Mathematical modelling of cell motility in a Rac/Rho/paxillin system with multiple timescales

Lucie Plazen, Department of Mathematics and Statistics

McGill University, Montreal

Supervisor: Anmar Khadra

November, 2022

A thesis submitted to McGill University in partial fulfillment of the requirements of the degree of

Master of Science

Table of Contents

Contents

Abstract

Mesenchymal cell motility is implicated in numerous physiological processes such as wound healing, embryonic development or cancer metastis. As such, understanding the molecular mechanisms underlying mesenchymal cell motility is crucial, but also challenging due to the high complexity of the network of over 200 proteins involved. Two key members of the Rho-family of GTPases, Rac1 and RhoA, along with the adaptor protein paxillin, are known to be particularly implicated. Together, they form a key signaling pathway that involves the mutual inhibition exerted by Rac1 and RhoA on each other and the promotion of Rac1 activation by phosphorylated paxillin at serine 273 (S273) residue. High concentration of active form of Rac1 (RhoA) can be found at the front (back) of migrating cells. This asymmetry is what defines cell polarization, generating persistent and directional migration. Yet, motility patterns appears to go beyond cellular polarization.

In the first part of this thesis, we simplify a pre-existing six-dimensional (6D) reaction-diffusion model describing the interactions of these three proteins (in their active/phosphorylated and inactive/unphosphorylated forms). This is done by first ignoring diffusion, thus turning the model into a system of ordinarily differential equations (ODEs), followed by reducing the dimensionality of the model using linear regression and quasi-steady state approximation (QSSA). The resulting one-dimensional (1D) ODE model describing Rac1 dynamics is then expanded phenomenologically, into an excitable 3D model that includes three timescales comprised of one fast variable: the scaled concentration of active Rac1, one slow variable: the maximum paxillin phosphorylation rate B (a parameter that is turned into a variable) and a very slow variable: the recovery rate of B to its resting state k_B (also a parameter that is turned into a variable). Using slow-fast analysis, we demonstrate how relaxation oscillations (ROs) and mixed-mode oscillations (MMOs) are produced by the model due to delayed Hopf bifurcation. Reintroducing diffusion in Rac1 dynamics, we show that new spatiotemporal patterns can be generated. This, as a result, motivated the questions of how such excitable dynamics may impact cell motility and how the spatiotemporal dynamics produced compare to migration patterns detected in Chinese Hamster Ovary (CHO-K1) cells.

In the second part of the thesis, we (i) utilize the Cellular Potts Model, a computational model that allows for the simulation of a virtually migrating cell in the form of a deformable object that can extend or retract, and move according to an energy-minimization technique; as well as (2) analyze imaging data of migrating CHO-K1 cells in 2D frames. We use a set of four metrics, instantaneous cell speed, exponent of mean square-displacement (called α-value), directionality ratio and membrane activity rate, to fully characterize and compare motility patterns in simulated CPM and CHO-K1 cells. In simulated cells, protrusions in cell membrane change localization, resulting in membrane oscillations and fast directionality variations similar to those seen in CHO-

K1 cells. This type of behaviour causes CPM and CHO-K1 cells to display exploratory and stationary motility phenotypes. When comparing the four different metrics between CPM and CHO-K1 cells, we find that they exhibit very similar outcomes, highlighting the importance of excitability in defining motility. Variations in migration patterns induced by mutating paxillin's S273 residue are also investigated using both the CPM model and machine learning. Our results reveal that this mutation alters the dynamics of the system through variation of paxillin phosphorylation sensitivity to the concentration of an active form of an adhesion protein called p21-Activated Kinase 1 (PAK). Taken together, our study suggests that MMOs and adhesion dynamics on multiple timescales are key ingredients underlying CHO-K1 cell motility.

Abrégé

La motilité des cellules mésenchymateuses est impliquée dans de nombreux processus physiologiques tels que la cicatrisation, le développement embryonnaire ou les métastases cancéreuses. Il est donc crucial de comprendre les mécanismes moléculaires qui sous-tendent la motilité des cellules mésenchymateuses, mais cela représente aussi un défi en raison de la grande complexité du réseau constitué de plus de 200 protéines. Deux membres clés de la famille des GTPases Rho, Rac1 et RhoA, ainsi que la protéine adaptatrice paxillin, sont connus pour être particulièrement impliqués. Ensemble, ils forment une voie de signalisation clé qui implique l'inhibition mutuelle exercée par Rac1 et RhoA l'un sur l'autre et la promotion de l'activation de Rac1 par la paxillin phosphorylée au résidu sérine 273 (S273). Une forte concentration de la forme active de Rac1 (RhoA) peut être trouvée à l'avant (arrière) des cellules en migration. Cette asymétrie est ce qui définit la polarisation cellulaire, générant une migration persistante et directionnelle. Cependant, la grande variété des modes de motilité semble aller au-delà de ce modèle de polarisation cellulaire.

Dans la première partie de ce mémoire, nous simplifions un modèle préexistant de réaction-diffusion à six dimensions (6D) décrivant les interactions de ces trois protéines (dans leurs formes actives/phosphorylées et inactives/non-phosphorylées). Pour ce faire, nous commençons par ignorer la diffusion, transformant ainsi le modèle en un système d'équations ordinairement différentielles (ODE), puis nous réduisons la dimensionnalité du modèle en utilisant la régression linéaire et l'approximation d'état quasi-stable (QSSA). Le model EDO unidimensionnel (1D) qui en résulte et qui décrit la dynamique de Rac1 est ensuite étendu de manière phénoménologique, sur la base d'hypothèses physiologiques raisonnables, en un modèle 3D excitable qui comprend trois échelles de temps et qui est constitué d'une variable rapide : la concentration de Rac1 actif normalisée, une variable lente : le taux maximal de phosphorylation de la paxillin B (un paramètre qui est transformé en variable) et une variable très lente : le taux de récupération de B à son état de repos k_B (également un paramètre qui est transformé en variable). En utilisant l'analyse lent-rapide, nous démontrons comment les oscillations de relaxation (ROs) et les oscillations de mode mixte (MMOs), qui combinent des oscillations lentes de grande amplitude avec des oscillations rapides de petite amplitude, sont produites par le modèle en raison d'une bifurcation de Hopf retardée. En réintroduisant la diffusion dans la dynamique de Rac1, nous montrons que de nouveaux motifs spatio-temporels, différents du wave-pinning, peuvent être générés. Nous nous sommes alors demandé comment une telle dynamique excitable pouvait avoir un impact sur la motilité des cellules et comment la dynamique spatio-temporelle produite se comparait aux schémas de migration détectés dans des cellules d'ovaire de hamster chinois (CHO-K1).

Dans la deuxième partie du mémoire, nous (i) utilisons le Cellular Potts Model (CPM), un modèle de calcul

qui permet de simuler une cellule virtuelle en migration sous la forme d'un objet déformable qui peut s'étendre ou se rétracter, et se déplacer selon une technique de minimisation de l'énergie ; ainsi que (2) analysons les données d'imagerie de cellules CHO-K1 en migration. Nous utilisons un ensemble de quatre mesures, la vitesse instantanée des cellules, l'exposant du déplacement quadratique moyen (appelé valeur α), le rapport de directionnalité et le taux d'activité membranaire, pour caractériser et comparer entièrement les modèles de motilité des cellules simulées CPM et CHO-K1. Dans les cellules simulées, les protrusions de la membrane cellulaire changent de localisation, ce qui entraîne des oscillations de la membrane et des variations rapides de la directionnalité similaires à celles observées dans les cellules CHO-K1. Ce type de comportement amène les cellules CPM et CHO-K1 à présenter des phénotypes de motilité exploratoire et stationnaire. En comparant les quatre métriques différentes entre les cellules CPM et CHO-K1, nous constatons qu'elles présentent des résultats très similaires, ce qui souligne l'importance de l'excitabilité dans la définition de la motilité. Les variations des modes de migration induites par la mutation du résidu S273 de la paxillin sont également étudiées à l'aide du modèle CPM et de l'apprentissage automatique. Nos résultats révèlent que cette mutation modifie la dynamique du système par une variation de la sensibilité de la phosphorylation de la paxillin à la concentration d'une forme active d'une protéine d'adhésion appelée p21-Activated Kinase 1 (PAK). Dans l'ensemble, notre étude suggère donc que les MMO et la dynamique d'adhésion à plusieurs échelles de temps sont des ingrédients clés qui sous-tendent la motilité des cellules CHO-K1.

Acknowledgements

I would like to thank first and foremost my supervisor Dr Anmar Khadra for his commitment to my education, his infinite patience and investment in my project and for passing on his passion of mathematical modelling and dynamical systems. Professor Khadra has provided me with help and precious advice at every stage of the project, which has been appreciated beyond words. Professor Khadra gives the best of himself for his students; for that I will always be grateful.

I also would like to thank our collaborators Dr Claire M. Brown and her PhD student Jalal Al Rahbani who patiently introduced me to the world of microscopy and experimental biology, and shared their feedback on my work all along my Master. They brought a new perspective on the project and deeply enriched my graduate experience.

I would like to express my gratitude to all members of the Khadra Lab for their precious support and suggestion, for their kindness, when sharing coffee and advice in the lab, and for the fruitful debates that were raised during lab meetings and beyond. I also thank Dr Laurent Mackay, a former member of the Khadra Lab, who welcomed me at McGill on my first days and introduced me to the topic of cell motility in general and to this project in particular.

Finally, my graduate experience would not have been the same without the continuous love and support of my friends and family who stood by me and always found the right words to remind me of my goals, to help me find balance and to give the best of myself.

Contributions of Authors

This thesis is comprised of three main chapters, Chapters 2 and 3 are based on an article that I co-authored. Chapters 2 and 3 have been submitted in peer reviewed journals: *Bulletin of Mathematical Biology* and *Scientific Reports* respectively. They are already available on bioRxiv: [1] and [2]. Chapter 1 is a literature review of the general mechanisms related to cell motility and of mathematical modelling in this field and as such does not contain significant contributions to original knowledge. Below I have briefly summarized my contributions to original work by chapter.

Chapter 2

- I simplified a pre-existing molecularly-explicit model for cell motility that describes the dynamics of active and inactive Rac, based on its interaction with other proteins including Rho and paxillin by applying a series of steps comprised of quasi-steady states approximations and linearization.
- I subsequently refined the model to include multiples timescales and to account for slow dynamics in adhesion and paxillin phosphorylation. I analytically solved its ODE version, demonstrating how it is capable of producing mixed-mode oscillations and relaxation oscillations, in addition to bistability seen in the original model.
- This analysis required the use of slow-fast analysis, and led me to consider the layer and the reduced problems in the 3D ODE model. Based on this analysis, I concluded that MMOs are due to both canard explosion and delayed Hopf bifurcation.

Chapter 3

- I implemented the refined model using the CPM to produce computer simulated migrating cells, and quantified their migratory patterns with a set of metrics which cover many aspects of cell motility, including speed, directionality, membrane activity and number of events detected in their migration tracks.
- I showed that the CPM cells exhibited three migratory patterns that were heavily influenced by not only the mutual inhibition of Rac and Rho, but also by the combination of slow large amplitude and fast small amplitude oscillations detected within MMOs. Our investigation revealed that the oscillatory and inactive modes of migration in CPM cells were consistent with the migratory patterns of active and inactive CHO-K1 cells.

- I quantified the effects of mutation of Serine-273 residue on paxillin on CHO-K1 cell migration patterns. The cells were imaged by our collaborators Jalal Al Rahbani and Dr Claire M. Brown, and also originated from work done in the Brown lab that had already been published. By altering the sensitivity of paxillin phosphorylation to active PAK concentration, I successfully reproduced the motility patterns of CHO-K1 cells expressing one of the two paxillin-mutants: S273A and S273D with the CPM cells.

My supervisor and I were responsible for writing the text in Chapters 2-3. Dr Claire Brown, and Jalal Al Rahbani edited the second manuscript (as co-authors). I was solely responsible for the development of the code in Chapters 2 and 3, for the formal analysis done in Chapter 2 and 3, and for the image and data analysis done in Chapter 3. I obtained significant feedback from my supervisor, Anmar Khadra.

List of Figures

List of Tables

1 Introduction and literature review

1.1 Cell motility

Cell motility refers to the spontaneous movement of a cell by energy consumption. The migration of neutrophils from the bone marrow to sites of infections during the process of wound healing [3], cell rearrangement in the early stages of embryonic development [4], creation of new blood vessel in the context of angiogenesis [5] or axonal growth during development [6] are a few example of key physiological processes where cell migration is involved. Although it is very critical for ensuring communication between the many tissues and organs regulating essential physiological processes, cell motility is also implicated in diseases such as cancer metastasis [3, 7] and thrombosis [8].

The wide variety of processes through which a cell can initiate and maintain a motion have for long been studied, and can be divided into two broad categories: amoeboid and mesenchymal motility. Amoeboid migration is a mode of rapid motility that is driven by actin-rich pseudopods (extention of the cell membrane) and a highly-contractile uropod (hind part of polarized cells), and is characterized by weak or absent adhesion to the substratum or extracellular matrix (ECM) [9,10]. In this mode, cells are highly deformable and exert very low traction force on the environment. Mesenchymal cell migration, on the other hand, is a mode of motility characterized by cell polarization to form a leading edge that extends actin-rich protrusions (such as lamellipodia), leading to adhesive interactions with the substratum and proteolytic extracellular matrix remodelling, followed by retraction of the contractile cell rear to achieve cellular movement [11].

In both of these modes of motility, there is a clear cell phenotype associated with them, namely, the formation of polarized cells with two distinct regions of activity: a front where the membrane is pushed outward by the growth of the actin cytoskeleton, and a back whose retraction is dynamically driven by the myosin molecular motor. In other words, the actin cytoskeleton is a key modulator of cell polarity and cell motility [12].

Single-cell migration enables cells to move towards and between tissue compartments [13], but cells may also form cohesive ensemble and mobilize as a collective [14]. Collective cell migration is defined as the coordinated movement of multiple cells that retain cell–cell contacts while coordinating their actin dynamics and intracellular signalling [15]. It implies, in addition to integrin-based adhesion dynamics (explained in detail in the next section), the formation of cadherin adhesion structures. Cadherin are cell–cell adhesion molecules expressed in many different cell types that are required for proper cellular function and maintenance of tissue architecture [16]. It is important for the formation of junctions that allow cells to adhere to each other.

The purpose of this thesis is to focus mainly on single-cell mesenchymal migration, by studying one particular

cell type: Chinese Hamster Ovarian cells (also referred to as CHO-K1 cells). We will therefore restrict ourselves now to the molecular mechanisms involved in single-cell mesenchymal migration.

1.1.1 Rac and Rho

The two members of the Rho family of GTPases, RhoA and Rac1 (referred to as Rac and Rho for the remainder of this study), along with their interactions with a third signal transduction protein named paxillin, are known to be key modulators of cell motility [17, 18]. They have been identified in the 1990's as key players responsible for generating cellular polarity and cell migration [19–22]. Rac and Rho transition from being inactive (guanosine diphosphate (GDP)-bound) to active (guanosine triphosphate (GTP)-bound) forms, via Guanine nucleotide Exchange Factors (GEFs), and vice versa, via GTPase-Activating Proteins (GAPs) [20]. Their activation is also inhibited by the active form of the other protein, generating a cross-talk between the two proteins (i.e., they mutually inhibit each other). Together these two processes of activation and deactivation form the key signaling pathways for producing cellular polarization [20]. Active Rac is responsible for actin polymerization, causing membrane protrusion [21–24] and formation of lamellipodia (cytoskeletal projection of the membrane at the leading edge of the cell). Rho, on the other hand, is known to induce the formation of actin stress fibers and large stable focal adhesions [17, 20, 25], and is responsible for the actomyosin-driven contractions at the rear of a cell required for membrane retraction towards the nucleus [26]. This thesis mainly focuses on the study of the two members of the Rho family of GTPases Rac and Rho and on the molecular processes involving paxillin, that control the activation of these proteins. Regulation of cell migration involves changes in protein activities through complex signalling cascades that imply various signal-transduction proteins. The total number of effectors of the Rho family of GTPases is not yet known, but it is sufficiently high that accounting for all the signalling pathways is not a reasonable approach to study the system. Instead, in this thesis, we focus on one particular pathway: the GIT-PIX-PAK signalling cascade (described in details in the next section) which causes the elevation in active Rac concentration through the binding of this molecular complex to paxillin subsequent to its phosphorylation [27, 28].

In the early stages of cell motility research, the Cdc42 protein, a third small GTPase of the Rho family, was also shown to be implicated in the reorganization and regulation of cell adhesion, migration, and invasion [29]. The many signalling pathways involved in defining cell motility are nevertheless known for their redundancy, intricacy and multiple feedback loops. This makes the task of identifying the key regulatory mechanism underlying cell motility even more challenging, and motivate the effort of pursuing other approaches (e.g., computational modelling) to understand cellular motility. Because of the redundancy of the chain of actions with Rac, Cdc42 has been typically ignored and the main focus has shifted towards Rac and Rho only [30].

1.1.2 Adhesion and paxillin

Cell adhesion molecules (CAMs) are a subset of cell surface protein complexes that allow the binding of cells with other cells or with the extracellular matrix (ECM) [31]. They are typically divided into four families: the immunoglobulin superfamily cell adhesion molecules, the cadherins, the integrins and the Superfamily of C-type of lectin-like domains proteins (CTLDs) [32]. Integrins are transmembrane adhesion molecules that are involved in both cell-cell adhesion and cell adhesion to the ECM. They play an important role in modulating cell signaling pathways of transmembrane protein kinases which can subsequently mediate cell adhesion dynamics (including assembly and disassembly), cell spreading and migration; mesenchymal cell motility primarily relies on integrin-based adhesions.

Integrin-based adhesions are protein complexes that provide a mechanical link between the extracellular environment and the actin cytoskeleton; they create a bio-mechanically regulated force transmission point between a cell's actin-cytoskeleton and its environment [33]. Therefore, the properties of these dynamic structures can heavily influence the nature of cell migration.

Adhesion sites are known to be composed of more than 900 proteins, whose spatiotemporal arrangement is of high complexity and dependent both on external and internal cues [34]. The adhesion lifecycle is typically initiated in protrusive regions of the cell, which are in the context of cell motility, found at the leading edge of the cell. Small clusters of integrin, called nascent adhesions (NAs) initially form [35, 36]. Although the majority of these NAs quickly disassemble - they are characterized by a turnover rate of less than one minute - a small fraction do not and are instead stabilized through increased association with actin filaments and become enlarged [37,38]. These adhesions are termed focal complexes (FCs). The transition from a NA to a FC requires both Rac-dependent increases in traction force and proper organization of the actin network adjacent to the aforementioned depolymerization zone [39]. Focal complexes have a turnover rate on the order of one minute, and can eventually mature into relatively large, stable focal adhesions as the junction between adhesions and the ECM tightens and more molecular components are recruited. Focal adhesions typically have a life span of a few minutes to an hour. [38]. Spatial organization of adhesion sites in a migrating cell is summarized in Fig. 1.

The adhesion plaque is the multi-molecular dynamic scaffold that links integrins to the actin cytoskeleton; its formation involves the recruitment of adhesion proteins including talin, focal adhesion kinase (FAK), vinculin, and paxillin [40]. Paxillin is a 68-kDa adaptor protein found in the adhesion plaque. Through the interactions of its multiple protein-binding modules, many of which are regulated by phosphorylation, paxillin serves as a platform for the recruitment of numerous regulatory and structural proteins that together control the dynamic changes in cell adhesion [41,42]. Paxillin is also involved in control of cytoskeletal reorganization and gene expression that are necessary for cell migration and survival [43]. In particular, paxillin plays a central role in coordinating the spatial

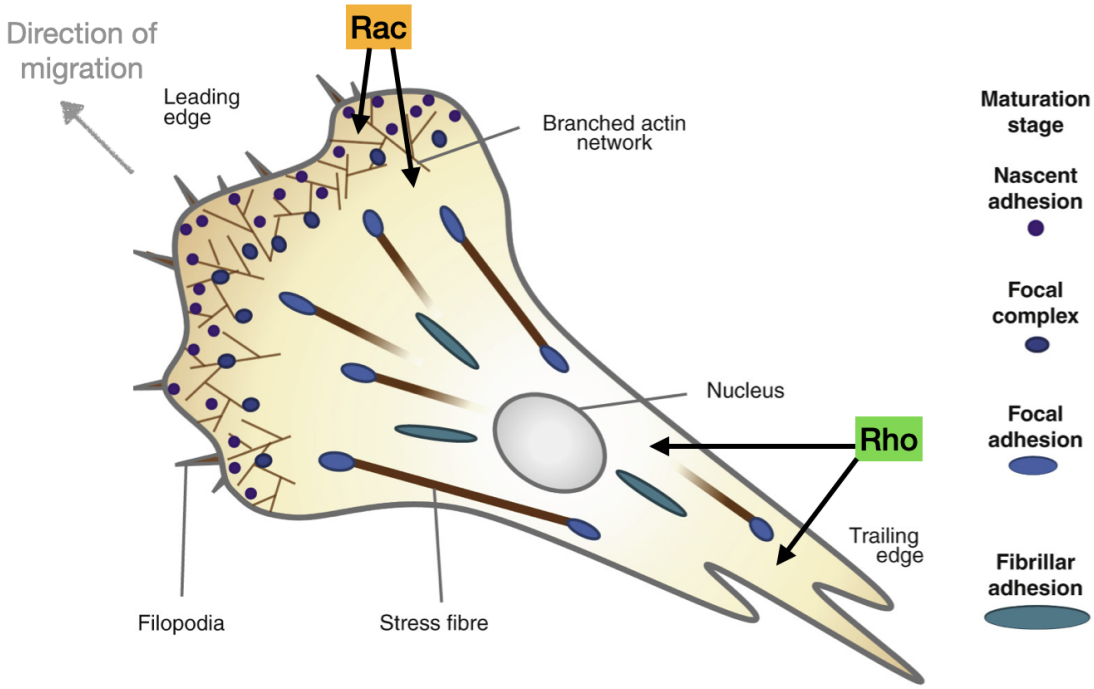

Figure 1: The components of a migrating cell. The polarized cell has a front (top-left) and a back (bottom-right), display various adhesions sites (nascent, focal complexes, focal adhesions), that are used to anchor to the extra-cellular matrix and allow the cell to apply forces resulting in its motion. Adapted from [38]

and temporal action of the Rho family of small GTPases, which regulate the actin cytoskeleton [42]. Paxillin can get phosphorylated at its serine 273 (S273) residue by the active form of the protein p21-Activated Kinase 1 (PAK) when bound to RacGTP (PAK-RacGTP), and subsequently promote Rac activation as a GEF [41, 44]. The binding of the protein complex (GIT-PIX-PAK), formed by the G protein-coupled receptor kinase InteracTor 1 (GIT), beta-PAK-Interacting eXchange factor (PIX), and PAK, to phosphorylated paxillin allows this entire complex to act as a GEF [41].

1.1.3 Cell Polarity

A hallmark of cell motility is cell polarity: the presence of a stable front and back whose internal architectures in term of actin cytoskeleton are deeply different, but that also show differences in the type of proteins found, their binding to the membrane and their activity/phosphorylation status [17]. It has been shown that Rac activity is mainly restricted to the leading edge of the cell [21], whereas Rho activity happens at the back [18, 45]. Suche spatial localization is consistent with their antagonistic role (Rac promoting actin polymerization, Rho promoting membrane retraction) and their mutual inhibition of each other [20]. This provides an other way to characterize cell motility, by the presence of this cell-wide gradient in concentrations of Rac (highly active at the front) and

Rho (highly active at the back).

1.2 Mathematical modelling of cell motility

Understanding the underlying molecular mechanisms that lead to cell migration is a challenging task due to the number of different proteins involved (over two hundred), and the complexity of the biological signalling pathways. They involve multiple non-linearities, complex feedback interactions and stochastic processes that lead to heterogeneous migratory phenotypes. This explains the very widespread use and popularity of mathematical models to understand the mechanisms regulating cell migration [46]. This approach allows, by building simplified models, to isolate, reduce and fully characterize the roles of key proteins, such as Rac and Rho, and to understand the implications of the various parameters in different conditions.

Several types of mathematical models dealing with cell motility have been previously developed. Each one of these models decipher the dynamics of a given phenomenon such as the physical process involved in the protrusion of a filopodia [47], the importance of membrane flexibility [48] or the F/G-actin branched network [49]. Some of these models follow a more holistic view of cell movement, and discuss the degree of adhesion strength and the mechanical properties of the cell itself can have on general cell migration [50, 51]. This second approach is the one that will be adopted in this thesis.

1.2.1 Schematic of cell motility

The general framework to tackle cell motility was first given by Abercrombie in his Croonian lecture [52] in 1980 where he presented the knowledge of the machinery of cell movement at that time, and gave a schematic model of cell movement. Although the model was not mathematical, it suggested the various functions the cell performs. This general approach has since been the most exclusively used when analyzing cell motility. The model summarizes motility pattern and steps that govern mesenchymal migration as follows. First, the cell membrane at the front, i.e., the lamellipod, stretches and is pushed outward by the action of the cytoskeleton. Then, it attaches to the extracellular matrix through maturing focal adhesions. Third, the adhesion sites at the extreme back of the cell detaches, loosening the back membrane. Finally, this membrane is pulled by the myosin molecular motor acting over the filaments that connect the back to the nucleus, causing the retraction of the trailing edge of the cell.

1.2.2 Reaction-diffusion models

Rac and Rho are diffusive proteins that can be found throughout the cytoplasm; in their active forms, however, these proteins are bound to the membrane, and as a result, their diffusion is reduced compared to their inactive

cytosolic forms [53]. Paxillin, on the other hand, doesn't show significant differences in its diffusion in its phosphorylated and unphosphorylated forms [54].

This explains the use of partial differential equation models in cell motility. Such models have to account for the spatial variability that should result from the diffusion of the G-proteins and the various mechanisms involved in their activation.

In the work of Marée *et al* (2006) [55], the three GTPases Rac, Rho and Cdc42 were considered; their activations and mutual interactions of each other were studied in a PDE reaction-diffusion model. The molecular crosstalks captured here are the Cdc42-mediated activation of Rac, which then triggers the activation of Rho. In addition, Rho and Cdc42 feedback onto each other through a mutual inhibition that does not involve Rac. The active form G of each protein's dynamic is dictated by the following equation

$$\frac{\partial G}{\partial t} = I_G(G', G'')\frac{G_i}{G_{tot}} - d_G G + D_G \Delta G \tag{1}$$

Here $G = C, R$ or ρ representing Cdc42, Rac and Rho respectively. I_G is the activation rate that depends on the active forms of two other proteins denoted by G' and G''. The inactive form of G is denoted by G_i. This dependence can be expressed linearly ($I_R(C) = (I_R + \alpha_C C)$), as a Hill function ($I_C(\rho) = (\frac{I_C}{1+(\frac{\rho}{\beta_\rho})^n})$, $I_\rho(R, C) = \frac{(I_\rho + \alpha_R R)}{1+(\frac{C}{\beta_C})^n}$) to indicate cooperativity, or as a simple Michaelis-Menten kinetic (which corresponds to a Hill function modelling with a Hill coefficient of $n = 1$). Note here that Cdc42 and Rho are mutually inhibiting each other whereas Rac activation is promoted by Cdc42.

Assuming conservation of matter, the inactive form's equation can be deduced

$$\frac{\partial G_i}{\partial t} = -I_G(G', G'')\frac{G_i}{G_{tot}} + d_G G + D_{G_i} \Delta G_i \tag{2}$$

Marée *et al* incorporated the system in a model of the cell which specified a Rho-dependent contraction force and the branching of the actin network at the edge of the cell. This framework was used to eventually draw conclusion on the ability of fish keratocytes to polarize, in response to a stimulus, and on the various shapes they can maintain throughout the migration process. They showed that polarity is triggered by interactions of Cdc42, Rac and Rho, while maintenance and robustness of polarity is due to the rapid cytosolic diffusion of the inactive forms of the small GTPases.

Such general framework was used in many motility studies, yet variations around the expression of the activation rate functions were proposed. In Jilkine *et al* (2007) [25], each of the three possible forms was considered for each GTPase, and they showed that linear terms result in monostability for Rac and Cdc42, inconsistent with cell polarization. They showed in addition, that assuming Michaelian terms for inhibition and

linear terms for activation do not allow for bistability. This supports the idea that cooperation and inhibition in protein activation are necessary for cell polarity. Important to note here that, the authors of this study assumed constant concentration in the inactive forms.

In Holmes *et al* (2017) [56], the formulation and strength or level of cooperativity of the multiple feedbacks loops were also analyzed, along with their implication on motility. They eventually showed that Hill functions are the kinetics terms that best capture cell motility with their modelling assumption. In addition, they showed that conservation of matter allows for complex oscillatory dynamics in the proteins concentration to arise and play an important role in the competition between lamellipods, a behavior which is not reproductible when mass concervation is not enforced.

In Marée *et al* (2012) [57], the work of Marée *et al* (2006) was extended by including the effects of the feedback between small signalling molecules, namely, the phosphoinositides (PIs), and Rho family GTPases. This was done by modulating the activation rates of the GTPases with the concentration of the PIP_3, and used to demonstrate how Cdc42 activity zones can benefit from the PIs feedback. They showed an increase in amplitude and extension of zones of Cdc42 activity in the cytoplasm, which they suggested it facilitated global communication between competing cell "fronts". This showcases how the comprehension of general GTPases temporal dynamic can be refined by accounting for additional signalling molecules.

In more recent studies [58–60], the Cdc42 GTPase was ignored and Rac was taken to be the sole inhibitor of Rho. This mutual inhibition pathway is known to be the necessary ingredient of cell motility and cellular polarization as far as the Rac/Rho subsystem is concerned. The models are all shown in these studies to produce bistability and to allow for a cell-wide gradient with inverse orientation between Rac and Rho to stabilize.

Still, these studies only modelled the cell signalling pathways and how internal dynamics can control cell motility and/or generate cell polarity. Recently, Rens *et al* (2021) [58] studied how cell deformation and adhesions can feedback onto the extracellular matrix (ECM) and how motility patterns (that they classified into three categories: oscillatory, persistent and random) may vary based on the type of forces applied to the ECM through adhesion sites. They considered the coupling between external and internal cues, by keeping the model simple, with few variables (Rac, Rho in active and inactive forms, and the ECM). They simulated cells using a Cellular Potts Model (CPM) numerically. This allowed them to observe a variety of patterns and cell behaviours, including persistent polarity, flipped front-back cell polarity oscillations, spiral waves, and random protrusion-retraction. With their CPM simulations, they also showed that the observed spatial patterns depend on the cell shape, and vice versa.

As such, cell motility has been extensively studied in the past twenty years. Yet, there is no denying that the majority of signalling pathways and motile behaviours remain to be explained.

1.2.3 Wave-pinning

In a one-dimensional or two-dimensional spatial domain, the wave-pinning phenomenon describes a travelling wave in chemical concentration that is pinned in space, generating a concentration gradient that remains stable at steady state, preventing homogenization of the spatial domain. It was shown that a simple two-dimensional reaction-diffusion model of two mutually-inhibiting and conserved molecules can produce this phenomenon of wave-pinning [61]. A hallmark of cell motility is cell polarity: the presence of a stable front and back. Active Rac is highly localized at the leading edge and active Rho is highly localized at the back of the cell. The wave-pinning pattern is believed to be responsible for generating cell polarity, and spatially localizing Rac and Rho to the front and back, respectively. This pattern was generated in several Rac/Rho models [56, 58, 62].

1.3 Study objectives

Adhesion and protrusion are the two main processes involved in cell motility. They need to coordinate and exchange signals in order to initiate and maintain migration. In this thesis, we will study the interactions between, the Rac/Rho subsystem, responsible for the formation of lamellipodium, for membrane protrusion, retraction, and for actin polymerization, as well as paxillin, known to be a key player in the formation and growth of adhesion sites. This study aims at providing insights on the consequences of this dialogue on cell motility.

Also, while CHO-K1 cell movement occurs on a timescale of hours, formation of protrusion and assembly of adhesion sites only take minutes, and activation and/or phosphorylation of proteins occur in seconds. In other words, cell migration can be studied on multiple timescales. In this thesis, we want to emphasize the importance of this time-scale separation in guiding the dynamics of cells, and to decipher the mechanisms that can allow processes acting on different timescales to get organized as a whole. Despite their lack of significant polarity, CHO-K1 can dynamically protrude, retract, and explore their surrounding environment when they are placed on glass coverslips coated with extracellular matrix (ECM) proteins [63]. They display complex migratory patterns that go beyond the simple unidirectional motility that result from wave-pinning. In these patterns, protrusion dynamically change localization, allowing for wavy movement of the membrane to form and frequent changes of direction to occur thoughout the trajectory of the cells.

This study aims to shed new light onto the dynamic interactions between Rac and paxillin in an integrative manner that includes mathematical modelling, computer simulations and finally the use of experimental data to further validate model predictions. By leveraging our understanding of the temporal evolution of protein activity, we aim to provide a simple way to address the question of cell motility that may yet provide an explanation for

the complex patterns observed in CHO-K1 cell migration.

In this thesis, we adapt a previously developed Rac, Rho, and paxillin reaction-diffusion model to pursue the objectives of this study. The added value of our models will be to take into account the dynamics of these proteins in different timescales and parameter regime. The goal is to provide information about how cell motility manifest itself in new parameter regimes not related to wave-pinning. Finally, modelling efforts should aim to reproduce classical features of cell motility (such as the wave-pinning phenomenon) but also to provide a new perspective on motility, by illustrating how slow dynamics can impact motility. By employing the same approach that in [25], we will first analyzed an ODE version of our models. The experimentally-observed spatial segregation of active Rac and Rho in polarized cells indicates that the cell can be thought as a multi-compartment entity where the proteins concentration are locally homogeneous but can globally differ between localizations. The separation between these various zones are actually fronts that are pinned in space (due to wave-pinning); they can be neglected when studying the dynamics of the proteins in each zone because they are very narrow. To ensure distinct values at (potentially multiple) front versus back, this system of ODEs should have multiple steady states, i.e., it should exhibit bistability once appropriate cross-talk terms are included in the model.

2 Excitable dynamics in a molecularly-explicit model of cell motility: Mixed-mode oscillations and beyond

MANUSCRIPT

Lucie Plazen[1], Anmar Khadra[2,*]

[1]Department of Mathematics and Statistics, McGill University, Montreal, Canada

[2]Department of Physiology, McGill University, Montreal, Canada

[*]**Corresponding author:** Anmar Khadra

McIntyre Medical Building (room 1120)

3655 Prom. Sir William Osler

Montreal, Quebec, Canada H3G 1Y6

Email: anmar.khadra@mcgill.ca

Telephone: (514) 398-1743

Abbreviated title: Mixed-mode oscillations in cell motility

Keywords: Rho family of GTPases, cellular polarity, mathematical model, hysteresis and bistability, wave-pinning, mixed-mode oscillations, relaxation oscillations, slow-fast analysis, cellular potts model, migration patterns.

Data availability: The datasets generated during and/or analysed during the current study are available in the Anmar Khadra repository, `http://www.medicine.mcgill.ca/physio/khadralab/Codes/code_plazen_excitability.html`.

Funding: This work was supported by the Natural Sciences and Engineering Research Council of Canada discovery grant to AK, and the Fonds Nature et technologies team grant to AK. The funders had no role in study design, data collection or analysis, decision to publish or preparation of the manuscript.

Conflict of Interest: No conflict of interest.

Abstract

Mesenchymal cell motility is mainly regulated by two members of the Rho-family of GTPases, called Rac and Rho. The mutual inhibition exerted by these two proteins on each other's activation and the promotion of Rac activation by an adaptor protein called paxillin have been implicated in driving cellular polarization comprised of front (high active Rac) and back (high active Rho) during cell migration. Mathematical modeling of this regulatory network has previously shown that bistability is responsible for generating a spatiotemporal pattern underscoring cellular polarity called wave-pinning when diffusion is included. We previously developed a 6D reaction-diffusion model of this network to decipher the role of Rac, Rho and paxillin (along with other auxiliary proteins) in generating wave-pinning. In this study, we simplify this model through a series of steps into an excitable 3D ODE model comprised of one fast variable (the scaled concentration of active Rac), one slow variable (the maximum paxillin phosphorylation rate - turned into a variable) and a very slow variable (a recovery rate - also turned into a variable). We then explore, through slow-fast analysis, how excitability is manifested by showing that the model can exhibit relaxation oscillations (ROs) as well as mixed-mode oscillations (MMOs) whose underlying dynamics are consistent with a delayed Hopf bifurcation. By reintroducing diffusion and the scaled concentration of inactive Rac into the model, we obtain a 4D PDE model that generates several unique spatiotemporal patterns that are relevant to cell motility. These patterns are then characterized and their impact on cell motility are explored by employing the cellular potts model (CPM). Our results reveal that wave pinning produces purely very directed motion in CPM, while MMOs allow for meandering and non-motile behaviours to occur. This highlights the role of MMOs as a potential mechanism for mesenchymal cell motility.

2.1 Introduction

Excitability is a very frequently observed phenomenon in many physiological systems including, but not limited to, cellular and molecular biology, neurophysiology [A1, A2] and immunology [A3]. It typically refers to the ability of a system to exhibit large excursions in their main variables when a small stimulus is applied. Such large excursions could occur singularly, or could occur periodically in a cyclic fashion [A2]. It is usually manifested in four different ways, referred to in the literature as type I, II, III and IV excitability [A4]. Type I and II are periodic in nature and are generated by homoclinic and Hopf bifurcations, while type III and IV are singular generated by perturbations away from a stable steady state with the former (the latter) depending on differences in time scales (on crossing the stable manifold of a saddle fixed point) to generate the excursion [A5–A7]. These basic dynamics become significantly more complex when multiple time scaled are involved.

Cell motility, the spontaneous movement of a cell by energy consumption, is an essential process by which many physiological (e.g., embryonic development, wound healing, inflammation) [A8, A9] and pathophysiological (e.g., cancer metastasis) [A10, A11] systems depend on. It is generated by the asymmetric polarization of migrating cells with a front (or the leading edge) and a back (or the rear edge) along an axis roughly parallel to the path of migration [A12]. The molecular networks regulating cell motility are very prominent examples of systems that exhibit diverse types of excitability properties that can range in complexity and impact. Indeed, some of these molecular networks may be able to exhibit multitude of these excitability properties simultaneously when perturbing one parameter [A13]. One example of such behaviour was seen in a molecularly-explicit model describing the dynamics of lamellipodium in fish keratocytes [A14]. In this latter system, several migration patterns, including waving, traveling wave pulse and smooth motility, were observed [A14] and three types of excitabilities were detected in parameter space: type I, III and IV [A14, A15].

Mesenchymal cell motility, similar to that seen in Chinese hamster ovary (CHO-K1) cells, is regulated by a network of over 200 proteins (also called adhosome). It is characterized by the formation of protein complexes, called adhesions [A16–A18], that allow motile cells to anchor on a substrate and to link the extracellular matrix (ECM) to the actin-cytoskeleton network. Although the molecular network governing adhesion dynamics and motility is very complex in these cells, three key proteins have been implicated in regulating both of them. This includes two members of the Rho family of GTPases, namely, Rac1 and RhoA (referred to as Rac and Rho for the remainder of this study) [A19–A22], as well as an adhesion and adaptor protein called paxillin [A23]. This trimolecular regulatory network involves Rac and Rho cycling between their inactive (GDP-bound) to active (GTP-bound) forms, via Guanine nucleotide Exchange Factors (GEFs), and vice versa, via GTPase-Activating Proteins (GAPs) [A24], as well as the mutual inhibition that the active forms of these two proteins exert on each other [A24]. Active Rac and Rho are membrane bound, making their diffusion coefficients significantly

lower than those associated with their inactive forms which happen to be cytosolic. The adhesion protein paxillin, on the other hand, can get phosphorylated at its serine 273 (S273) residue by the active form of the protein p21-Activated Kinase 1 (PAK) when bound to RacGTP (PAK-RacGTP), and subsequently promote Rac activation as a GEF [A23, A25]. The binding of the protein complex (GIT-PIX-PAK), formed by the G protein-coupled receptor kinase InteracTor 1 (GIT), beta-PAK-Interacting eXchange factor (PIX), and PAK, to phosphorylated paxillin allows this entire complex to act as a GEF [A23]. A molecularly explicit reaction-diffusion model of this protein regulatory network was developed in the form of a six-dimensional (6D) partial differential equation (PDE) model [A26]. The model described the spatiotemporal dynamics of the scaled concentrations of active/phosphorylated and inactive/unphosphorylated forms of the proteins involved, as well as those auxiliary ones (i.e., GIT, PIX and PAK) that were set to steady states. The model was nondimensionalized, to reduce the number of parameters, and its steady state dynamics were analyzed in the absence of diffusion, demonstrating that it possessed two different time scales. In the presence of diffusion, the model was shown to exhibit wave pinning, a phenomenon in which a travelling wave is pinned in space, generating a concentration gradient in Rac and Rho responsible for forming cellular polarization.

In the absence of diffusion and by taking into account conservation of matter, the model was turned into a 3D ODE model (referred to hereafter as the original ODE model). This original ODE model was shown to possess two timescales and to exhibit a bistable switch. Bistability was defined by the coexistence of two steady states, one corresponding to elevated scaled concentration of active Rac (or low scaled concentration of active Rho) and another corresponding to the low scaled concentration of active Rac (or elevated scaled concentration of active Rho), and was delimited by saddle-node bifurcations. Beyond the saddle-node bifurcations, the model was monostable. The effects of bistability on the dynamics of the 6D PDE was then explored to show that it was responsible for generating wave-pinning with active Rac accumulating in the "front" of the one-dimensional spatial domain, and active Rho accumulating in the back. This phenomenon of wave-pinning produced by the Rac-Rho system was heavily investigated dynamically using a method called local perturbation analysis [A27], in which the large difference in diffusion coefficients between the active and inactive forms of Rac and Rho [A28] allowed the PDE model to be simplified into an ODE model that can provide insights into how the spatial patterns exhibited by the PDE model after a perturbation is formed. These analyses were helpful in determining the effects of different parameter regimes in defining dynamics.

It is important to point out that other complex models of the Rac-Rho system were also developed by coupling them to the ECM to generate oscillatory dynamics in the absence of diffusion [A29]. The amplitude of the oscillations in such models were typically uniform or changed minimally, allowing the PDE models to produce interesting spatiotemporal patterns. Implementing these models using the cellular potts model (CPM),

a computer-based discrete grid-based simulation technique that involves the modelling of the ECM as a mesh upon which simulated cells are superimposed [A30], typically produced migrating cells that were either purely directional or do not migrate significantly (depending on the amplitude of the oscillations), but not both. These oscillations were consistent with type II excitability through a Hopf bifurcation. In the presence of two competitive ECMs, the oscillations became more "random" (due to the presence of a period doubling bifurcation), but the amplitude of such oscillations did not change significantly change. As a result, the migration patterns produced by this model typically did not succeed in combining both exploratory and stationary behaviours in one simulation typically seen in mesenchymal cell motility [A31].

Here, we will expand on these studies by considering series of simplified models of the Rac-Rho-paxillin system capable of producing oscillatory dynamics with nonuniform amplitudes. The models will possess at least two timescales and are excitable in nature, allowing them to exhibit what is known as mixed-mode oscillations (MMOs) [A32–A34] that combine fast small amplitude oscillations with slow large amplitude oscillations. Because MMOs are more complex dynamically than relaxation oscillations (ROs) and because they are quite frequently observed in models of many physiological systems [A32, A35], we will investigate in this study how MMOs impact the spatiotemporal dynamics of the models considered here, especially in comparison to ROs. This will be done numerically by simulating the PDE models whose dynamics are regulated by MMOs and ROs, as well as by employing the CPM to simulate migrating cells.

2.2 The original spatiotemporal 6D PDE model

To understand quantitatively the behaviour of the regulatory network involving Rac, Rho and paxillin, a 6D reaction-diffusion mathematical model describing the dynamics of inactive (GDP bound) and active (GTP bound) forms of Rac and Rho as determined by paxillin S273 phosphorylation was developed [A26]. The model consisted of two main modules: the mutual inhibition exerted by Rac and Rho on each other, as well as the indirect positive feedback loop exerted by active Rac on itself through paxillin phosphorylation at S273 (Fig. 2A). The resulting spatiotemporal model over one spatial domain was comprised of 6 PDEs characterizing the interactions of the active and inactive forms of the two proteins Rac (R, R_i) and Rho (ρ, ρ_i) along with the phosphorylated and unphosphorylated forms of paxillin (P, P_i) at S273 residue. Rescaling the model into its nondimensionalized form

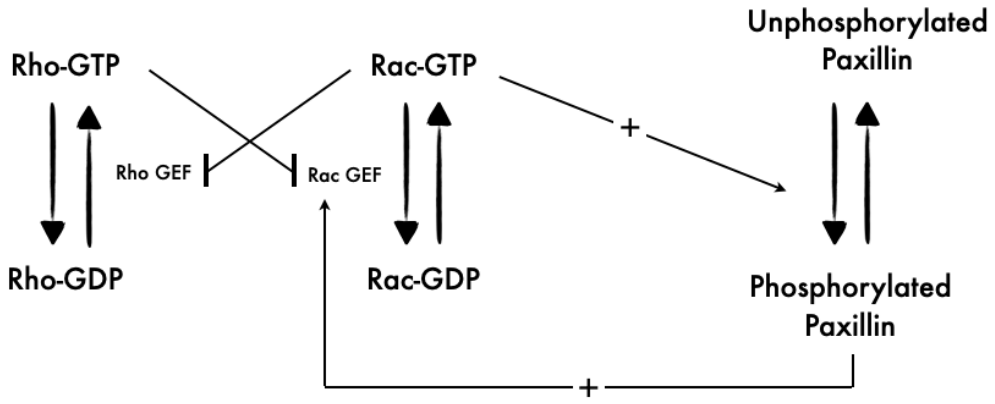

Figure 2: Schematic of the 6D model involving the Rac, Rho and paxillin regulatory network. Diagram of the signalling pathways of the 6D model showing the two proteins Rac and Rho cycling between inactive (GDP bound) and active (GTP bound) forms, and the active form of each protein inhibiting the activation of the other through GTPase-specific GEFs inactivation. It also shows how active Rac participates in paxillin phosphorylation at serine 273 (S273) residue which in turn promotes Rac activation in a positive feedback loop.

gave

$$\frac{\partial R}{\partial t} = (I_R + I_K^*)\left(\frac{L_\rho^n}{L_\rho^n + \rho^n}\right) R_i - \delta_R R + D_R \frac{\partial^2 R}{\partial x^2} \tag{3a}$$

$$\frac{\partial R_i}{\partial t} = -(I_R + I_K^*)\left(\frac{L_\rho^n}{L_\rho^n + \rho^n}\right) R_i + \delta_R R + D_{R_i} \frac{\partial^2 R_i}{\partial x^2} \tag{3b}$$

$$\frac{\partial \rho}{\partial t} = I_\rho \left(\frac{L_R^n}{L_R^n + (R + \gamma K)^n}\right) \rho_i - \delta_\rho \rho + D_\rho \frac{\partial^2 \rho}{\partial x^2} \tag{3c}$$

$$\frac{\partial \rho_i}{\partial t} = -I_\rho \left(\frac{L_R^n}{L_R^n + (R + \gamma K)^n}\right) \rho_i + \delta_\rho \rho + D_{\rho_i} \frac{\partial^2 \rho_i}{\partial x^2} \tag{3d}$$

$$\frac{\partial P}{\partial t} = B\left(\frac{K^n}{L_K^n + K^n}\right) P_i - \delta_P P + D_P \frac{\partial^2 P}{\partial x^2} \tag{3e}$$

$$\frac{\partial P_i}{\partial t} = -B\left(\frac{K^n}{L_K^n + K^n}\right) P_i + \delta_P P + D_{P_i} \frac{\partial^2 P_i}{\partial x^2}, \tag{3f}$$

where n is the Hill coefficient, L_ρ (L_R) is the Rho-dependent (Rac-dependent) half maximum inhibition of Rac (Rho), L_K represents the half-maximum phosphorylation of paxillin, I_R is the basal Rac activation rate, I_ρ is the Rho activation rate, B is the maximum paxillin phosphorylation rate, δ_ρ (δ_R) is the GAP-dependent Rho (Rac) inactivation rate, δ_P is the paxillin dephosphorylation rate, γ is the ratio of total PAK to total Rac, D_x ($x = R, R_i, \rho, \rho_i, P, P_i$) is the diffusion coefficient of each molecular species, K is the scaled concentration of active

PAK ($[PAK^*]$), given by

$$K = \frac{[PAK^*]}{[PAK]_{tot}} = \alpha_R R\left(1 + k_x[PIX] + k_G k_X k_C[GIT][PIX][Pax_{tot}]P)\right) K_i^* \tag{4}$$

and I_K^* is the $GIT - PIX - PAK$ complex-dependent Rac activation rate, given by

$$I_K^* = I_K\left(1 - K_i^*\left(1 + \alpha_r R\right)\right), \tag{5}$$

with

$$K_i^* = \{(1 + k_X[PIX] + k_G k_X k_C[GIT][PIX][Pax_{tot}])\left(1 + \alpha_R R\right) + k_G k_X[GIT][PIX]\}^{-1}. \tag{6}$$

The parameters in Eqs. (4) and (5) represent the association constant for $PIX - PAK$ binding (k_X), the association constant for $GIT - PIX$ binding (k_G), the association constant for $Pax_p - GIT$ binding (k_C), the concentration of GIT and PIX ($[GIT]$ and $[PIX]$) and the affinity constant for $PAK - RacGTP$ binding (α_R).

The first (second) terms in Eqs. (3a), (3c) and (3e) represent Rac, Rho activation (inactivation) and paxillin phosphorylation (unphosphorylation), respectively, whereas the third term represents the diffusion of these proteins. The terms in Eqs. (3b), (3d) and (3f) are defined similarly for the inactive/unphosphorylated form of these three proteins. Notice how the activation term of Rac (Rho) is a decreasing Hill function of Rho (Rac) to reflect the mutual inhibition exerted by the two proteins on each other, whereas the phosphorylation term of paxillin is an increasing function of Rac through K. The derivations of this highly nonlinear model are detailed in [A26, A36]. For the complete list of parameter definitions and values, see Table 1.

2.3 Model reduction and simplification into 1D ODE model

Due to the high dimensionality of the original 6D spatiotemporal PDE model (3) and the difficulty in interpreting its underlying dynamics, Tang *et al* [A26] simplified the model and reduced its dimensionality. This was done by first ignoring the diffusion terms, turning the PDE model into an ordinary differential equation (ODE) model, followed by assuming that protein biosynthesis in the cell is slow enough, implying that the total amount of each protein is conserved (i.e., constant). This produced the following system of ODEs

$$\frac{dR}{dt} = (I_R + I_K^*)\left(\frac{L_\rho^n}{L_\rho^n + \rho^n}\right)(1 - R - \gamma K) - \delta_R R \tag{7a}$$

$$\frac{d\rho}{dt} = I_\rho\left(\frac{L_R^n}{L_R^n + (R + \gamma K)^n}\right)(1 - \rho) - \delta_\rho \rho \tag{7b}$$

$$\frac{dP}{dt} = B\left(\frac{K^n}{L_K^n + K^n}\right)(1 - P\left(1 + k_G k_C k_X[GIT][PIX][PAK_{tot}]K_i^*\left(1 + \alpha_R R\right)\right)) - \delta_P P, \tag{7c}$$

Parameter	Description	Value	Unit	References
I_R	Basal Rac activation rate	0.0035	s^{-1}	[A26]
δ_R	Rac inactivation rate	0.025	s^{-1}	[A26]
L_ρ	Rho-dependent half-maximum inhibition of Rac	0.34	unitless	[A26]
I_ρ	Basal Rho activation rate	0.016	s^{-1}	[A26]
δ_ρ	Rho inactivation rate	0.016	s^{-1}	[A26]
L_R	Rac-dependent half-maximum inhibition of Rho	0.34	unitless	[A26]
γ	Ratio of total PAK to total Rac	0.3	unitless	[A26]
δ_P	Paxillin dephosphorylation rate	0.00041	s^{-1}	[A26]
n	Hill coefficient	4	unitless	[A26]
L_K	Active PAK-dependent half-maximum activation of paxillin	5.77	unitless	[A26]
I_K	Additional Rac activation due to paxillin	0.009	s^{-1}	[A26]
k_G	Association constant for GIT-PIX binding	5.71	s^{-1}	[A26]
$[GIT]$	Concentration of GIT	0.11	μM	[A26]
k_X	Association constant for PIX-PAK binding	41.7	s^{-1}	[A26]
$[PIX]$	Concentration of PIX	0.069	μM	[A26]
k_C	Association constant for Pax_p-GIT binding	5	s^{-1}	[A26]
$[Pax_{tot}]$	Total concentration of paxillin	2.3	μM	[A26]
α_R	Affinity constant of PAK-RacGTP binding	15	unitless	[A26]

Table 1: Parameter values associated with the original spatiotemporal model given by Eqs. (3).

where $R_i = 1 - R$, $\rho_i = 1 - \rho$ and $P_i = 1 - P\Big(1 + k_G k_C k_X [GIT][PIX][PAK_{tot}]K_i^*(1 + \alpha_R R)\Big)$.

To further simplify this ODE model without modifying its underlying dynamics, several simplifying steps have been implemented here to reduce its dimensionality. In the first step, we apply linear regression on K_i^*, defined by Eq. (6), using the values of paxillin at steady state; this generates the following simplified expression

$$1 - P\Big(1 + k_G k_C k_X [GIT][PIX][PAK_{tot}]K_i^*(1 + \alpha_R R)\Big) \approx 1 - \alpha_P P,$$

where α_P is a parameter (see Table 2). Second, since the dynamics of active Rho (ρ) and phosphorylated paxillin (P) occur at a faster timescale compared to active Rac (R), one can use quasi-steady state approximation (QSSA) to express ρ and P as functions of R. This is done by setting Eqs. (7b) and (7c) to zero to obtain

$$\rho = \frac{I_\rho L_R^n}{I_\rho L_R^n + \delta_\rho \left(L_R^n + (R + \gamma K)^n\right)} \tag{8}$$

$$P = \frac{B\frac{K^n}{L_K^n + K^n}}{\alpha_P B\frac{K^n}{L_K^n + K^n} + \delta_P}. \tag{9}$$

Finally, at steady state, K defined by Eq. (4) can be approximated (through fitting) using an expression that

purely depends on R. This fitted expression is given by

$$K \approx \frac{\alpha_R R}{(1+\alpha_R R) + \frac{k_G k_X [GIT][PIX]}{1+k_X[PIX]+\frac{3}{1+R}}}.$$

The same can be done for I_K^*, defined by Eq. (5), to obtain a simplified expression in terms of R only, given by

$$I_K^* \approx I_K \times \left(1 - \frac{1}{1.5 + k_X[PIX] + k_G k_X k_C [GIT][PIX][Pax_{tot}]P}\right),$$

where P is at steady state defined by Eq. (9).

Taking all these approximations into consideration, including QSSA, produces a 1D ODE model for R, given by

$$\frac{dR}{dt} = (I_R + I_K^*)\left(\frac{L_\rho^n}{L_\rho^n + \rho^n}\right)(1 - R - \gamma K) - \delta_R R, \tag{10}$$

where ρ, K and I_K^* are defined by Eqs. (8), (4) and (5), respectively. This new 1D ODE model is in a closed form as it purely depends on R.

The bistability in R with respect to maximum phosphorylation rate of paxillin B was an important feature of the original ODE model given by Eqs. (7) [A26]. This is further confirmed here by plotting the bifurcation diagram of R with respect to B (Fig. 3A), producing a bistable switch comprised of two branches of stable equilibria (solid lines) linked together by a branch of unstable equilibria (dashed line) at two saddle-node bifurcations. To determine if such bistable switch is preserved by the simplified 1D ODE model, we plot the same type of bifurcation diagram for R in terms of B but use Eq. (10). Doing so produces a bistable switch whose shape and range of hysteresis are similar to that obtained by the original ODE model (Fig. 3B). In both models, bistablity allows for the switching between the uninduced (low active Rac) and induced (high active Rac) states to occur at specific thresholds in B (determined by the saddle-node bifurcations), outside of which the system becomes monostable. These results thus demonstrate that the simplified 1D ODE model, defined by Eq. (10), preserves the key dynamic features of the original ODE model, defined by Eq. (7), and can thus be used to analyse motility.

2.4 Two-dimensional (2D) ODE model with one fast and one slow variable

Studying the impact of bistability on cellular polarization has been previously investigated in detail in past modeling studies [A37, A38]. Because CHO-K1 cells are known to exhibit much more complex migration patterns (manifested as quick increases and decreases in protrusions, indicating variations in the Rac activity) [A31], we have decided to increase the complexity of the 1D ODE model, given by Eq. (10), to allow the modified model to display a whole set of new and interesting dynamics, including oscillations. The goal is to explore how such

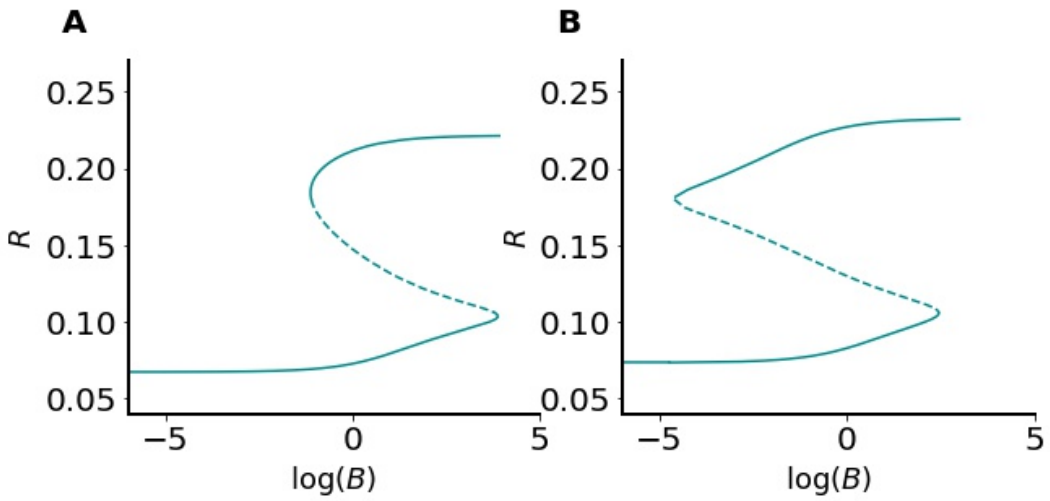

Figure 3: Bistable switch generated by the Rac, Rho and paxillin signaling network. The bifurcation diagram of R with respect to B according to the (A) 6D, and (B) 1D models defined by Eqs. (3) and (10), respectively, when diffusion is ignored. Both diagrams exhibit bistability between the uninduced (low active Rac) and induced (elevated active Rac) states in an almost identical fashion. Solid lines: branches of stable equilibria; dashed lines: branches of unstable equilibria (or saddle fixed points). Solid lines merge with dashed lines at saddle-node bifurcations.

new complex dynamics can impact motility.

With the evidence suggesting that there are potential feedbacks from Rac to maximum phosphorylation rate B, the 1D ODE model is modified here accordingly. This is done by augmenting the 1D ODE model with one additional auxiliary and phenomenological equation that reflects the slow dynamics of paxillin phosphorylation. More specifically, we have turned the parameter B into a slow variable, given by

$$\frac{dB}{dt} = \epsilon \left(1 - \gamma_R R - k_B(B - B_r) + \frac{1}{\eta\,(B - \epsilon_B)}\right),$$

where $0 < \epsilon \ll 1$ is the time constant, $B_r > 0$ is the resting state of B, $k_B > 0$ is the recovery rate to the resting state and $\epsilon_B, \eta > 0$ are parameters. The resulting 2D ODE model becomes

$$\frac{dR}{dt} = (I_R + I_K^*)\left(\frac{L_\rho^n}{L_\rho^n + \rho^n}\right)(1 - R - \gamma K) - \delta_R R \tag{11a}$$

$$\frac{dB}{dt} = \epsilon \left(1 - \gamma_R R - k_B(B - B_r) + \frac{1}{\eta\,(B - \epsilon_B)}\right). \tag{11b}$$

This new 2D ODE model is designed to have B vary very slowly compared to R. This means that R can always converge to a steady state, if it exists, before any substantial variation in B. The slow dynamics of B is depicted here by ϵ. Two important features of this new model include the absence of feedback from B to active

Rac R (i.e., the model is feedforward with B receiving input from R but not vice versa), and the impossibility for B to be negative due to the term $\frac{1}{\eta(B-\epsilon_B)}$ which acts as a barrier.

Equations 11, possess one slow and one fast variable. As before, this model can exhibit bistability for certain parameter values. Indeed, depending on the parameters that govern the variation in B (e.g., k_B and γ_R), the system can either have one or two co-existing stable steady states, when the B-nullcline crosses the "generalized" R-nullcline at stationary points where R is stable (i.e., the lower and upper stable branches of the generalized R-nullcline, see Fig. 4A, B and C). The real interesting dynamic feature of this new model, however, is that it can also exhibit ROs; this occurs when it is in a configuration in which the B-nullcline intersects the generalized R-nullcline in the middle unstable branch (Fig. 5A). This would allow the 2D ODE model to exhibit relaxation oscillations (ROs) along the hysteresis cycle that involves the slow evolution of trajectories along the stable branches of the generalized R-nullcline, because B is slow, and the fast jumps between the two stable branches at the saddle-nodes, because R is fast (Fig. 5B). Having the B-nullcline separating the phase-space into two regions: one above the B-nullcline with $dB/dt < 0$ (B is decreasing) and another below the B-nullcline with $dB/dt > 0$ (B is increasing), causes the trajectories to move to the left (right) below (above) the B-nullcline until they reach the saddle-nodes. Thus for such oscillations to occur, ϵ must be very small and the two nullclines must intersect only once on the middle unstable branch of the cubic-shaped generalized R-nullcline (Fig. 5).

With these ROs, one would expect (as shown later) to obtain a Hopf bifurcation when varying the parameter(s) related to B, or more specifically those that dictate the position of the B-nullcline (e.g., k_B). Indeed, if this parameter variation causes the configuration of the nullclines in Fig. 4A, where the two nullclines intersect at a stable steady state in the upper branch of the generalized R-nullcline, to transition to the one in Fig. 5A, where the two nullclines intersect at an unstable steady state in the middle branch of the generalized R-nullcline, a shift in dynamics from quiescent to oscillatory behaviour would occur right when the intersection of the two nullclines crosses the upper saddle-node bifurcation during this transition. This oscillatory behaviour is eventually manifested as a RO (Fig. 5B).

Interestingly, during the transition from quiescent to the ROs obtained while varying the slope of the B-nullcline (through the parameter k_B), another very interesting dynamics is also observed within a very small parameter regime (Fig. 6A). In this third regime, trajectories exhibit very small amplitude oscillations (SAOs) in both variables: R and B (Fig. 6B). Such oscillations are formed as soon as the stable steady state disappears during the decrease in the slope of the B-nullcline and a new unstable steady state is formed in the middle branch of the generalized R-nullcline. Trajectories, in this case, initially get attracted to the lower stable branch of the generalized R-nullcline causing R to jump from the upper branch at the saddle-node bifurcation; during this jump, however, the fast variable crosses the B-nullcline, causing the slow variable B to increase again. When B

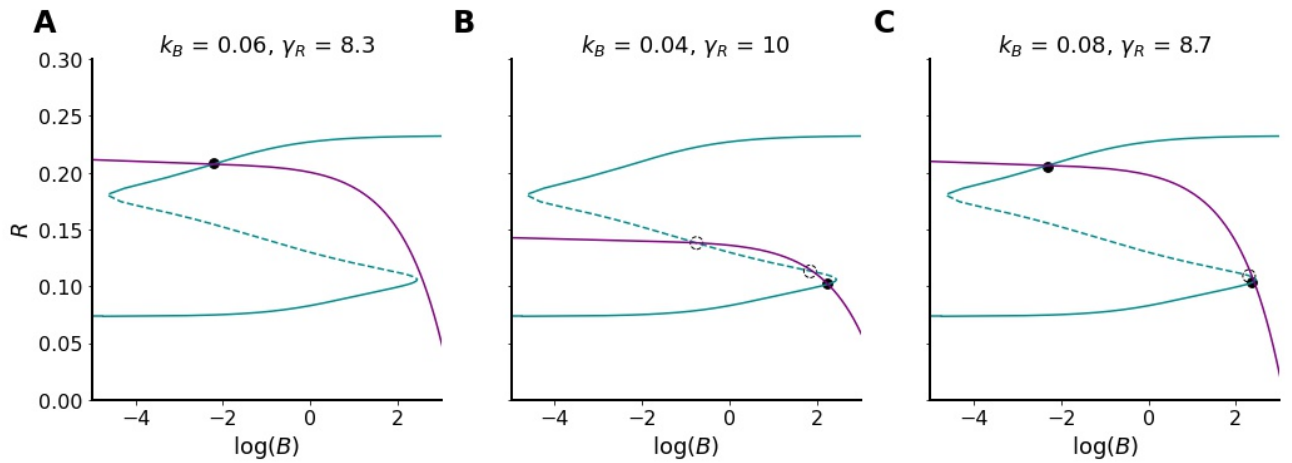

Figure 4: Three possible configurations for the steady states of the 2D ODE model, given by Eqs. 11, lying at the intersection of the B-nullcline (purple) and generalized R-nullcline (blue) obtained when k_B and γ_R are varied but no change is made to the remaining parameter values listed in Tables 1 and 2. In the first two cases, one stable steady state, lying either on the (A) upper or (B) lower stable branch of the generalized R-nullcline is formed between the two nullclines. In the last case, (C) two stable steady states, lying on the upper and lower stable branches of the generalized R-nullcline, are formed. Black solid (empty) circles represent stable (unstable) steady states.

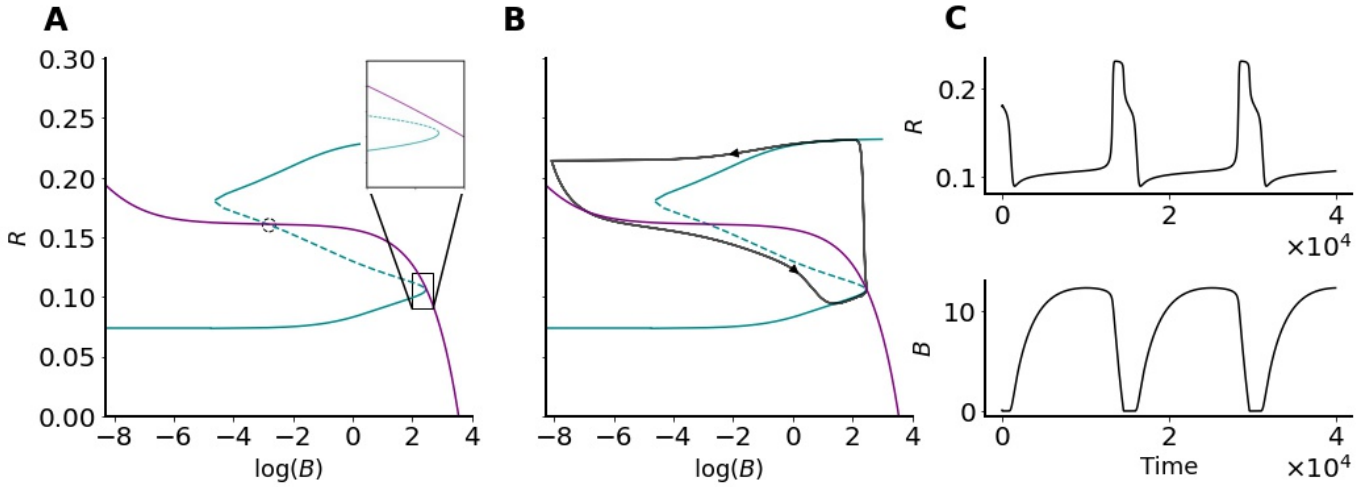

Figure 5: A new configuration for the steady state of the 2D ODE model, given by Eqs. 11, lying at the intersection of the B-nullcline (purple) and generalized R-nullcline (blue) obtained at default parameter values listed in Tables 1 and 2. In this case, (A) only one intersection occurs on the middle unstable branch of the cubic generalized R-nullcline, forming an unstable steady state (open circle). The inset in (A) is a magnification of the box surrounding the bottom saddle-node bifurcation. (B) Stable periodic orbit in the form of ROs (black) is formed around the unstable steady state. The cause for the apparent stretching of the ROs far from the generalized R-nullcline in (A, B) is the use of the logarithmic scale, which considerably expands any small deviation near zero. (C) Time series simulations of R (top) and B (bottom) showing oscillations.

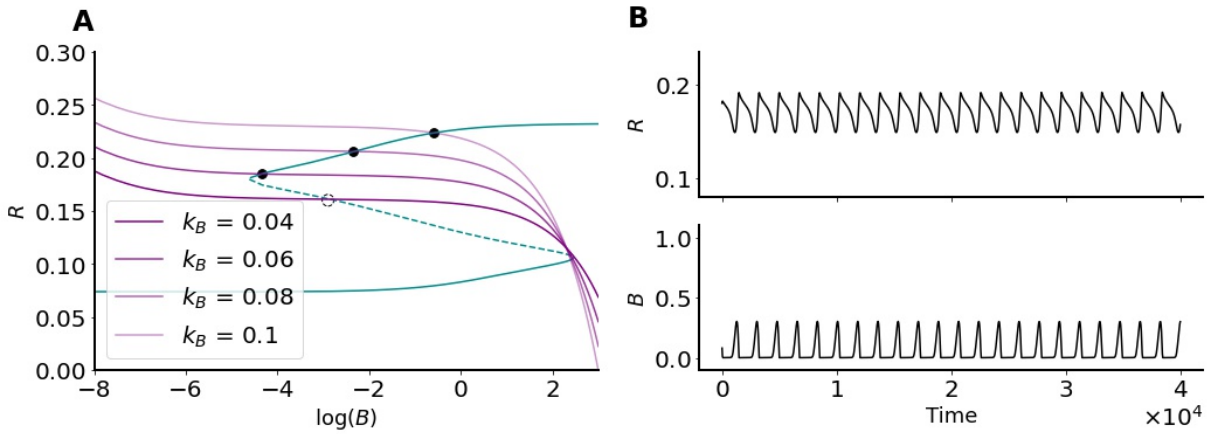

Figure 6: The 2D ODE model, given by Eqs. 11, can exhibit SAOs when varying k_B due to canards. (A) Gradually decreasing the slope of the B-nullcline through k_B, the steady state at the intersection of the generalized R-nullcline (blue) and the B-nullcline (shades of purple) transitions from being stable (lying on the upper branch of the generalized R-nullcline) to being unstable (lying on the middle branch of the generalized R-nullcline). (B) Time series simulations of SAOs displayed by R (top) and B (bottom) formed right after the B-nullcline shifts its intersection with the generalized R-nullcline to the middle branch.

reaches a higher value, it brings the system back to the right of the upper saddle-node bifurcation. Meanwhile, the decrease in R is insufficient to bring the trajectories all the way down to the lower branch, causing them to interrupt their jumps and to return back to the upper branch of the generalized R-nullcline (because of the increase in B). When this happens, the same phenomenon repeats itself again, causing both R and B to generate SAOs (Fig. 6B).

2.4.1 Three-dimensional (3D) ODE model with one fast, one slow and one very slow variable

The SAOs highlighted in the previous section (Fig. 6) occur between the upper stable branch of the generalized R-nullcline and its unstable branch, in the neighbourhood of the upper saddle-node. Further investigation of the 2D ODE model of Eqs. (11) shows that for the trajectories to go back and forth between the quiescent configuration of Fig. 4A to the RO configuration of Fig. 5, one needs to periodically decrease and increase the slope the B-nullcline sufficiently enough. This can be done by targeting the the recovery rate parameter k_B which defines the slope of the B-nullcline. By dynamically varying k_B, the system can travel through the whole spectrum of these regimes highlighted earlier, producing SAOs in combination with ROs in the form of large amplitude oscillations (LAOs). This combination of different amplitude oscillations is called mixed modes oscillations (MMOs).

Keeping that in mind, we have expanded the 2D ODE model into a 3D semi-phenomenological ODE model based on the scheme of Fig. 7 to produce MMOs. The model possesses three different timescales: fast, slow

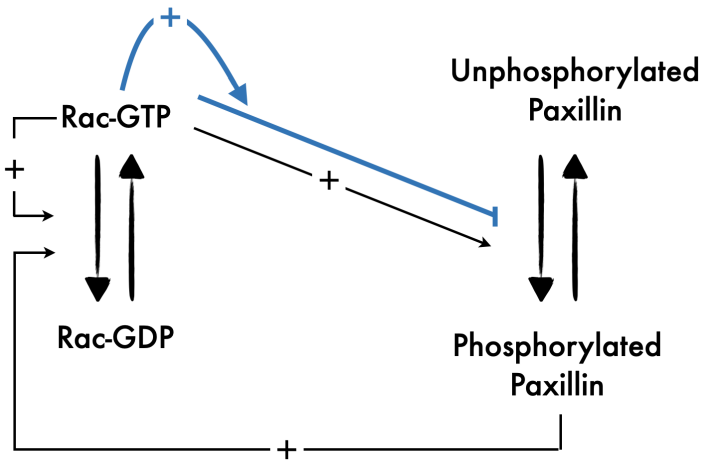

Figure 7: Schematic of the 3D ODE model involving Rac and paxillin in a simplified protein network. Diagram of the signalling pathways included in the 3D ODE model showing Rac cycling between inactive and active forms and the indirect positive auto-feedback (via Rho) on itself through RacGEF. It also shows the positive and negative (blue pathway) feedbacks on paxillin phosphorylation at a fast and a slow timescale, respectively, as well as the indirect upregulation of Rac activation through RacGEF by phosphorylated paxillin. Blue pathway: refinement of the original model from Tang *et al* (2018).

and very slow, to allow for the aforementioned patterns of activity to arise, including MMOs that combine slow large amplitude with fast small amplitude oscillations within one cycle. The fast variables in this new model is R whereas the slow and the very slow variables are the two parameters - turned into variables - B and k_B, respectively. The 3D ODE model is given by

$$\frac{dR}{dt} = (I_R + I_K^*)\left(\frac{L_\rho^n}{L_\rho^n + \rho^n}\right)(1 - R - \gamma K) - \delta_R R \tag{12a}$$

$$\frac{dB}{dt} = \epsilon\left(1 - \gamma_R R - k_B(B - B_r) + \frac{1}{\eta\,(B - \epsilon_B)}\right) \tag{12b}$$

$$\frac{dk_B}{dt} = \epsilon_L\,(\gamma_K - R)\,, \tag{12c}$$

where $0 < \epsilon_L \ll \epsilon < 1$ is the time constant and $\gamma_K > 0$ is a parameter chosen to be between the steady states of R defined by the generalized R-nullcline. The equations for R and B are identical to these in Eqs. (11).

The 3D ODE model of Eqs. (12) is once again feedforward. The new auxiliary equation for recovery variable k_B possesses the slowest timescale defined by ϵ_L, receives input from R in a feedforward manner and allows the system to exhibit oscillations of varying amplitudes and periods. These oscillations are manifested as MMOs in R (Fig. 8).

Parameter	Description	Value	Unit
α_P	Linearization coefficient in paxillin activation	2.7	unitless
ϵ	Time constant for B	0.01	s^{-1}
B_r	Resting state of B	10	unitless
k_B	Recovery rate of B back to its resting state	0.04	unitless
γ_R	Strength of R feedback onto B	8.6956	s^{-1}
η, ϵ_B	Parameters that guarantee the positivity of B	10^4, 10^{-4}	unitless
ϵ_L	Time constant of k_B	10^{-5}	s^{-1}
γ_K	Source term	0.15	unitless

Table 2: Parameter values associated with the 2D and 3D ODE models defined by by Eqs. (11) and (12), respectively.

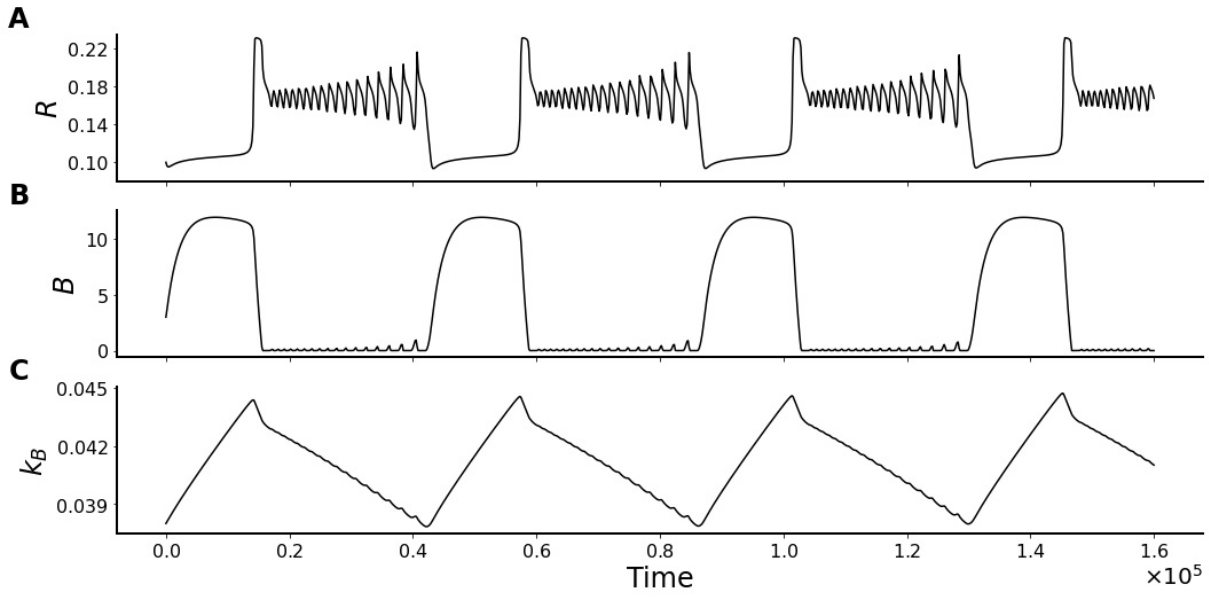

Figure 8: MMOs generated by the 3D ODE model defined by Eqs. (12). Time course simulations of (A) R, (B) B and (C) k_B showing oscillations in each variable with R displaying very pronounced MMOs.

2.4.2 Slow-fast analysis of the 3D ODE model

The MMOs detected in the 3D ODE model of Eqs. (12) (Fig. 8) indicate that there is a quick and exponential increase in the amplitude of these oscillations through a canard explosion. This classical canard phenomenon explains the very fast transition from a small amplitude oscillations (SAO), via canard cycles, to a large amplitude oscillation (LAO), after a Hopf bifurcation. Such very fast transition happens within an exponentially small range of a control parameter, making it difficult to detect. Still, the peculiar shape of the generalized R-nullcline (i.e., the critical manifold of the 3D ODE model) makes our system very prone to developing these canard explosions; indeed, these types of oscillations are always encountered when designing the model and setting different formulations for the B and k_B equations.

Desroches *et al* (2012) [A32] provided a detailed summary of the local mechanisms that give rise to MMOs. As acknowledged in this study, different configurations that can produce MMOs have been widely studied in the presence of folded singularities in the critical manifold. According to this scenario, the simplest form for a system to exhibit MMOs is to have a three-dimensional model with one fast and two slow variables. By investigating the dynamics of the reduced problem, obtained by setting the fast variable to steady state, one could find folded singularities in the critical/slow manifold of the problem and thus explain the presence of MMOs. However, in some cases, there is no folding in the critical manifold, and therefore another less common approach must be applied, where the system is viewed as consisting of two fast variables and one slow one. Here, we adopt this approach with the 3D ODE mode, given by Eqs. (12), by taking R and B to be fast and k_B to be slow. To simplify the analysis, we let

$$\frac{dR}{dt} = (I_R + I_K^*)\left(\frac{L_\rho^n}{L_\rho^n + \rho^n}\right)(1 - R - \gamma K) - \delta_R R =: f(B, k_B, R, \epsilon_L) \tag{13a}$$

$$\frac{dB}{dt} = \epsilon\left(1 - \gamma_R R - k_B(B - B_r) + \frac{1}{\eta\,(B - \epsilon_B)}\right) =: g(B, k_B, R, \epsilon_L) \tag{13b}$$

$$\frac{dk_B}{dt} = \epsilon_L\,(\gamma_K - R) =: \epsilon_L h(R). \tag{13c}$$

Based on this, we can define the layer problem to be

$$\frac{\partial R}{\partial t} = f(B, k_B, R, 0) \tag{14a}$$

$$\frac{\partial B}{\partial t} = g(B, k_B, R, 0) \tag{14b}$$

$$\frac{\partial k_B}{\partial t} = 0, \tag{14c}$$

and the the reduced problem, obtained by transforming the fast time scale t into a slow time scale $T = \epsilon_L t$, to

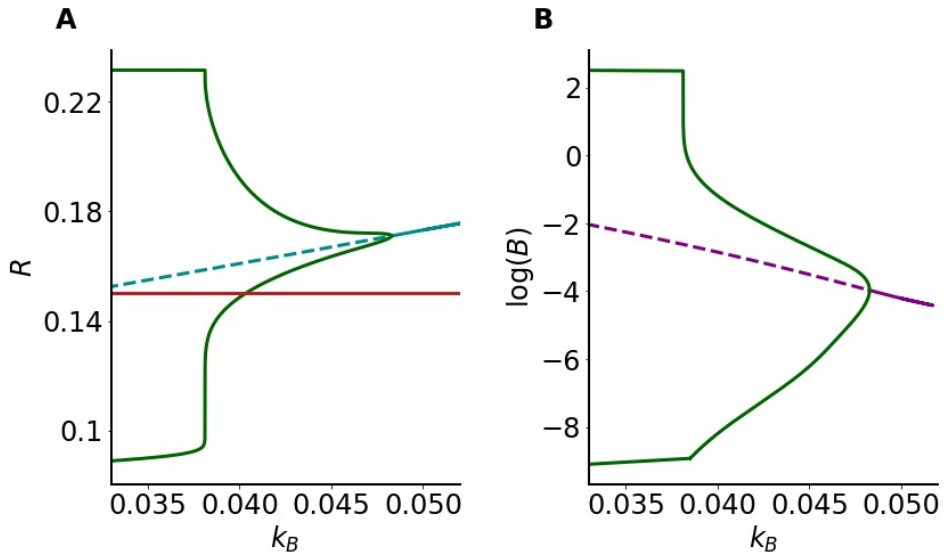

Figure 9: Slow-fast analysis of the 3D ODE model defined by Eqs. (12). Bifurcation diagram of (A) R and (B) B with respect to k_B as defined by the layer problem 14. Solid (dashed) blue and purple lines represent stable (unstable) equilibria. In both panels, the change in stability (i.e., the switch from solid to dashed line) occurs at a supercritical Hopf bifurcation at which two envelopes of stable periodic orbits (solid green), representing the maximum and minimum of the oscillations, emerge. Red line in Panel A is the k_B-nullcline superimposed on the bifurcation diagram.

be

$$\frac{\partial R}{\partial T} = 0 \tag{15a}$$

$$\frac{\partial B}{\partial T} = 0 \tag{15b}$$

$$\frac{\partial k_B}{\partial T} = h(R), \tag{15c}$$

where ϵ_L is set to zero in both problems defined by Eqs. (14) and (15). According to this formalism, the critical manifold is defined to be $S = \left\{(R, B, k_B) : \frac{dR}{dt} = 0\right\}$, which is equivalent to the null-surface of the fast variable R.

With these two problems introduced, we can now plot the bifurcation diagrams of the fast variables with respect to k_B as defined by the layer problem of Eqs. (14) (Fig. 9). Our results reveal that both variables of the fast sub-system, namely, R (Fig. 9A) and B (Fig. 9B), undergo a supercritical Hopf bifurcation when decreasing k_B at $k_{BHopf} \approx 0.048$. Two envelopes of stable periodic orbits representing the maximum and minimum of the oscillations emanate from the Hopf bifurcation. The amplitude of the oscillations increases exponentially fast in the form of a canard explosion until these envelops eventually plateau starting from approximately $k_{BLAO} \approx 0.038$ (estimated using AUTO-07p [A39]) towards smaller values of k_B. The periodic orbits associated with canard

explosion seen in the bifurcation diagrams of R and B (Fig. 9A and B, respectively) are ROs that partially contribute to the formation of the LAOs in the MMOs. Due to the fact that these oscillations appear at $k_{BLAO} < k_{BHopf}$, the Hopf bifurcation in this case is referred to as delayed Hopf. In our subsequent analysis, we use the phrase "active phase" of the system to refer to the configuration when k_B is between k_{BLAO} and k_{BHopf}.

To further investigate how SAOs and LAOs form MMOs, we now turn our attention to the reduced problem, given by System 15. By superimposing the nullcline of k_B on the bifurcation diagram of R with respect to k_B (Fig. 9A), we can see that the dynamic of the full 3D ODE model is dictated by how long trajectories spend time below or above the k_B-nullcline. Indeed, if the average value of R, calculated over an entire SAO cycle, is bigger than γ_K, then k_B will decrease (since the average $dk_B/dt < 0$), causing the trajectory to move to the left in Fig. 9. If the opposite happens, then the trajectory moves to the right. Such mechanism is similar to that seen in parabolic bursting [A40].

To verify if this is the mechanism underlying MMOs, one cycle of the solution trajectory of the full 3D ODE model, given by Eqs. (12), is superimposed onto the bifurcation diagram of R with respect to k_B (Fig. 10A). Doing so shows that the trajectory initially moves to the left while exhibiting SAOs delimited by the two envelopes of the periodic orbits to the right of the canard explosion because it spends more time above the k_B-nullcline. Thus, the number of spikes during the active phase is directly linked to the time constant of k_B, because the time the system spends in the active phase depends on how fast k_B decreases. However, when the trajectory crosses k_{BLAO} and enters the relaxation oscillation regime, it starts spending more time below the k_B-nullcline causing it to travel to the right (recall that we have $R_{low} < \gamma_K < R_{high}$).

Notice here that, according to the configuration of Fig. 10A, the trajectory does not spend too much time in the RO regime, as it leaves very soon after by moving to the right away from the periodic envelopes. The contribution of ROs (through the canard explosion) to the MMOs is therefore limited. Interestingly, when the trajectory moves to the right, it peculiarly does not follow a specific manifold and suddenly changes direction upward by forming a very prominent LAO. The configuration of Fig. 10A is thus not sufficient to explain all the dynamics.

To explain the underlying dynamics of this very last component of the solution trajectory showing the prominent LAO, it is necessary to expand our slow-fast analysis to include B. This is done in Fig. 10B, where we plot the critical manifold of the layer problem, given by Eqs. (14), and the B-nullsurface along with one cycle from the solution trajectory of the full 3D ODE model to view how it evolves with respect to both of these surfaces. Our results reveal that towards the end of the last SAO (which is becoming a LAO), the trajectory reaches the lower stable sheet of the critical manifold. When this happens, the trajectory ends up being below the B-nullsurface in a region where $dB/dt > 0$, causing it to travel right along this stable sheet until it reaches the fold (the

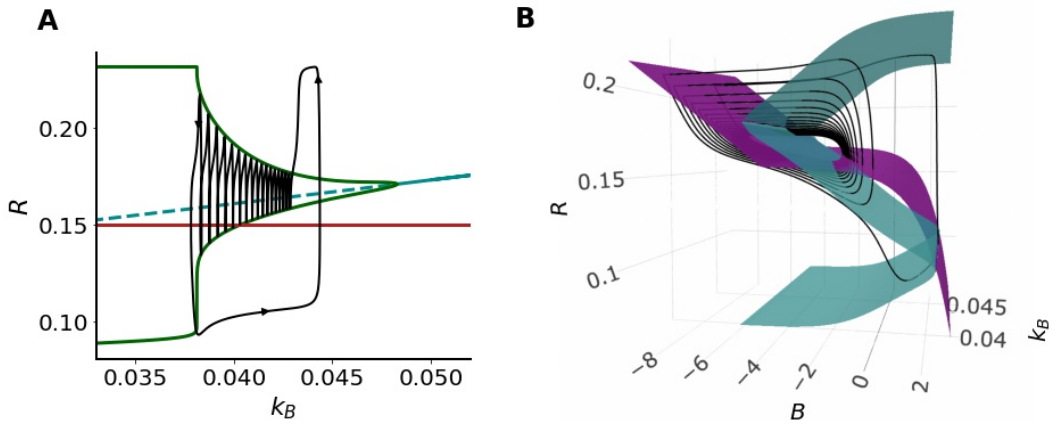

Figure 10: Underlying dynamics of MMOs produced by the 3D ODE model defined by Eqs. (12). (A) Solution trajectory (black line) superimposed in the bifurcation diagram of R with respect to k_B previously plotted in Fig 9. (B) The critical manifold S (blue) along with the B-nullsurface (purple) showing how they govern the dynamics of a solution trajectory (black) over time.

saddle-node); this produces the lower plateau part of the trajectory in Fig. 10A right after leaving the oscillatory regime. At the fold, the trajectory then jumps up to the upper stable sheet of the critical manifold of Fig. 10B (because R is fast), crossing the B-nullsurface into a region where $dB/dt < 0$, causing the trajectory to travel to the left briefly along the upper sheet until it crosses the B-nullsurface all over again (Fig. 10B). Because B has slow time scale, trajectory then moves downward and slightly to the left along the B-nullsurface until it enters the oscillatory regime determined by k_B. The full cycle of jumping up, and down with a short plateau in between form the LAO seen in Fig. 10A.

2.4.3 Spatiotemporal dynamic in the presence of diffusion

By reintroducing diffusion into the R equation of the 1D and 3D ODE models, given by Eqs.(10) and (12), respectively, one can investigate the spatiotemporal dynamic of Rac according to these models. In order to do this in the context of cell motility, however, one also needs to reintroduce the equation that govern the dynamics of inactive Rac (R_i). This produces, as a result, two spatiotemporal models that we label as the 2D and 4D PDE models, respectively.

2.4.3.1 Wave-pinning in the 2D PDE model A hallmark of cell motility and cell polarization is the formation of a stable inhomogeneous pattern in molecular concentrations between the front and the rear of a polarized cell [A41]. Such a pattern has been previously referred to as wave-pinning [A38,A42]; it is a spatiotemporal phenomenon that describes the propagation of a front of higher protein concentration, originating from a perturbation of a homogeneous low steady state, and the stabilization of the front, creating a restricted region with high

concentration of an active protein at steady state. It is an inherent property of some reaction-diffusion systems possessing bistability, and relies on two important biophysical assumptions, namely, that matter is conserved and that there is a difference in diffusion coefficients between the chemical species under consideration [A38, A42].

As an example, let us consider the 2D PDE model, given by

$$\frac{\partial R}{\partial t} = (I_R + I_K^*)\left(\frac{L_\rho^n}{L_\rho^n + \rho^n}\right)(1 - R - \gamma K) - \delta_R R + D_R \frac{\partial^2 R}{\partial x^2} \tag{16a}$$

$$\frac{\partial R_i}{\partial t} = -(I_R + I_K^*)\left(\frac{L_\rho^n}{L_\rho^n + \rho^n}\right)(1 - R - \gamma K) + \delta_R R + D_{R_i} \frac{\partial^2 R_i}{\partial x^2}, \tag{16b}$$

where ρ is defined by Eq. (8). This model depends purely on active (R) and inactive (R_i) Rac in a closed form, is conserved and possesses differences in diffusion coefficients between its two molecular species: R and R_i. In other words, it has all the ingredients necessary to produce wave-pinning.

To verify this, the model is simulated over time on a one-dimensional spatial domain by initiating it from non-homogeneous initial condition (Fig. 11). A step function with $R = 0.083$ for $x \leq 30$ and $R = 0.2269$ for $x > 30$ (which correspond, respectively, to the stable low and high equilibria of R in the 1D ODE model) is used as an initial condition. By doing so, we obtain the wave-pinning phenomenon comprised of elevated R in the "front" and low R in the "back" (Fig. 11A). This spatiotemporal phenomenon remained stable at steady state due to the low diffusion coefficient of R. In contrast, the high diffusion coefficient of R_i prevented this from happening, leading R_i to become homogeneous at steady state (Fig. 11B). This result thus confirms that the reduced 2D PDE model of Eqs. 16 can produce wave-pinning in Rac in a manner similar to that seen with the 6D PDE model [A26].

2.4.3.2 Spatiotemporal dynamics of the 4D PDE model To explore how MMOs affect the spatiotemporal patterns generated by Rac, we turn our attention now to the 4D PDE given by

$$\frac{\partial R}{\partial t} = (I_R + I_K^*)\left(\frac{L_\rho^n}{L_\rho^n + \rho^n}\right)(1 - R - \gamma K) - \delta_R R + D_R \frac{\partial^2 R}{\partial x^2} \tag{17a}$$

$$\frac{\partial R_i}{\partial t} = -(I_R + I_K^*)\left(\frac{L_\rho^n}{L_\rho^n + \rho^n}\right)(1 - R - \gamma K) + \delta_R R + D_{R_i} \frac{\partial^2 R_i}{\partial x^2} \tag{17b}$$

$$\frac{\partial B}{\partial t} = \epsilon\left(1 - \gamma_R R - k_B(B - B_r) + \frac{1}{\eta\,(B - \epsilon_B)}\right) \tag{17c}$$

$$\frac{\partial k_B}{\partial t} = \epsilon_L(\gamma_K - R). \tag{17d}$$

The numerical instability of this model makes it quite difficult to simulate it over time on a one-dimensional domain. To overcome this obstacle, we revert k_B to being a parameter and analyze the dynamics of the resulting

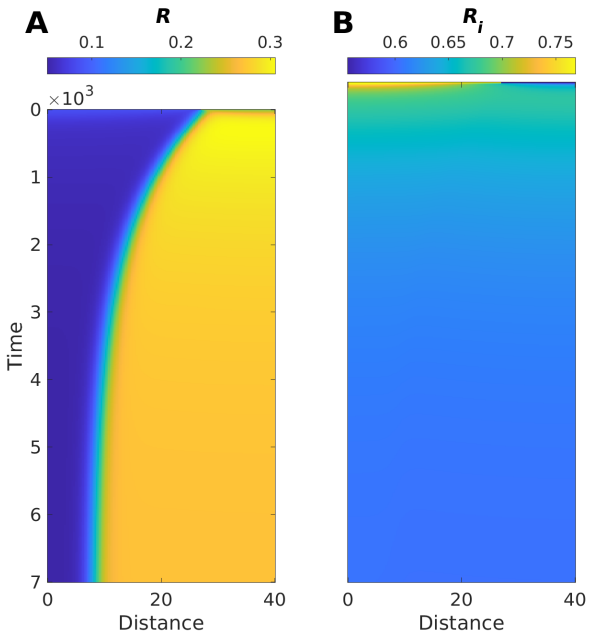

Figure 11: Wave-pinning in a one-dimensional spatial domain generated by the 2D PDE model, given by Eqs. (16). Kymographs of (A) R and (B) R_i when a step-function is used as an initial condition, with zero-flux boundary conditions. The kymographs are color-coded according to the color-map in each panel. R_i is homogeneous, having $D_{R_i} \gg D_R$, whereas R exhibits a front that eventually gets pinned. Longer simulations indicate that the front stays indefinitely in a fixed position, preventing the homogenization of the domain in terms of R. Time and distance are dimensionless.

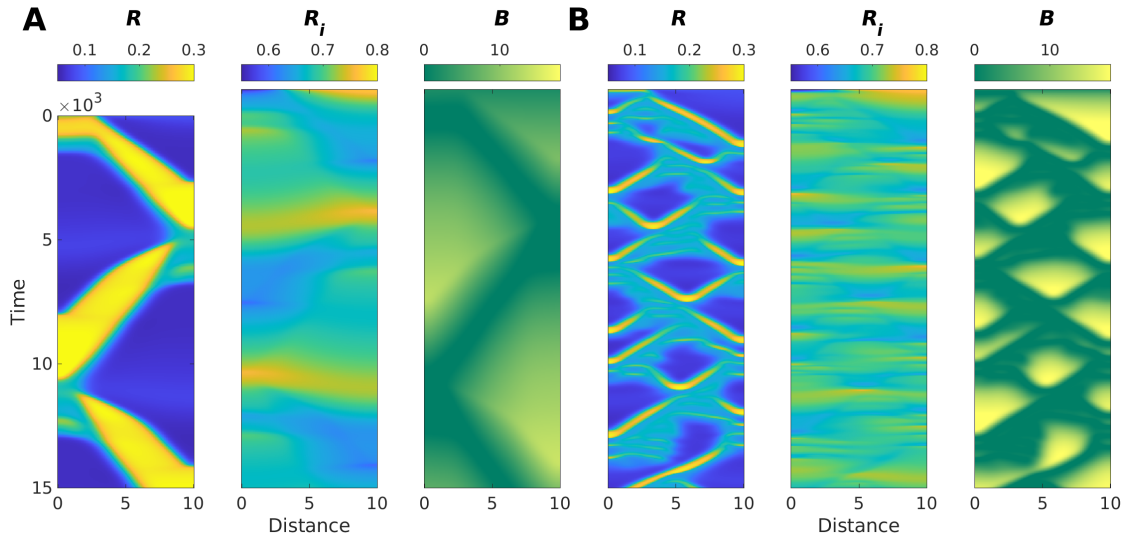

Figure 12: Switching and ripples produced by the 4D PDE model, given by 17, when k_B is set to a constant. Kymographs of R (left) R_i (middle) and B (right) in two parameter regimes defined by k_B: (A) The RO regime and (B) SAO regime. A step-function is used as an initial condition, with zero-flux boundary conditions. The kymographs are color-coded according to the color-map in each panel.

3D PDE model in two different parameter regimes associated with k_B: one that produces ROs and another that produces SAOs (as defined by the 2D ODE model of Eqs. (11)).

Our results show that, by simulating this 3D PDE model of active (R), and inactive (R_i) Rac and B in the RO regime, we obtain intermittent polarization that switches orientation back and forth as time evolves (Fig. 12A). In the SAO regime, however, the entire domain shows small ripples that are present in all variables, especially in R (Fig. 12B). Interestingly, the switching in the level of the three variables in the SAO regime at the boundary of the domain is less pronounced than those seen in the RO regime (compare Fig. 12A to B), but the scaled concentrations across the domain are more heterogeneous.

The fact that k_B varies slowly between these two dynamic behaviours in the 4D PDE model, given by Eqs. (17), indicates that a mixture of these outcomes should be observed periodically. In other words, we expect the 4D PDE model to show a succession of the behaviours detected in the two regimes displayed in Figure 12. Such a mixture of dynamic outcomes can potentially act as a framework that allows cells to exhibit not only change in Rac localization, but also membrane oscillations and fast directionality variations.

2.5 Computer simulations of motile cells

Cellular Potts Models (CPMs) have recently received quite a bit of attention as a tool to simulate "cells" in two-dimensional grid to investigate how different mechanical and chemical forces affect cellular migration [A30, A43, A44]. It is an iterative discrete grid-based stochastic simulation technique that involves the modelling

of the extracellular matrix (ECM) as a mesh upon which simulated cells are superimposed. This computational technique is used here as a framework to explore the migration patterns that can be generated by the 4D PDE model in combination with stochasticity.

2.5.1 Numerical implementation of the CPM

Each simulated CPM cell is modelled as a compartmentalized object that can grow, undergo shape variations and move on the surface of the grid. To account for forces $\mathbf{F}$ affecting cell shape and movement, such as elastic restoring forces or pressure caused by actin filaments growth that push the membrane outward, a Hamiltonian function $H(\mathbf{F};\boldsymbol{\lambda})$ is designed with different weights given by $\boldsymbol{\lambda}$. Monte Carlo Markov Chain-like simulations are then implemented based on the energy expressed by the Hamiltonian, to generate successive configurations of the cell body. Such configurations dictate how cell membrane evolves over time according to the physical forces included in the Hamiltonian. One can use *Morpheus*, a highly flexible CPM simulator software [A45], to incorporate multi-scale systems into this computational technique to simulate a migrating cell.

In the analysis presented here, we combine the 4D PDE model, given by Eqs. (17), with the CPM simulations. This is done by incorporating the chemical reactions of the PDE model along with diffusion to dictate how membrane protrusions are regulated. The main assumption made in these simulations is that elevated Rac causes localized membrane protrusions. In our settings, we set the Hamiltonian function to be

$$H = \lambda_P \left(p_{\sigma,t} - P_{target}\right)^2 + \lambda_S \left(s_{\sigma,t} - S_{target}\right)^2 + \lambda_{Act} \left(\Pi_{u\in M(\sigma,t)} Act\left(u\right)\right),$$

where σ denotes the configuration of the cell at time t, the weights λ_P and λ_S describe the deformation resistance with values tuned to allow the CPM cell to exhibit reasonable membrane elasticity properties [A46, A47], $M(\sigma,t)$ denotes the set of lattices that form the membrane of the cell and the *Act* function measures the amount of actin activity at a specific location. According to this model, protrusions are favoured in the regions of elevated Rac thanks to the *Act* function. Details of the Morpheus implementation can be found in [A45].

2.5.2 Outcomes of the CPM simulations

As highlighted previously, the 4D PDE model, given by Eqs. 17, possesses different time scales; the presence of these time scales have been shown to be crucial for producing complex spatiotemporal patterns, induced by a combination of ROs and SAOs in the form of MMOs. It would be thus interesting to explore how these patterns affect migration paths of simulated cells generated using the CPM.

To study the migration paths of CPM cells, the boundary of these cells is initially computed using binary

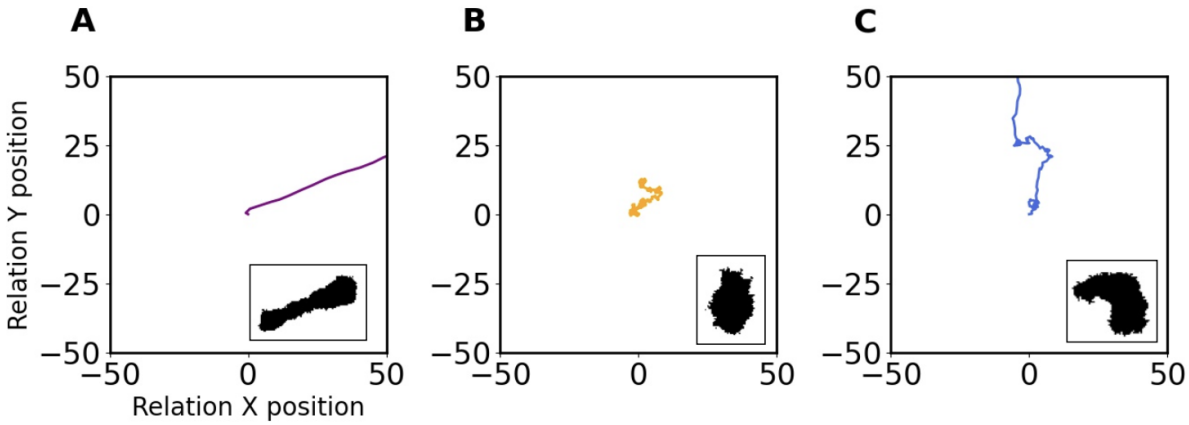

Figure 13: Migration patterns detected in the CPM. Migration paths of simulated CPM cells exhibiting (A) directed, (B) non-motile and (C) meandering motion. Insets: Binary masks of CPM cells at a given frame of the Monte Carlo simulations.

masks, defined as the black and white pixelation of the domain where each pixel occupied (unoccupied) by the cell is colored black (white), and their center of mass is determined at each frame generated by the Monte Carlo simulations. The x and y position of the center of mass of each frame is then tracked to generate the migration path. With this analysis, we have found that these paths display three distinct migration patterns. In the first one, CPM cells exhibit the classic *directional* motion that is typically associated with wave-pinning (Fig. 13A). These cells are fast, unidirectional (i.e., rush in one direction) and possess a stable front (back) with high (low) R. In the second pattern, simulated CPM cells display a homogeneous cytoplasm in terms of R and are non-motile (Fig. 13B). They nonetheless exhibit fluctuations in their membrane and small divergence away from their initial position due to the inherent stochasticity of the Monte Carlo simulation. Finally, in the third pattern, simulated cells show oscillations as well as meandering motion (Fig. 13C). More specifically, these cells protrude episodically and move more substantially than those simulated cells detected in the second pattern. Their membranes display waving patterns, and sometimes stretch because of multiple protruding fronts that dynamically change localization. No straight migratory patterns emerge in these CPM cells, because of this episodic activity in protrusions and retractions. This causes the simulated cells in this migration pattern to exhibit meandering trajectories typical of many migrating mesenchymal cells (such as CHO-K1 cells) [A31]. This seems to suggest that MMOs are important for generating such migration pattern.

2.6 Discussion

Understanding molecular mechanisms underlying excitability in cell motility is a very challenging task due to the wide variability and complexity of the biological network involved. Redundancy in the signalling pathways, stochasticity in molecular expression and the nonlinearity associated with the processes underlying cell motility make investigating the role of excitability in this system very challenging experimentally. Therefore, one can use mathematical modeling as an alternative approach to decipher the dynamics of cell motility, including excitability, in different conditions.

In this present study, we used this modeling approach to uncover the oscillatory mechanisms that can arise in a molecularly-explicit model of cell motility. By focusing on a pre-existing 6D PDE model that describes closely the dynamics of the scaled concentrations of active and inactive forms of Rac and Rho (two members of the Rho family of GTPases that define cellular polarity), as well as of phosphorylated and unphosphorylated forms of the adaptor protein paxillin (an adhesion protein) [A26], we were able to initially simply the model into a 1D ODE model by ignoring diffusion and by using a combination of linear regression and QSSA. The 1D ODE model described the dynamics of scaled active Rac concentration (R) and produced outcomes very similar to those produced by the original PDE model when diffusion was ignored, including bistability.

The simplified model was then successively expanded by phenomenologically turning two of its key parameters to slow and very slow variables. This expansion allowed the resulting 2D and 3D ODE models to produce ROs and MMOs in addition to bistability seen in the original model. The two parameters targeted in these expansions were the phosphorylation rate of paxillin B and the recovery rate k_B. By applying slow fast analysis on the 2D and 3D ODE model, we determined how these oscillations are regulated by the critical manifold of this system and by the different time scales included. More specifically, by focusing on the 3D ODE model, we demonstrated how SAOs and LAOs in MMOs seen in scaled active Rac concentration were generated by considering the layer and reduced problems obtained from the timescale separation. Based on this analysis, we concluded that MMOs are due to both canard explosion and delayed Hopf bifurcation [A32].

Whereas MMOs usually arise from folded singularities [A32], the 3D ODE model analyzed here behaved differently. By choosing to decipher the dynamics of this model using two time scales: two fast (R and B) and one slow (k_B) variables, we showed that the SAOs in MMOs start with very low amplitude but gradually grow before entering the RO regime; during this process the oscillations evolve from being canards without head to becoming canards with head in the RO regime in a manner similar to that governed by delay in a dynamical Hopf bifurcation [A32]. By expanding the analysis to two time scales: one fast (R) and one slow (B), we then demonstrated that the last LAO in the MMOs was due to slow propagation of the trajectory along the two attracting sheets of the critical manifold and jump between them across the B nullcline.

While it is generally accepted that the small GTPases Rac and Rho are responsible for cell motility, most of the standard existing mathematical models only account for polarized cells with a leading front and a stable back that do not display a behavior more complex than straight directed motion. Some relevant models happen to produce oscillations [A29, A37], but they rely on external feedbacks such as adhesion dynamic and signalling from the extra-cellular matrix, as well as do not exhibit frequent directionality change. Here we choose to focus only on internal pathways, and take advantage of the unusual structure and shape of the critical manifold and of the time-scale separation to show that these three internal variables are sufficient to build a model capable of generating complex oscillatory phenomena. This was verified when simulating the 2D and 4D PDE models considered in this study. The spatiotemporal patterns generated by the latter especially revealed that a mixture of switching between front and back as well as ripples across the one-dimensional domain can be obtained. This allowed the simulated CPM cell to exhibit three migration patterns that are quite distinct: directed, meandering and non-motile motions. The latter two appeared quite consistent with those migration patterns detected in CHO-K1 cells [A31].

What are the functional and physiological consequences of the MMOs in this chemical system of cell motility is still to be determined. One needs to quantitatively compare the migration patterns generated by the CPM cells with those generated by mesenchymal cells (e.g. CHO-K1 cells), in a rigourous manner that should be applicable to both systems. This would allow for important conclusions to be drawn about the role of MMOs in defining cell migration.

References

[A1] Eugene M Izhikevich. Neural excitability, spiking and bursting. *International journal of bifurcation and chaos*, 10(06):1171–1266, 2000.

[A2] John Rinzel and G Bard Ermentrout. Analysis of neural excitability and oscillations. *Methods in neuronal modeling*, 2:251–292, 1998.

[A3] Rob J De Boer and Alan S Perelson. Target cell limited and immune control models of hiv infection: a comparison. *Journal of theoretical Biology*, 190(3):201–214, 1998.

[A4] Steven A Prescott. Excitability: Types i, ii, and iii., 2014.

[A5] Steven A Prescott, Yves De Koninck, and Terrence J Sejnowski. Biophysical basis for three distinct dynamical mechanisms of action potential initiation. *PLoS computational biology*, 4(10):e1000198, 2008.

[A6] Zhiguo Zhao, Li Li, and Huaguang Gu. Different dynamical behaviors induced by slow excitatory feedback for type ii and iii excitabilities. *Scientific Reports*, 10(1):1–16, 2020.

[A7] Alan L Hodgkin. The local electric changes associated with repetitive action in a non-medullated axon. *The Journal of physiology*, 107(2):165, 1948.

[A8] Ilan D Zipkin, Rachel M Kindt, and Cynthia J Kenyon. Role of a new rho family member in cell migration and axon guidance in c. elegans. *Cell*, 90(5):883–894, 1997.

[A9] Elena Scarpa and Roberto Mayor. Collective cell migration in development. *Journal of Cell Biology*, 212(2):143–155, 2016.

[A10] Li Li, Yong He, Min Zhao, and Jianxin Jiang. Collective cell migration: Implications for wound healing and cancer invasion. *Burns & trauma*, 1(1):2321–3868, 2013.

[A11] Douglas Hanahan and Robert A Weinberg. Hallmarks of cancer: the next generation. *cell*, 144(5):646–674, 2011.

[A12] Atef Asnacios and Olivier Hamant. The mechanics behind cell polarity. *Trends in cell biology*, 22(11):584–591, 2012.

[A13] Athanasius FM Marée, Alexandra Jilkine, Adriana Dawes, Verônica A Grieneisen, and Leah Edelstein-Keshet. Polarization and movement of keratocytes: a multiscale modelling approach. *Bulletin of mathematical biology*, 68(5):1169–1211, 2006.

[A14] Erin L Barnhart, Jun Allard, Sunny S Lou, Julie A Theriot, and Alex Mogilner. Adhesion-dependent wave generation in crawling cells. *Current Biology*, 27(1):27–38, 2017.

[A15] Laurent MacKay, Etienne Lehman, and Anmar Khadra. Deciphering the dynamics of lamellipodium in a fish keratocytes model. *Journal of Theoretical Biology*, 512:110534, 2021.

[A16] Sabina E Winograd-Katz, Reinhard Fässler, Benjamin Geiger, and Kyle R Legate. The integrin adhesome: from genes and proteins to human disease. *Nature reviews Molecular cell biology*, 15(4):273–288, 2014.

[A17] Satyajit K Mitra, Daniel A Hanson, and David D Schlaepfer. Focal adhesion kinase: in command and control of cell motility. *Nature reviews Molecular cell biology*, 6(1):56–68, 2005.

[A18] Cord Brakebusch and Reinhard Fässler. The integrin–actin connection, an eternal love affair. *The EMBO journal*, 22(10):2324–2333, 2003.

[A19] Catherine D Nobes and Alan Hall. Rho, rac, and cdc42 gtpases regulate the assembly of multimolecular focal complexes associated with actin stress fibers, lamellipodia, and filopodia. *Cell*, 81(1):53–62, 1995.

[A20] Anne J Ridley, Hugh F Paterson, Caroline L Johnston, Dagmar Diekmann, and Alan Hall. The small gtp-binding protein rac regulates growth factor-induced membrane ruffling. *Cell*, 70(3):401–410, 1992.

[A21] Anne J Ridley. Rho gtpases and cell migration. *Journal of cell science*, 114(15):2713–2722, 2001.

[A22] Sarah J Heasman and Anne J Ridley. Mammalian rho gtpases: new insights into their functions from in vivo studies. *Nature reviews Molecular cell biology*, 9(9):690–701, 2008.

[A23] Anjana Nayal, Donna J Webb, Claire M Brown, Erik M Schaefer, Miguel Vicente-Manzanares, and Alan Rick Horwitz. Paxillin phosphorylation at ser273 localizes a git1–pix–pak complex and regulates adhesion and protrusion dynamics. *The Journal of cell biology*, 173(4):587–589, 2006.

[A24] Keith Burridge and Krister Wennerberg. Rho and rac take center stage. *Cell*, 116(2):167–179, 2004.

[A25] Abira Rajah, Colton G Boudreau, Alina Ilie, Tse-Luen Wee, Kaixi Tang, Aleksandar Z Borisov, John Orlowski, and Claire M Brown. Paxillin s273 phosphorylation regulates adhesion dynamics and cell migration through a common protein complex with pak1 and βpix. *Scientific reports*, 9(1):1–20, 2019.

[A26] Kaixi Tang, Colton G Boudreau, Claire M Brown, and Anmar Khadra. Paxillin phosphorylation at serine 273 and its effects on rac, rho and adhesion dynamics. *PLoS computational biology*, 14(7):e1006303, 2018.

[A27] William R Holmes, May Anne Mata, and Leah Edelstein-Keshet. Local perturbation analysis: a computational tool for biophysical reaction-diffusion models. *Biophysical journal*, 108(2):230–236, 2015.

[A28] Sulagna Das, Taofei Yin, Qingfen Yang, Jingqiao Zhang, Yi I Wu, and Ji Yu. Single-molecule tracking of small gtpase rac1 uncovers spatial regulation of membrane translocation and mechanism for polarized signaling. *Proceedings of the National Academy of Sciences*, 112(3):E267–E276, 2015.

[A29] Elisabeth G Rens and Leah Edelstein-Keshet. Cellular tango: how extracellular matrix adhesion choreographs rac-rho signaling and cell movement. *Physical biology*, 18(6):066005, 2021.

[A30] Athanasius FM Marée, Verônica A Grieneisen, and Paulien Hogeweg. The cellular potts model and biophysical properties of cells, tissues and morphogenesis. In *Single-cell-based models in biology and medicine*, pages 107–136. Springer, 2007.

[A31] Lucie Plazen, Jalal Al Rahbani, Claire M Brown, and Anmar Khadra. Polarity and mixed-mode oscillations may underlie different patterns of cellular migration. *Scientific Report, under review*, 2022.

[A32] Mathieu Desroches, John Guckenheimer, Bernd Krauskopf, Christian Kuehn, Hinke M Osinga, and Martin Wechselberger. Mixed-mode oscillations with multiple time scales. *Siam Review*, 54(2):211–288, 2012.

[A33] Mathieu Desroches, Tasso J Kaper, and Martin Krupa. Mixed-mode bursting oscillations: Dynamics created by a slow passage through spike-adding canard explosion in a square-wave burster. *Chaos: An Interdisciplinary Journal of Nonlinear Science*, 23(4):046106, 2013.

[A34] Peter Szmolyan and Martin Wechselberger. Canards in r3. *Journal of Differential Equations*, 177(2):419–453, 2001.

[A35] Valery Petrov, Stephen K Scott, and Kenneth Showalter. Mixed-mode oscillations in chemical systems. *The Journal of chemical physics*, 97(9):6191–6198, 1992.

[A36] Jessica K Lyda, Zhang L Tan, Abira Rajah, Asheesh Momi, Laurent Mackay, Claire M Brown, and Anmar Khadra. Rac activation is key to cell motility and directionality: an experimental and modelling investigation. *Computational and Structural Biotechnology Journal*, 17:1436–1452, 2019.

[A37] William R Holmes, JinSeok Park, Andre Levchenko, and Leah Edelstein-Keshet. A mathematical model coupling polarity signaling to cell adhesion explains diverse cell migration patterns. *PLoS computational biology*, 13(5):e1005524, 2017.

[A38] Yoichiro Mori, Alexandra Jilkine, and Leah Edelstein-Keshet. Wave-pinning and cell polarity from a bistable reaction-diffusion system. *Biophysical journal*, 94(9):3684–3697, 2008.

[A39] Eusebius J Doedel, Volodymyr A Romanov, Randy C Paffenroth, Herbert B Keller, Donald J Dichmann, Jorge Galán-Vioque, and André Vanderbauwhede. Elemental periodic orbits associated with the libration points in the circular restricted 3-body problem. *International Journal of Bifurcation and Chaos*, 17(08):2625–2677, 2007.

[A40] R Bertram et al. Topological and phenomenological classification of bursting oscillations. *Bulletin of mathematical biology*, 57(3):413–39, 1995. Mathematical Neuroscience.

[A41] David G Drubin and W James Nelson. Origins of cell polarity. *Cell*, 84(3):335–344, 1996.

[A42] Yoichiro Mori, Alexandra Jilkine, and Leah Edelstein-Keshet. Asymptotic and bifurcation analysis of wave-pinning in a reaction-diffusion model for cell polarization. *SIAM Journal on applied mathematics*, 71(4):1401–1427, 2011.

[A43] Elisabeth G Rens and Leah Edelstein-Keshet. From energy to cellular forces in the cellular potts model: An algorithmic approach. *PLoS computational biology*, 15(12):e1007459, 2019.

[A44] Noriyuki Bob Ouchi, James A Glazier, Jean-Paul Rieu, Arpita Upadhyaya, and Yasuji Sawada. Improving the realism of the cellular potts model in simulations of biological cells. *Physica A: Statistical Mechanics and its Applications*, 329(3-4):451–458, 2003.

[A45] Jörn Starruß, Walter de Back, Lutz Brusch, and Andreas Deutsch. Morpheus: a user-friendly modeling environment for multiscale and multicellular systems biology. *Bioinformatics*, 30(9):1331–1332, 01 2014.

[A46] François Graner and James A. Glazier. Simulation of biological cell sorting using a two-dimensional extended potts model. *Physical Review Letters*, 69(13):2013 – 2016, 1992.

[A47] Ioana Niculescu, Johannes Textor, and Rob J. de Boer. Crawling and gliding: A computational model for shape-driven cell migration. *PLOS Computational Biology*, 11, 10 2015.

3 Polarity and mixed-mode oscillations may underlie different patterns of cellular migration

Manuscript

Lucie Plazen[1], Jalal Al Rahbani[2], Claire M. Brown[2,3,4,5], Anmar Khadra[2,*]

[1]Department of Mathematics and Statistics, McGill University, Montreal, Canada

[2]Department of Physiology, McGill University, Montreal, Canada

[3]Advanced BioImaging Facility (ABIF), McGill University, Montreal, Quebec, Canada

[4]Cell Information Systems, McGill University, Montreal, Québec, Canada

[5]Department of Anatomy and Cell Biology, McGill University, Montreal, Québec, Canada

[*]**Corresponding author:** Anmar Khadra

McIntyre Medical Building (room 1120)

3655 Prom. Sir William Osler

Montreal, Quebec, Canada H3G 1Y6

Email: anmar.khadra@mcgill.ca

Telephone: (514) 398-1743

Abbreviated title: Mixed-mode oscillations in cell motility

Keywords: Rho family of GTPases, migration patterns, adhesion dynamics, cellular polarity, computational modeling, wave-pinning, mixed-mode oscillations, event detection, directionality ratio, α-value, instantaneous speed, membrane activity.

Funding: This work was supported by the Natural Sciences and Engineering Research Council of Canada discovery grant to AK and discovery grant to CMB, and the Fonds Nature et technologies team grant to AK and CMB. The funders had no role in study design, data collection or analysis, decision to publish or preparation of the manuscript.

Conflict of Interest: No conflict of interest.

Abstract

In mesenchymal cell motility, several migration patterns have been observed, including directional, exploratory and stationary. Two key members of the Rho-family of GTPases, Rac and Rho, along with an adaptor protein called paxillin, have been particularly implicated in the formation of such migration patterns and in regulating adhesion dynamics. Together, they form a key regulatory network that involves the mutual inhibition exerted by Rac and Rho on each other and the promotion of Rac activation by phosphorylated paxillin. Although this interaction is sufficient to generating wave-pinning that underscores cellular polarization comprised of cellular front (high active Rac) and back (high active Rho), it remains unclear how they interact collectively to induce other modes of migration detected in Chinese hamster Ovary (CHO-K1) cells. We previously developed a 6D reaction-diffusion model describing the interactions of these three proteins (in their active/phosphorylated and inactive/unphosphorylated forms) along with other auxiliary proteins, to decipher their role in generating wave-pinning. In this study, we explored, through computational modeling and image analysis, how differences in timescales within this molecular network can potentially produce the migration patterns in CHO-K1 cells and how switching between them could occur. To do so, the 6D model was reduced to an excitable 4D spatiotemporal model possessing three different timescales. The model produced not only wave-pinning in the presence of diffusion, but also mixed-mode oscillations (MMOs) and relaxation oscillations (ROs). Implementing the model using the Cellular Potts Model (CPM) produced outcomes in which protrusions in cell membrane changed Rac-Rho localization, resulting in membrane oscillations and fast directionality variations similar to those seen in CHO-K1 cells. The latter was assessed by comparing the migration patterns of CHO-K1 cells with CPM cells using four metrics: instantaneous cell speed, exponent of mean square-displacement (called α-value), directionality ratio and protrusion rate. Variations in migration patterns induced by mutating paxillin's serine 273 residue was also captured by the model and detected by a machine classifier, revealing that this mutation alters the dynamics of the system from MMOs to ROs or nonoscillatory behaviour through variation in the concentration of an active form of an adhesion protein called p21-Activated Kinase 1 (PAK). These results thus suggest that MMOs and adhesion dynamics are the key ingredients underlying CHO-K1 cell motility.

3.1 Introduction

Mesenchymal cell migration is a spatiotemporal phenomenon that refers to one mode of cell movement characterized by the development of protrusive areas at the cell front and retractive areas at the cell rear and the requirement of energy consumption [B1]. It is regulated by both extrinsic (e.g., chemokinetactic gradients) [B2,B3] and intrinsic signals (e.g., Rho family of GTPases) [B4, B5] that result in the spatial organization and subsequent dynamic remodelling of subcellular structures such as protein complexes termed adhesions that anchor a motile cell to its substrate and the actin-cytoskeleton [B6]. It is an essential process for many physiological functions, including embryonic development [B7], wound healing [B8], inflammation and axonal growth during development [B9]; it is also involved in pathophysiological conditions such as cancer metastasis [B8, B10] and thrombosis [B11]. Thus, a more clear understanding of the molecular processes that regulate cell migration will improve our understanding of a fundamental cellular physiology and also can lead to new discoveries for the treatment of disease.

Motile cells display a wide range of migratory behaviours [B1]. They can bias their direction of locomotion by heading to the source of a stimulus, or randomly explore their surrounding environment [B12]. Understanding the underlying mechanisms that lead to different patterns of cell migration (e.g. random, directed) is a challenging task given the large number of proteins involved. Indeed, over two hundred proteins have been implicated in regulating cell migration and adhesion dynamics with complex biological signaling pathways governing their interactions and activity [B13]. Nonetheless, two members of the Rho-family of GTPases Rac1 and RhoA (referred to as Rac and Rho for the remainder of this study) have been identified as key players responsible for generating cellular polarity, comprised of a cell front and rear, leading to directional cell migration [B14]. They transition from inactive (guanosine diphosphate (GDP)-bound) to active (guanosine triphosphate (GTP)-bound) forms, via Guanine nucleotide Exchange Factors (GEFs), and vice versa, via GTPase-Activating Proteins (GAPs) [B4]. Activation is also regulated through their mutual inhibition that the active forms of Rac and Rho exert on each other. Together these two processes of activation and deactivation form the key signaling pathways for producing cellular polarization [B4]. Active Rac is responsible for actin polymerization, causing membrane protrusion [B15–B18] and formation of lamellipodia (cytoskeletal projection of the membrane at the leading edge of the cell). Rho, on the other hand, is known to induce the formation of actin stress fibers and large stable focal adhesions [B4, B5, B19], and is responsible for the actomyosin-driven contractions at the rear of a cell required for membrane retraction towards the nucleus [B20].

It has been shown that the dynamics of Rac and Rho are modulated by an adaptor protein called paxillin [B21]. This adhesion protein can be phosphorylated at its serine 273 (S273) residue by the active form of the protein p21-Activated Kinase 1 (PAK) when bound to RacGTP (PAK-RacGTP) [B22]. This phosphorylated form of

paxillin can then bind to a protein complex formed by: the G protein-coupled receptor kinase InteracTor 1 (GIT), beta-PAK-Interacting exchange factor (PIX), and PAK, and subsequently promote further Rac activation [B22]. The phosphorylation of paxillin at S273 is one crucial switch for regulating fast adhesion assembly and disassembly [B21–B24]. Interestingly, substituting serine by alanine (S273A) or aspartic acid (S273D) generates, respectively, nonphosphorylatable and phosphomimetic mutants that directly affect not only the motility patterns of Chinese Hamster Ovary (CHO-K1) cells but also adhesion dynamics across the cell [B22, B24] and paxillin co-binding with PAK in adhesion subdomains [B24]. The nonphosphorylatable S273A mutant showed reduced motility, more stable adhesions and minimal co-binding with PAK compared to wildtype cells. In contrast, the phosphomimetic S273D paxillin mutant showed more enhanced motility, more dynamic adhesions and increased paxillin-PAK co-binding to adhesions [B24].

The complexity of this system and how it impacts cell migration motivates the use of mathematical modelling approaches to quantitatively study this system [B25]. Previous models have varied in complexity and analyzed different aspects of cell migration, but many of them focused on the Rac-Rho subsystem. In these models, the mutual inhibition seen in the Rac-Rho system was sufficient to generate the spatiotemporal pattern needed to generate cell polarity. This spatiotemporal pattern, called wave-pinning, is formed when a travelling wave in the cytosol is pinned in space, generating a concentration gradient in Rac and Rho and a polarized cell with a front and back, respectively [B26, B27]. The dynamics of this spatiotemporal phenomenon was expanded by including paxillin and the GIT-PIX-PAK complex in a six-dimensional (6D) mathematical model characterizing how paxillin can affect polarity and wave-pinning [B21,B23]. This work has highlighted the importance of paxillin in the small GTPases Rac and Rho activation.

Chinese hamster ovary (CHO-K1) cells have long been used to study cell motility. Despite their lack of significant polarity, CHO-K1 cells show significant protrusion and retraction leading to random migration as seen when they are placed on glass coverslips coated with extracellular matrix (ECM) proteins [B28]. Persistent polarity leading to rapid directed cell migration is rare but the cells do form dynamic and stable adhesion complexes whose assembly, disassembly and stability are tightly regulated by proteins including paxillin [B22]. Waves and oscillatory phenomena, in both cell tracks and membrane protrusions are frequently detected in various cell lines migrating on 2D surfaces [B29, B30], so this prompted the question of whether wave-pinning alone can produce such behaviours, and if not, what other oscillatory dynamics must be involved. Much experimental evidence has repeatedly demonstrated the importance of shape oscillations in cell migration [B31]. Several mathematical studies have attempted to understand how these oscillations are generated at the cell membrane level using a spatiotemporal model with multiple timescales [B32,B33]. Existing mathematical models involving the Rac-Rho system typically accounted for polarized cells with a leading front and a stable back [B26,B34,B35].

These models were then further expanded to couple the Rac-Rho system to the extracellular matrix (ECM), generating oscillatory dynamics that were either periodic or semi-periodic [B36]. The amplitude of the oscillations in these models did not change or changed very little (e.g. in the case of semi-periodic oscillations). Therefore, implementing these models using the Cellular Potts Model (CPM), a computational discrete grid-based simulation technique that involves the modelling of the ECM as a mesh upon which simulated cells are superimposed [B37], typically produced migrating cells that were either purely directional or do not migrate significantly but remain inactive with random cell membrane protrusion and retraction (depending on the amplitude of the oscillations), but not both. The fact that CHO-K1 cells do display both of these behaviours simultaneously, allowing them to explore and migrate [B24, B38], suggests that other oscillatory dynamics may be at play.

In this study, we used a reduced four-dimensional (4D) spatiotemporal model that possesses three different timescales [B39] to analyze motility patterns of CPM cells and how they compare to those exhibited by CHO-K1 cells. The model was both physiological, taking into account the dynamics of Rac and how it interacts with Rho and paxillin, as well as phenomenological to allow for the inclusion of two slower time scales. The model, in the absence of diffusion, produced temporal profiles that possessed both slow large amplitude oscillations and fast slow amplitude oscillations in the form of mixed-mode oscillations (MMOs) [B40]. Several metrics developed in this study demonstrated that such MMOs are essential for capturing the key features of CHO-K1 cell migration.

3.2 Results

3.2.1 CHO-K1 cells display two distinct migration patterns: active and inactive

To explore the role of paxillin phosphorylation on serine 273, we studied Chinese hamster ovary (CHO-K1) cells. When we visually examined the migration patterns of CHO-K1 cells, data showed that they can be either (i) inactive (Fig. 14a), remaining mostly stationary (i.e. stalled) while attached to the substrate with very little movement in their membrane and very limited displacement away from their starting point, or (ii) active (Fig. 14b), exhibiting more migration activity by moving around on the substrate and travelling away from their starting point. When inspecting all the recorded tracks of imaged CHO-K1 cells, we found that they all exhibited one of these migration patterns (Fig. 14c), generating two independent classes of inactive and active cells displaying low or high levels of membrane activity, respectively (Fig. 14d).

The exponent of mean square-displacement, called the α-value expressed in Equation 21 (see Methods), provides a metric to automate classification of CHO-K1 cells as inactive or active. Thus, to systematically distinguish between the two classes of CHO-K1 cells detected, we first used the α-value to split them into two separate classes. Those that attained α-values below 1.4 were considered inactive, while those that attained α-

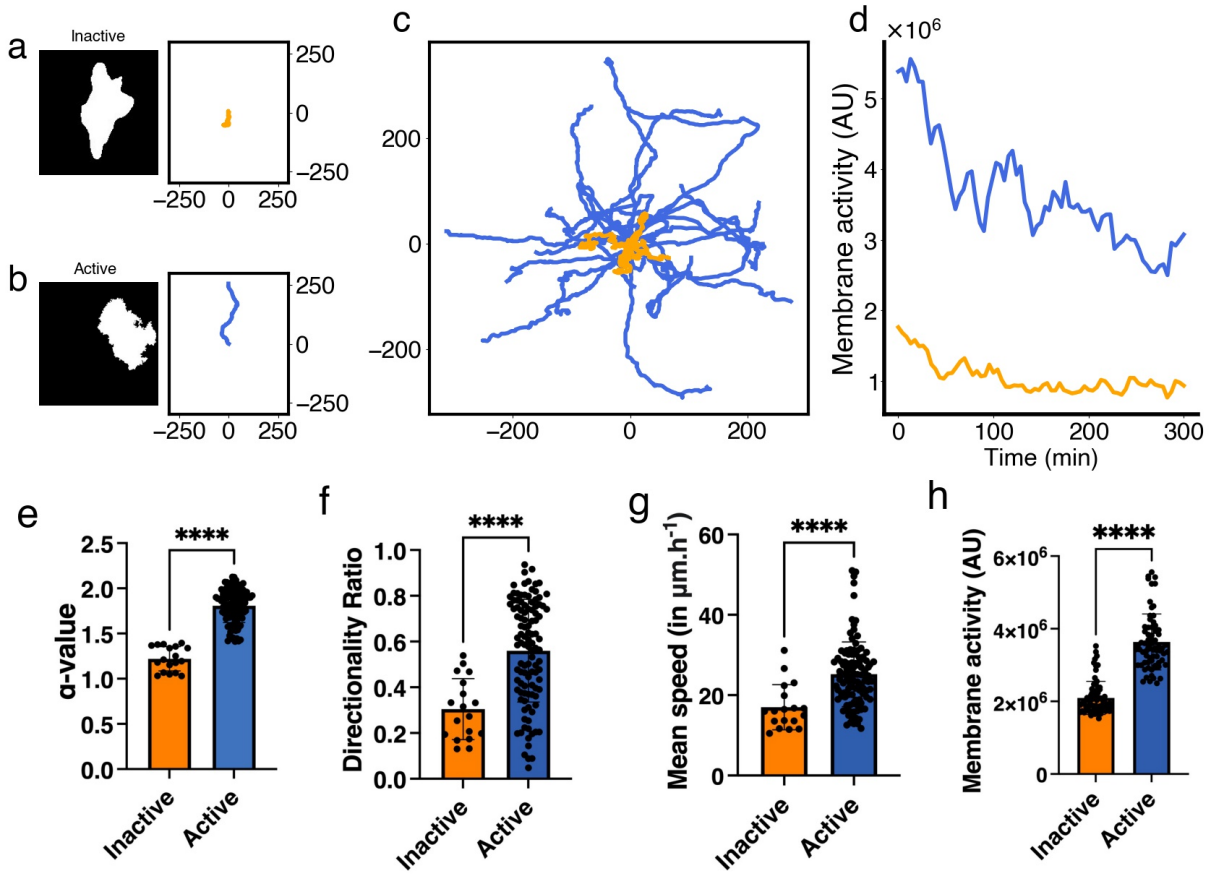

Figure 14: Characteristics of inactive and active classes of CHO-K1 cells exhibiting two distinct migration patterns detected using the α-value. (a, b) Representative binary masks (left) illustrating the shapes of CHO-K1 cells, along with their representative migration tracks (right). (c) Roseplots of a sample of CHO-K1 cell tracks (31 in total) colour-coded according to each class; orange: inactive, blue: active. (d) Time series of the level of membrane activity of two representative CHO-K1 cells, colour-coded according to each class. (e) Mean α-value of CHO-K1 cells in each class. (f) Directionality ratio (DR) for the entire trajectory of CHO-K1 cells in each class. (g) Mean instantaneous speed of CHO-K1 cells in each class. (h) Multiple measurements of the level of membrane activity, in term of pixel counts, of CHO-K1 cells in each class. Error bars indicate SEM. Black dots represent individual cells. Tracking data from Kiepas (2020) were used to produce panels c, e, f and g. Tracking data and cell images acquired for this study were used to produce panels a, b, d and h. There were n = 18 inactive cells and n = 108 active cells in panels e, f and g, whereas there were n=3 inactive and n=4 active cells in panel h.

values above 1.4 were considered active (Fig. 14e). Based on extensive exploration of the data, it was determined that a 1.4-threshold generated the best separation between these two classes. We then used three additional metrics, directionality ratio (DR), instantaneous speed and level of membrane activity to further characterize the behaviour of the two classes identified. Results revealed that the inactive class, on average, exhibited significantly lower DR values, instantaneous speed and membrane activity than active cells. Active cells displayed more wavy patterns on the membrane and oscillated in an irregular fashion (compare the blue trace that exhibits slow oscillations to the yellow trace that does not in Fig. 14d).

The differences between inactive and active cells identified here are consistent with what was previously found in the literature [B28]. Using the α-value, we were able to demonstrate here that these two classes of cells are indeed distinct in a systematic and automated fashion. This, however, raises the question of what the underlying causes of such differences are between the two dynamic classes of cells?

3.2.2 Mixed-mode oscillations in scaled Rac concentration

It has been previously shown that wave-pinning, a spatiotemporal phenomenon that describes the propagation of a front of higher protein concentration that eventually gets pinned in space, underlies cellular polarization in motile cells [B26]. It is an inherent property of some reaction-diffusion systems capable of attaining two different states for the same set of parameters but starting from different initial conditions (also called "bistability"). Such spatiotemporal phenomenon, however, typically produces migrating cells that are persistently directional, a feature that appears not to be very consistent with CHO-K1 cell migration patterns (Fig. 14), including local Rac activities in several locations in the cytosol and wavy patterns travelling across the membrane.

To explore if other dynamic behaviours, aside from bistability, can produce migration patterns that are in agreement with those seen in CHO-K1 cells, we designed a simplified mechanistic model involving active and inactive forms of Rac (Fig 15) that possesses multiple time scales ranging from fast to slow (see Methods) [B39]. In this model frame, described by the 4D model of Eqs. (20), active Rac exerts positive (negative) feedback on paxillin phosphorylation rate on a fast (slow) timescale (Fig. 15a), as well as exerts indirect positive auto-feedback (via Rho) on itself through RacGEF. The combination of the timescales in this model allows scaled concentration of Rac to display one type of oscillations that are called mixed-mode oscillations (MMOs) (Fig. 15b) [B39]. In MMOs, fast small amplitude oscillations are combined with slow large amplitude oscillations that can potentially allow for local Rac activities in several locations in the cytosol to form and wavy patterns travelling across the membrane to occur.

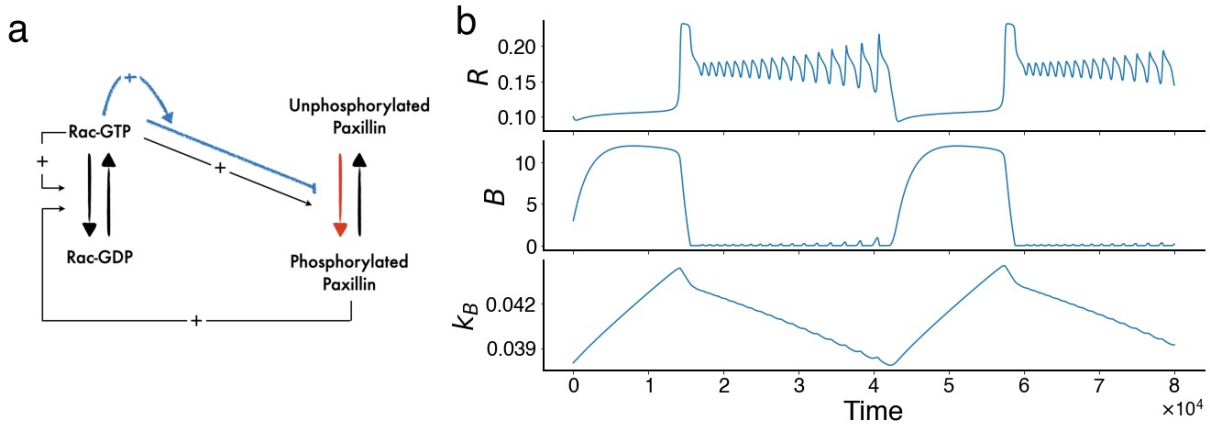

Figure 15: Model framework and model simulations. (a) Schematic of the semi-phenomenological four-dimensional (4D) model of Eqs. (20). Rac cycles between inactive (GDP-bound) and active (GTP-bound) forms. Rac-GTP (denoted by R) exerts an indirect positive auto-feedback (via Rho) on itself through RacGEF. It also simultaneously exerts positive and negative (blue pathway) feedback on paxillin phosphorylation at a fast and a slow timescale, respectively. Phosphorylated paxillin, in turn, indirectly upregulates Rac activation through RacGEF. Blue pathway: refinement of the original model Tang *et al* (2018) ; red pathway: the reaction directly influenced by the half-maximum phosphorylation of paxillin (L_K). (b) Time courses of active Rac (R), phosphorylation rate (B) and recovery rate (k_B) in the absence of diffusion, showing the presence of mixed-model oscillations (MMOs) in R.

3.2.3 Cellular Potts Model (CPM) simulated cells exhibit three distinct migration patterns: directed, oscillatory and inactive

Having detected two classes of CHO-K1 cells from experimental data, we went on to explore if Cellular Potts Model (CPM) simulated cells, governed by the 4D model of Eqs. (20), can also exhibit the two distinct migration patterns. Making this link would allow us to test the hypothesis of whether the dynamic feature of MMOs, that combine slow large amplitude with fast small amplitude oscillations, underlies active CHO-K1 cell migration.

To do this, we first simulated 60 CPM cells; this produced noisy tracks with considerable variability due to the stochastic nature of the CPM simulations. When visually examining these tracks, three distinct motility patterns were discernible, one of which was inactive (Fig. 16a), exhibiting migration patterns very similar to inactive CHO-K1 cells, while the other two were active (Fig. 16b, c). The active CPM cells were either highly directed (Fig. 16c) or exhibited migration pattern that were more like patterns seen with active CHO-K1 cells (Fig. 16b). The dynamics of this latter group is governed by MMOs (and hence labelled "oscillating" CPM cells hereafter), while directed cells are purely governed by wave-pinning [B26, B27]. All the simulated CPM cells appeared to fall into one of these three classes of migration patterns (Fig. 16d) and their levels of membrane activity seemed to positively correlate with their ability to migrate (Fig. 16e). Interestingly, CPM cells in the oscillating class were found to also exhibit slow oscillations in their membrane activity, unlike the other two

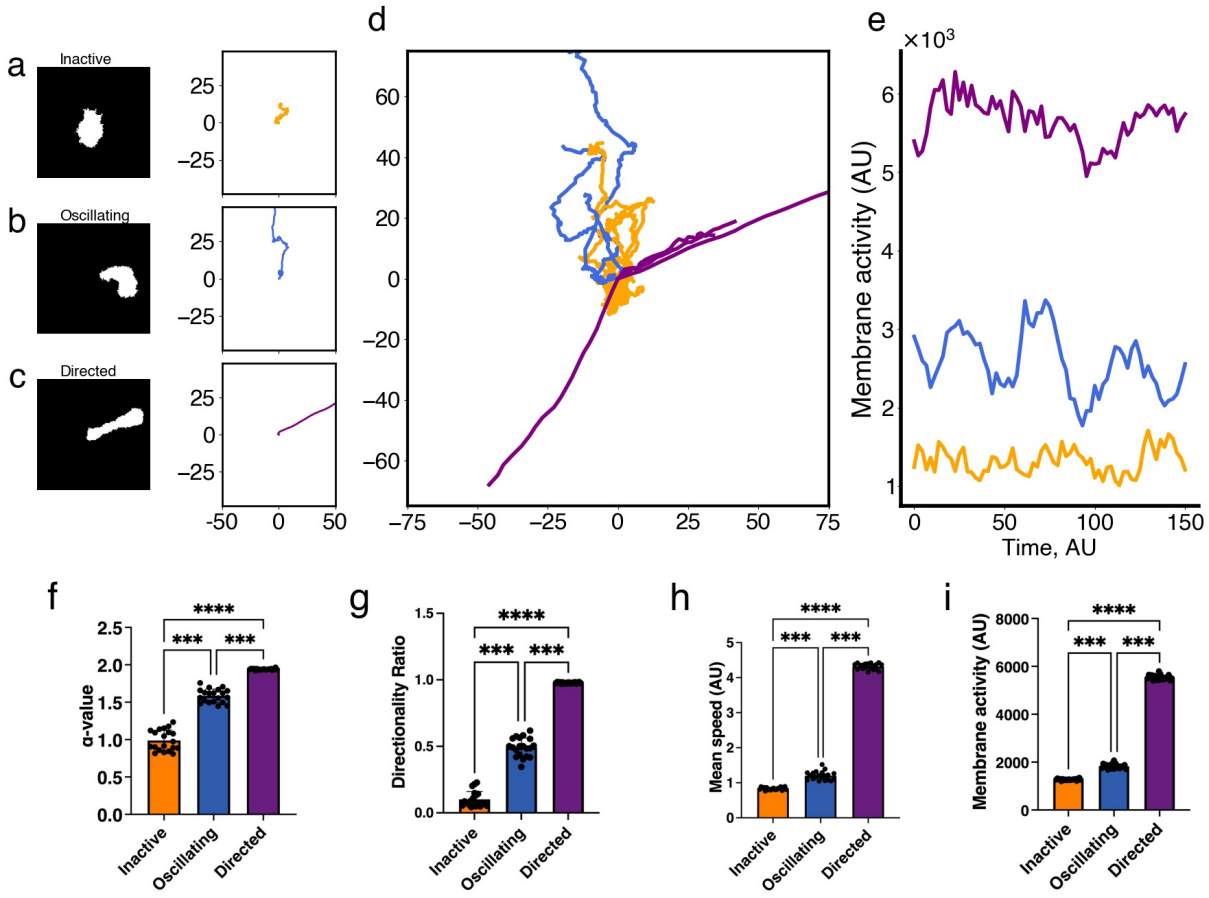

Figure 16: Characteristics of the three classes (n=20 for each group) of simulated cells obtained by the Cellular Potts Model (CPM) exhibiting distinct migration patterns detected by the two metrics: α-value, that distinguishes inactive from active CPM cells, and directionality ratio (DR), that divides active cells into oscillatory and directed cells. (a, b, c) Representative binary masks (left) illustrating the relevant shapes of CPM cells, along with their representative migration tracks (right). (d) Roseplots of a sample (n=21) of CPM cell tracks colour-coded according to each class; orange: inactive, blue: oscillatory, purple: directed. (e) Time series of the level of membrane activity of three representative CPM cells, colour-coded according to each class. (f) Mean α-value of CPM cells in each class. (g) Directionality ratio (DR) for the entire trajectory of CPM cells in each class. (h) Mean instantaneous speed of CPM cells in each class. Inactive cells have a non-zero mean instantaneous speed due to their inherent stochasticity, causing them to be random. (i) Mean level of membrane activity, in terms of pixel counts, of CPM cells in each class. Error bars indicate SEM. Black dots represent individual cells.

classes (Fig. 16e). Oscillating CPM cells on average show membrane activity that is 1.945 times higher than inactive CPM cells, a ratio that is similar to the 1.825 obtained for active versus inactive CHO-K1 cells.

To systematically categorize the classes of CPM cells, we applied the same strategy used on CHO-K1 cells by using the 1.4-threshold in α-value to separate inactive CPM cells from active ones. The active CPM cells were then further divided into oscillating and directed by choosing a threshold of 0.8 in DR. This combined strategy generated a clear distinction between the three classes of CPM cells based on their α-value (Fig. 16f) and DR (Fig. 16g). Interestingly, the α-value of directed CPM cells was ≈ 2, indicating a super-diffusive motion, while the DR value of inactive cells was very low, highlighting a motion that is random (i.e. the inactive CPM cells were mostly stationary). Comparing the mean instantaneous speed (Fig. 16h) and mean level of membrane activity (Fig. 16i) between the three classes of CPM cells revealed that these two metrics positively correlated with the efficiency with which each class migrate. In other words, inactive (directed) CPM cells had the lowest (highest) mean instantaneous speed and level of membrane activity compared to other classes, an expected outcome in view of how these classes of CPM cells were defined.

3.2.4 Active Rac localization is central in defining the three classes of CPM cells

To determine what role the spatiotemporal dynamics of Rac plays in generating differences between the three classes of CPM cells, Rac activity was studied across the entire cell bodies of these simulated cells. To do this, we first considered the inactive class of CPM cells. In this class, CPM cells always displayed homogeneous scaled concentrations of active and inactive Rac along their membrane (Fig. S1a) and in their cytoplasm, respectively, but still attained a non-zero mean instantaneous speed (Fig. 16h). The reason for the latter is because the CPM relies on a Hamiltonian to estimate different energy configurations and tends to minimize it locally. Because the minimization includes a stochastic component, the CPM makes it possible for these inactive cells to have slight changes in membrane configurations over time, granting them the ability to move around during these energy fluctuations. Such behaviour can be seen as a random motion, with DR that drops very quickly over time to approach zero.

In the second class, oscillating CPM cells were found to exhibit episodic bursts of activity and waving patterns in their membrane (Fig. 16e). The bursts of activity were manifested as increased levels of protrusions, due to active Rac localization along the membrane (Fig. S1b), that do not last for too long but are repeated periodically. Such behaviour caused the CPM cells to sometimes stretch (because of multiples protruding fronts that dynamically change localization), and to not exhibit straight migratory pattern (because of their episodic activity in protrusions and retractions) (Fig. 17a). As a result, they exhibited meandering migratory paths (Fig. 16b) with active protrusions that allowed them to migrate a lot further than inactive CPM cells (Figs. 16f and 17a, b; red

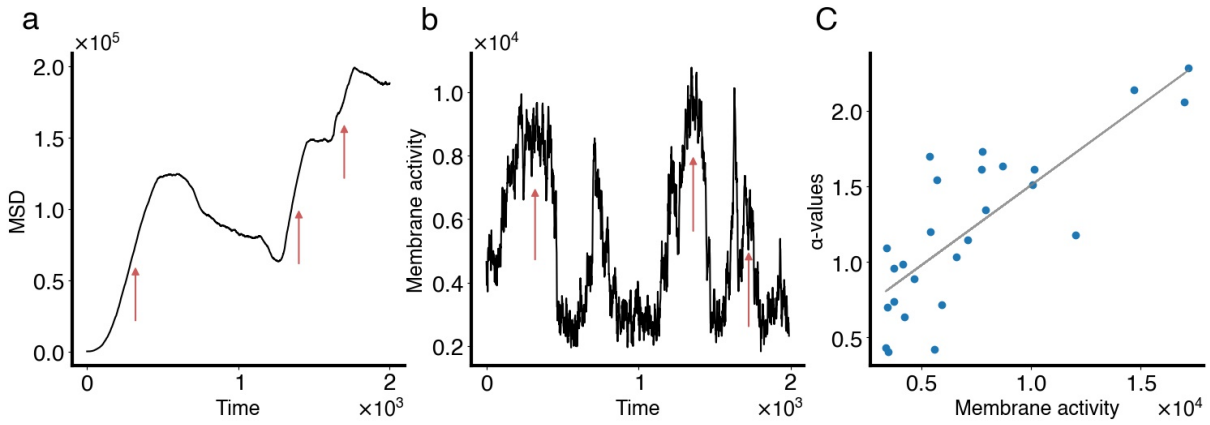

Figure 17: Characterizing cell movement of oscillating CPM cells. (a) MSD time series of an oscillating CPM cell. Red arrows point to periods of directed motion, when the MSD scales with t^2. (b) Level of membrane activity associated with the same cell in a. Notice how periods of directed motion in the MSD correspond to periods of increased level of membrane activity, called bursts of activity (also highlighted by red arrows in this panel). (c) α-values plotted against mean level of membrane activity (averaged over 40 time-steps) for this oscillating cell, along with the linear regression line (light gray).

arrows). The DR of their entire paths were low, but non-zero and not as low as the inactive ones (Figs. 16g). Their level of membrane activity varied depending on the phase of bursting (Fig. 17b), was positively correlated with the α-value (Fig. 17c) and picked up after increases in the speed of the cell; this level of membrane activity changed over time within the same track and caused the α-value to change meanwhile.

Finally, directed CPM cells were found to be very polarized with active Rac accumulating in the front but not in the rear (Fig. S1c). This extensively-studied feature of cell migration, called wave-pining [B26, B27], was reproducible by the model and caused the CPM cells to move in a fast and directed fashion for prolonged periods of time. Their DR values were close to 1 (Fig. 16g) and level of membrane activity were high throughout the whole simulations (Fig. 16e, i). Furthermore, their MSD indicated a superdiffusive active motion, with α-values close to 2.

3.2.5 Event detection in oscillating CPM cells is consistent with active CHO-K1 cells

To provide further evidence that oscillating CPM cells are representative of active CHO-K1 cells, we applied an event detection framework, designed to detect events of directionality change, on both CHO-K1 experimental and CPM simulated cells to further explore how they compare to each other.

For CHO-K1 cells, we previously distinguished active cells from those that were inactive (Fig. 14), classifying 108 tracks as belonging to the first class - active - and 18 belonging to the second - inactive. The event detection was run on the 108 active cell tracks. To ensure, retrospectively, that the detected events were indeed separating periods of directed motion, the α-value of each period of directedness was computed, averaged and eventually

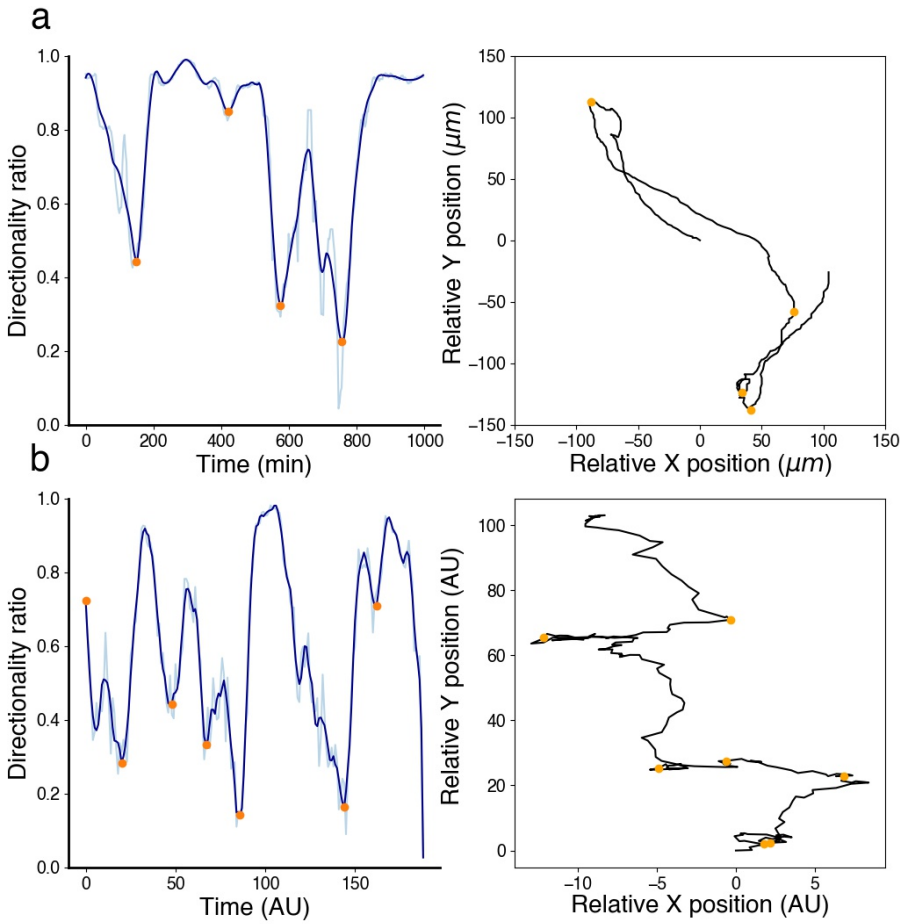

Figure 18: Periods of directedness and directionality change in active CHO-K1 and oscillating CPM cells. Event detection framework applied to (a) an active CHO-K1 cell, and (b) an oscillating CPM cell. Directionality ratio (left panels), computed using a rolling window of length 60 minutes (light blue) for an active CHO-K1 cell and 20 time-steps for an oscillating CPM cells, allowed for event detection (orange dots). Superimposing detected events (orange dots) on cell tracks (right panel) shows a good agreement with directionality change.

compared to the 1.4 threshold; our results indicated that, on average, the α-value for all periods of directedness and tracks was 2.065 ± 0.473, which is larger than the 1.4 threshold, indicating a very highly directed super-diffusive motion. As an example, for a randomly selected active CHO-K1 cell (Fig. 18a), the computed α-values of all detected periods of directedness were 2.069, 2.262, 2.143, 2.039 and 1.350, showing that during four out of five periods, the cell was directed. More importantly, when the α-values were computed using a 60-minute-long rolling window (see Methods), we found that, for each CHO-K1 cell track, the α-value of each period of directedness, delimited by two events, was almost always higher than its mean using the rolling window. Thus, this method allowed for the automatic identification of periods of increased directionality.

The same event detection framework was then applied on 20 oscillating CPM cell tracks. Interestingly, similar dynamics concerning change of direction were observed. As in CHO-K1 cells, periods of directness were followed

by clear changes in directionality. An example of such behaviour, a randomly selected oscillating CPM cell (Fig. 18b) showed that the computed α-values of all detected periods of directedness were 1.634, 1.56, 1.148, 2.645, 0.327, 1.724. When computing the average α-value of all periods of directedness and all tracks, a value of 1.851 ± 0.80 was obtained; this value is close to that seen in CHO-K1 cells (refer to figure).

3.2.6 Mutation of Serine-273 residue on paxillin alters CHO-K1 cell migration patterns

The S273 residue can be targeted to generate phosphomimetic or nonphosphorylatable mutants of paxillin in which the serine 273 residue is replaced with aspartic acid (S273D) or alanine (S273A), respectively. Here, we investigated how such mutations alter migration patterns.

Cells expressing the paxillin-EGFP-S273A mutant showed impaired motility with typically shorter migration tracks compared to CHO-K1 cells expressing wild-type paxillin-EGFP (Fig. 19; compare panel a to b). Indeed, cells expressing the S273A mutant had significantly reduced instantaneous speed of 16.1 ± 0.658 μm·h^{-1} and lower mean α-value of 1.418 ± 0.038 compared to CHO-K1 cells expressing wild-type-paxillin-EGFP whose mean instantaneous speed was 25.8 ± 0.822 μm·h^{-1} and mean α-value was 1.698 ± 0.037 (Fig. 19d and e, respectively). Cells expressing the paxillin-EGFP-S273D phosphomimic, on the other hand, displayed - on average - a more active migratory phenotype than cells expressing wild-type-paxillin-EGFP (Fig. 19; compare panel a to c) with a higher mean instantaneous speed of 35.2 ± 1.93 μm·h^{-1} (Fig. 19d) and elevated, but statistically insignificant, mean α-value of 1.672 ± 0.028 (Fig. 19e). These results are in agreement with previously published data [B22,B24].

To further explore how the migration patterns of cells expressing wild-type versus mutant paxillin compare to each other, the number of events representing changes in directionality (as defined by Fig. 18) were measured for all cells in each condition. The results were normalized by the number of events in cells expressing wild-type-paxillin-EGFP (Fig. 19f). Our results showed that cells expressing the S273A mutant exhibited a significantly lower number of events (1.93) than wild-type expressing cells (2.55) and S273D mutant expressing cells (2.62), but the latter two groups did not show statistically significant differences.

These results thus suggest that cells expressing the S273A mutant are distinct in their migration patterns, exhibiting a far less active migratory behaviour, while the migration patterns of cells expressing the S273D phosphomimic are generally equivalent to or are slightly more dynamic than cells expressing wild-type paxillin.

3.2.7 Mutant CPM cells can mimic cells expressing paxillin phosphorylation mutants by altering the model to change the sensitivity of paxillin to phosphorylation

The total active PAK concentration (i.e., total RacGTP-bound PAK) is known to be essential for paxillin phosphorylation at the S273 residue. The half-maximal activation parameter L_K in Eq. (19) describes phenomenologically

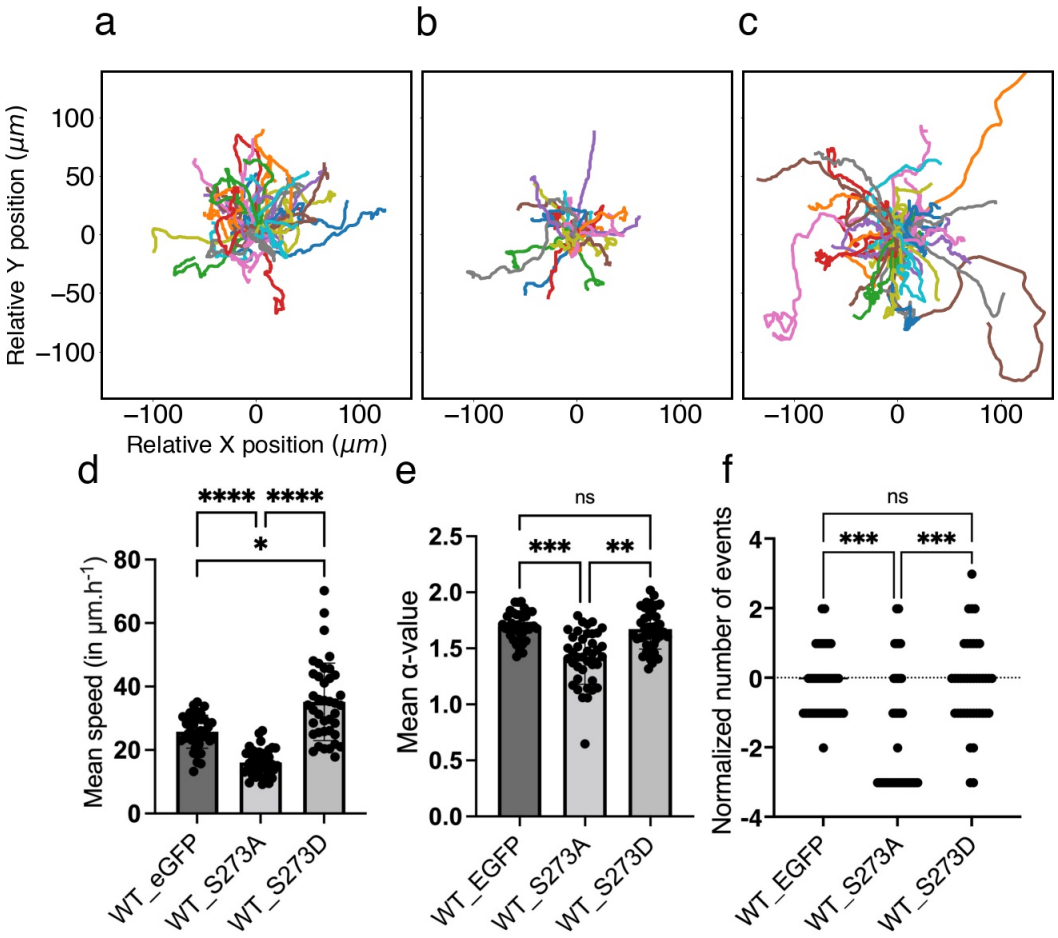

Figure 19: Serine-273 (S273) residue on paxillin is key to CHO-K1 cell migration. Roseplots showing cell tracks (n=40 cells for each condition) of wild-type CHO-K1 cells that were transfected with (a) paxillin-EGFP, (b) paxillin-S273A-EGFP phosphomutant, and (c) paxillin-S273D-EGFP phosphomimic. (d) Mean instantaneous speed of the same sampled cells in each condition, measured over 360 minute-long recordings. (e) Mean α-value of the same sampled cells in each condition, computed using a rolling window of length 60 minutes. (f) Normalized number of events of the same sampled cells in each condition computed over their entire tracks. Error bars indicate SEM. Cell tracking data from Rajah (2019) were used to produce the figure.

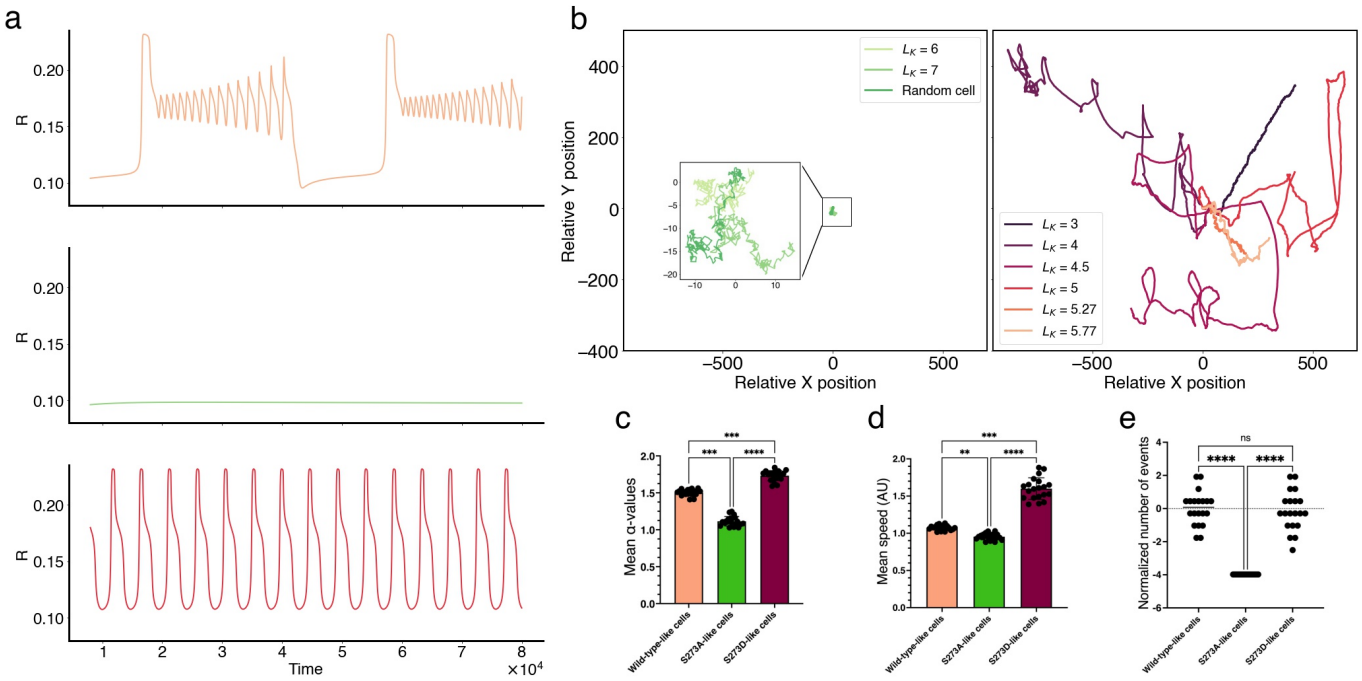

Figure 20: Role of PAK-dependent sensitivity parameter L_K in defining mutant dynamics in CPM cells. (a) Time series simulations of active Rac at default value of $L_K = 5.77$ (top) showing mixed-mode oscillations (MMOs), at $L_K = 7$ (middle) showing non-oscillatory behaviour, and at $L_K = 4.5$ (bottom) showing relaxation oscillations (ROs). (b) Migration tracks of CPM cells generated by altering only L_K while keeping other parameters fixed; this produced inactive (i.e., random) cells when $L_K > 6$ (left), or actively migrating cells when $L_K \lesssim 6$ (right). The lower the value of L_K, the further the CPM cell typically migrated. (c) Mean instantaneous speed, (d) mean α-values, and (e) normalized number of events evaluated over the entire simulated track from 20 cells from each of wild-type-like ($L_K = 5.77$), S273A-like ($L_K = 7$) and S273D-like ($L_K = 4.5$) CPM cells. The number of events in the S273A-like CPM cells did not vary because they all exhibited random inactive migration pattern; they were all zero and became negative when normalized. Error bars indicate SEM.

how sensitive paxillin phosphorylation is to active PAK (PAK-RacGTP) concentration. Thus, L_K is a parameter that indirectly links adhesion dynamics to cell motility and causes significant changes to Rac dynamics when it is altered. For example, increasing L_K above ~ 6 caused Rac dynamics to change from MMOs to being non-oscillatory, whereas decreasing it below ~ 5.25 caused active Rac dynamics to change from MMOs to relaxation oscillations (ROs) (Fig. 20a). To investigate how altering the value of this parameter affects migration patterns of CPM cells, we simulated CPM cells at different values of L_K and plotted their migration tacks (Fig. 20a). Doing so revealed that setting $L_K \lesssim 6$ produced actively migrating cells, while setting $L_K \lesssim 6$ produced inactive or stationary cells (Fig. 20a), demonstrating its importance in defining CPM motility.

As a result, the parameter L_K was targeted to determine if this could generate similar migration patterns as cells expressing one of the two paxillin mutants. This was done by simulating 20 CPM cells per condition using Morpheus. In these simulations, all cells possessed identical parameter values across the three conditions except for L_K that was either kept at its default value of $L_K = 5.77$ to represent the wild-type paxillin expressing cells,

set to $L_K = 7$ to represent the S273A phosphomutant, or set to $L_K = 4.5$ to represent the S273D phosphomimic. In the S273A-like CPM cells, the mean instantaneous speed 0.9537 ± 0.009 and alpha value 1.115 ± 0.014 were significantly lower than those for wild-type-like CPM cells (mean instantaneous speed: 1.057 ± 0.007; mean α-value: 1.553 ± 0.010) (Fig. 20c and d, respectively). The normalized number of events representing changes in directionality in S273A-like CPM cells (-3.981; negative values due to normalization) was also significantly lower than the value for wild-type-like CPM cells which was 0, due to normalization (Fig. 20e).

In the case of S273D-like CPM cells, however, the instantaneous speed (1.60 ± 0.032) and α-values (1.690 ± 0.0170) of these simulations were significantly higher than wild-type-like CPM cells (Fig. 20c and d, respectively). The former is in agreement with how experimental cells expressing the S273D mutant compare to cells expressing wild-type paxillin, but the latter is not. This seems to suggest that distinguishing between the three cell conditions using the parameter L_K would be better captured by using distributions of L_K values (centred around those used for each condition) to describe them, rather than using one specific value of L_K to describe all CPM cells within each condition. This is in line with cell-to-cell variation expected in experimental systems. To further validate this argument, the normalized number of events representing change in directionality was calculated (-0.1475 relative to 0 for the wild-type-like cells) and was not statistically different from wild-type-like CPM cells (Fig. 20e), in agreement with what was seen in experiments with CHO-K1 cells (Fig. 19f). This suggests that the number of events in both wild-type-like and S273D-like cells are equivalent.

3.2.8 Machine classification-based approach to validate the CPM model

Now that the CPM model captured the key features of CHO-K1 migration, the question was: could a machine classifier be trained on simulated CPM cells belonging to the three simulated conditions, then recognize and distinguish between cells expressing wild-type-paxillin, or one of the two phosphorylation mutants S273A and S273D? In other words, can a classifier be trained with the dynamic features of simulated motile CPM cells to characterize experimental CHO-K1 cells?

An artificial neural network with 3 fully-connected layers that incorporated a set of 4 metrics: mean instantaneous speed of the cell, mean alpha-value, directionality ratio and number of events representing change in directionality was generated (see Methods). The neural network, or classifier, was trained using 10 of each wild-type-like ($L_K = 5.77$), S273A-like ($L_K = 7$) and S273D-like ($L_K = 4.5$) CPM cells. Its performance was then tested on sixty (twenty of each type) randomly simulated CPM cells. The classifier demonstrated almost-perfect accuracy.

The trained classifier was then applied to track 40 CHO-K1 cells expressing wild-type-paxillin-EGFP, paxillin-S273A-EGFP mutant or paxillin-S273D-EGFP mutant (Fig. 21). In each category, the classifier identified the

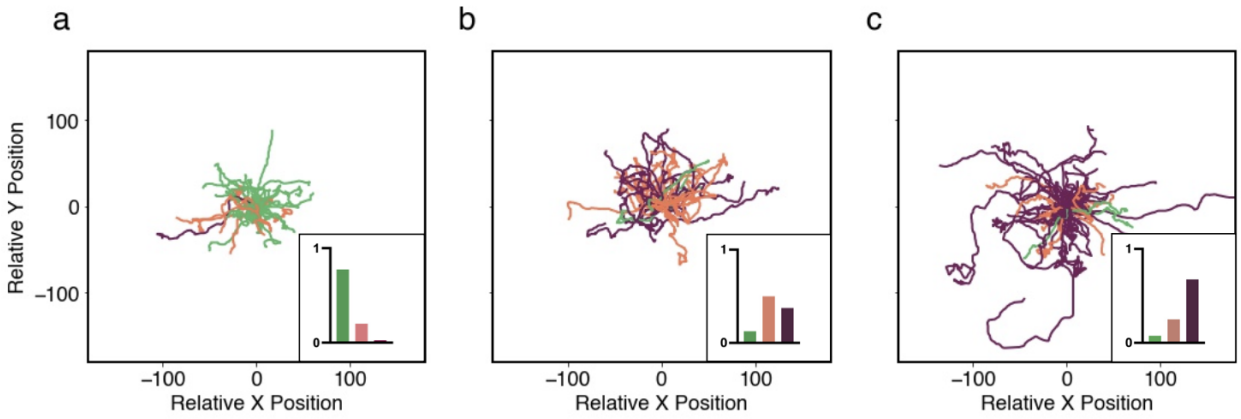

Figure 21: Machine classification of CHO-K1 cell tracks in three different condition. Tracks of 40 CHO-K1 cells expressing (a) paxillin-S273A-EGFP mutant, (b) wild-type-paxillin-EGFP, or (c) paxillin-S273D-EGFP mutant. Trajectories were colour-coded based on the classifier's predictions with green corresponding to tracks classified as cells expressing the S273A mutant, orange as wild-type and purple as the S273D mutant. Insets: boxplots showing the distributions of the classifier's predictions within each class. Tracking data from Rajah (2019) were used to produce the figure.

majority of wild-type or mutant expressing cells accurately by labelling them according to the type of paxillin they were expressing. The distribution of cell identification for each predicted condition was centred around the matching condition (Fig. 21, insets). Interestingly, a distribution shift was observed between cells expressing the S273A versus the S273D paxillin mutants. Specifically, the classifier identified most paxillin-S273D expressing cells correctly, with few recognized as wild-type-paxillin-EGFP expressing cells and very few as paxillin-S273A mutant expressing cells; the classifier did as well on the cells expressing the paxillin-S272A mutant: only one was identified as paxillin-S273D cells.

These results thus show that the classifier is able to identify the three groups of CHO-K1 cells after training only with simulated CPM cells. This supports our hypothesis that MMOs underlying the dynamics of wild-type-paxillin-like CPM cells is key to producing expected migration patterns of CHO-K1 cells.

3.3 Discussion

The present study brought new light onto what defines cell migration in CHO-K1 cells by emphasizing the importance of the presence of multiple timescales in governing the dynamics of Rac, Rho and paxillin. The pre-existing 6D spatiotemporal Rac, Rho and paxillin model [B21, B23] was simplified and modified to develop a reduced 4D spatiotemporal model to achieve this goal [B39]. The model described closely the dynamics of active and inactive Rac, based on its interaction with other proteins including Rho and paxillin, but also included a

phenomenological part comprised of two parameters that were turned into variables. These variables were the maximum phosphorylation rate of paxillin B and the recovery rate of B to its resting state B_r, given by k_B. The model incorporated, respectively, a fast and a slow positive and negative feedback from active Rac to paxillin phosphorylation (Fig. 15a).

The presence of the three timescales in the 4D model produced, in the absence of diffusion, a special kind of dynamic behaviour in the scaled concentration of Rac, namely, MMOs. MMOs combine slow large amplitude oscillations with fast small amplitude oscillations to generate interesting behaviours that we showed here to be key to CHO-K1 cell migration. By perturbing one key parameter of the 4D model, L_K, representing how sensitive paxillin phosphorylation is to active PAK (PAK-RacGTP) concentration, it was demonstrated that the model can also produce ROs and non-oscillatory behaviour.

Having previously analyzed mathematically how MMOs are generated by the 4D model using slow-fast analysis [B39], here an implementation of a Cellular Potts Model (CPM) was used to produce computer simulated cells. The spatiotemporal dynamics of these CPM cells exhibited three migratory patterns that were heavily influenced by not only the mutual inhibition of Rac and Rho, but also by the combination of slow large amplitude and fast small amplitude oscillations within MMOs. This temporal pattern resulted in CPM cells that fell into three classes with distinct modes of migration: directed with rare events of change in directionality, oscillatory with frequent directionality changes, and inactive in which CPM cells were mostly stationary.

Unlike the inactive and directed CPM cells, oscillatory CPM cells displayed meandering migration track caused by periodic bursts of activity with piece-wise directed motion interrupted by changes in directionality. The combination of slow large amplitude and fast small amplitude oscillations in MMOs were responsible for generating this behaviour. Stationary cells, on the other hand, displayed homogeneous scaled concentrations of active and inactive Rac in their cytoplasm, but still attained a non-zero mean instantaneous speed due to energy fluctuations in the Hamiltonian as seen in random motion. Finally, the motion of directed CPM cells was governed by mostly prolonged large amplitude oscillations (with minimal impact from fast small amplitude oscillations). Such migration pattern is similar to those produced by CPM cells whose underlying dynamics are governed by wave-pinning only [B27] or by standard oscillatory behaviour [B35, B41]. In other words, MMOs allow cells to simultaneously exhibit migratory and exploratory behaviours that standard non-MMOs or wave-pinning alone cannot, and localized active Rac activity is essential for generating the three migration patterns.

The migratory patterns of the CPM cells were then compared with the two CHO-K1 cell migration patterns detected in this study, namely, the active and inactive modes. Using a set of four metrics, including mean instantaneous speed, mean α-value, directionality ratio and level of membrane activity, we then characterized these two modes of migration and compared them to the ones generated by CPM cells. Our investigation revealed

that the oscillatory and inactive CPM cells were consistent with the migratory patterns of active and inactive CHO-K1 cells, respectively, while directed CPM cells were not consistent with any of the migratory patterns of CHO-K1 cells. The former highlighted the importance of MMOs in CHO-K1 cell motility and suggested that wave-pinning and standard oscillations are insufficient to produce the combination of directionality change and stationarity seen in CHO-K1 cells. In addition, the results of the event detection method highlighted how similar active CHO-K1 and oscillating CPM cells are in their migration patterns, with both cells types possessing periods of directedness separated by events of change in direction. They also produced similar averaged α-values during periods of directedness over all tracks. This showcases that the CPM offers a good model to study and understand how CHO-K1 cell migration is regulated. CHO-K1 cells do not contain many ion channels and thus tend not to be highly polarized and do not exhibit highly directed cell tracks. Therefore, it is not surprising that the directed cell population is not observed [B42].

By altering the sensitivity of paxillin phosphorylation to active PAK concentration (i.e., by perturbing the parameter L_K), CPM cells successfully reproduced the motility patterns of CHO-K1 cells expressing one of the two paxillin-mutants: S273A and S273D. To capture the former (latter), migratory behaviour of the CPM cells were impaired (enhanced) by increasing (decreasing) L_K. A comparison between mutant CPM and experimental CHO-K1 cells was then performed using a machine classifier trained using the simulated wild-type and mutant CPM cells. The classifier was successful in identifying CHO-K1 cells in each condition with high accuracy. This further highlighted that the CPM model governed by MMOs is sufficient to capture CHO-K1 cell migration and that perturbing adhesion dynamics reflected by the parameter L_K in the CPM model changes its underlying dynamics to either ROs or nonoscillatory behaviour. These latter temporal patterns are needed to capture the mutant dynamics associated with S273 amino acid phosphorylation. The classifier results also suggested that the limited number of CHO-K1 cells that were labelled differently than their actual condition may have some underlying differences in their protein network that make them different. This is not unexpected since each CHO-K1 cell expresses a different amount of the mutant paxillin protein and the cells also express endogenous paxillin that can compensate for the mutant proteins. In fact, the paxillin-S273A mutant is known to have a higher binding affinity for adhesions [B24]. With this longer binding time, it is less likely to be displaced by endogenous paxillin, making the phosphomutant the dominant form of paxillin in adhesions. Thus the classifier almost perfectly identified cells expressing S273A correctly. However, the paxillin-S273D mutant has a lower binding affinity to adhesions than even the wild-type protein [B24], so it can easily be displaced by endogenous paxillin. Endogenous paxillin can take on the form of the S273A or S273D mutant depending on its phosphorylation state leading to some cells being correctly identified as wild-type or S273A even though the cells are expressing the S273D phosphomimic.

The motility of S273D-like CPM cells was purely governed by ROs, allowing these cells to exhibit longer periods of directionality and to reach higher speeds. S273D-like CPM cells were very efficient in quickly changing their directionality due to the absence of small amplitude oscillations in ROs seen in MMOs. Taking a closer look at wild-type-like CPM cells, it was observed that they typically exhibited some brief random (diffusive) motions prior to directionality change, unlike S273D-like CPM cells. This random motion during change in directionality caused the discrepancy in the α-values that was not seen in CHO-K1 cells.

Small oscillations were visible in the time courses of the level of membrane activity in the active side of simulated CPM cells (results not shown). Limitations in the duration of imaging of CHO-K1 cells (mostly linked to the frequency at which these cells divide), however, did not allow to validate these observations on these cells. Some time courses of the level of membrane activity obtained from CHO-K1 cells showed irregular oscillations, but power spectra of these time series did not reveal anything (results not shown), because time series were too short to obtain clean power spectra. To further examine this aspect of CHO-K1 cell motility, higher time resolution imaging techniques are needed to investigate the dynamic of their protrusive activity.

Although CPMs are widely used to provide key insights into the mechanisms regulating cell motility, the nature of noise used in the simulation (white noise) can be substituted by other types of noise for purposes of enhancing the similarity with experimental biological systems. White noise does not allow for rare events or large deviations from the baseline in terms of cell perimeter or area and as a consequence, might not be closely aligned with the biological reality of cell motility. Coloured noise seems to provide a good alternative in some biological system simulations [B43, B44] and its impacts could be extensively studied in the future.

The stochastic nature of the simulations can also be envisioned differently. Simulated CPM cells were very distinct across the three conditions of wild-type versus mutant paxillin and showed significant differences in all metrics, whereas CHO-K1 cells expressing wild-type paxillin and S273 mutants did not show a statistical difference in DR measurement (results not shown). This may be due to the absence of ion channels, the variability in the expression level of wild-type or mutant paxillin, the presence of endogenous paxillin or upregulation of other motility-related proteins. The classification task may be able to identify this variability and correctly identify the CHO-K1 cell behaviours. Future plans are to improve the simulation set-up by sampling the parameter L_K from a distribution instead of assigning each condition a single value. This would nevertheless require an estimate of the distribution of L_K that the parameters should be sampled from, but would produce more diverse phenotypes within a given condition.

This study involved the development of tools that can continue to be developed for simulating cell migration and varying regulation of migration through paxillin phosphorylation. The simulations accurately reproduced the known experimental outcomes. Tools were also developed for automated 1) cell segmentation 2) cell track

generation, 3) identification of cell direction changes, 4) measurements of cell speed, 5) determination of type of cell movement (e.g. inactive, random, directed), 6) calculation of directionality ratios, 7) calculation of cell speed, 8) calculation of cell membrane activity and 9) classification of cell tracks.

This study demonstrates the utility of a newly developed CPM for simulated cell migration movies, provides a MMO model that can generate physiologically relevant cell migration tracks, and applies this model to further understand cell migration of CHO-K1 cells and the role of paxillin S273 phosphorylation in regulating that migration by characterizing the underlying dynamics. It uses both computational methods and mathematical modelling to achieve this goal. The approaches applied can be further expanded to analyze motility patterns in other cell types in different conditions and to include other phosphorylation pathways that regulate cell migration through the regulation of adhesions, the actin-cytoskeleton and Rho-GTPases.

3.4 Methods

3.4.1 CHO-K1 cell growth and imaging

Wild-type Chinese Hamster Ovary-K1 (CHO-K1) cells were obtained from the American Type Culture Collection (Cat. no.: CCL-61, ATCC). CHO-K1 cells stably expressing WT-paxillin–EGFP were obtained from the lab of Dr Rick Horowitz (University of Virginia, Charlottesville, VA). Stable cell lines expressing paxillin-S273A-EGFP or paxillin-S273D-EGFP were based on ATCC purchased CHO-K1 cells. CHO-K1 cells stably expressing G. gallus (chicken) paxillin-EGFP were seeded onto fibronectin coated ibidi 8-well u-slide (Ibidi, Cat. no. 80826) at a density of 2000 cells/cm^2 and allowed to attach overnight. Before plating cells, the dishes were coated with a freshly made 2 ug/mL solution of fibronectin diluted in phosphate buffered saline (PBS) from a stock of 0.1% human plasma fibronectin (Sigma Aldrich, Cat. no. F-0895). The fibronectin coating was applied overnight at 4^oC. Dishes were then washed 3x with Phosphate Buffered Saline (PBS). The CHO-K1 cells were grown in low glucose (1.0 g/L) Dulbecco's modified Eagle's medium (DMEM; Thermo Fisher Scientific, Cat. no. 11,885-084) supplemented with 10% fetal bovine serum (FBS; Thermo Fisher Scientific, Cat. no. 10082-147,), 1% non-essential amino acids (Thermo Fisher Scientific, Cat. no. 11140-050,), 25 mM 4-(2-hydroxyethyl)-1-piperazineethanesulfonic acid (HEPES; Thermo Fisher Scientific, Cat. no. 15630-080,) and 1% penicillin-streptomycin (Thermo Fisher Scientific, Cat. no. 10378-016,). Cells were maintained in 0.5 mg/mL Geneticin-418 (G418; Thermo Fisher Scientific, Cat. no. 11811-031,) antibiotic selection to maintain paxillin–EGFP expression. After ensuring the cells were attached to the well surface, the samples were placed in a Chamlide TC-L-Z003 stage top environmental control incubator (Live Cell Instrument, Seoul, South Korea) to maintain the cells at 37^oC and 5% CO_2 while imaging. The cells were imaged with transmitted light and fluorescence emission

of EGFP on an automated Zeiss AxioObserver microscope with a Plan-ApoChromat 20X/0.8 NA objective lens and an Axiocam 506 monochrome CCD camera (Carl Zeiss, Jena, Germany, 2752 x 2208 pixels, 4.54 μm pixels). Transmitted light images were acquired with the halide lamp set at 3V of power and a 50 ms camera exposure time. Fluorescence images were collected using the X-Cite 120 LED light source (Excelitas, Toronto, Ontario, Canada) and a FS10 filter cube (Carl Zeiss, Jena, Germany, Ex450-490 nm, Dichroic Filter FT510, Em515-565 nm). The light power on the sample was set to 1% excitation light intensity using 10% lamp power and a 10% neutral density filter. Fluorescence images were collected with a 5 s exposure time. For protrusion measurements, images were collected at 3-minute intervals for a total of 5 hours. The resulting image timeseries were saved as a Zeiss propriety "czi" files that was later used to track the cells using a FIJI/ImageJ Manual tracking plugin. For cell tracking experiments in Figure 19 baseline measurements of cell migration, transmitted light images were acquired every minute for a total of 3 h and tracked using FIJI/ImageJ Manual tracking plugin.

3.4.2 Paxillin mutant CHO-K1 cell tracking data

Cell tracking data from previous work in the Brown laboratory was used for this study. Readers are referred to the respective publications for the experimental details, image acquisition parameters and image analysis protocols [B38, B45].

3.4.3 Framework of the simplified 4D mathematical model

We have previously extended a reaction-diffusion model, comprised of the two members of the Rho-family of GTPases, Rac and Rho [B16], to include the adhesion protein paxillin [B21] and its effects on Rac, Rho and adhesion dynamics, through the GIT-PIX-PAK complex. The model consisted of two main modules: the mutual inhibition exerted by Rac and Rho on each other, as well as the positive feedback exerted by active Rac on paxillin phosphorylation which, in turn, exerts positive feedback on Rac activation [B21]. The model was described by a 6D system of partial differential equations (PDEs) dictating the dynamics of the two proteins Rac and Rho scaled concentrations in their active (R, ρ) and inactive (R_i, ρ_i) forms, along with the scaled concentrations of phosphorylated and unphosphorylated forms of paxillin (P, P_i) at serine 273 (S273) residue.

We subsequently simplified this model by making the following physiologically-based assumptions: (i) The synthesis and degradation of Rac, Rho, and paxillin occur on a much slower timescale compared to their reaction kinetics, implying that their total concentrations are conserved [B46–B48]. (ii) Rho dynamics occur at a faster timescale compared to the rest of the model, allowing us to use quasi-steady state approximation to express the scaled concentration of Rho as a function of Rac scaled concentration. (iii) The diffusion of active chemical species are very similar [B49], allowing us to approximate the diffusion coefficient of these chemical species in

their active/phosphorylated forms to be the same.

Taking these three assumptions into account produced a two-dimensional (2D) PDE model, given by

$$\frac{\partial R}{\partial t} = (I_R + I_K^*)\left(\frac{L_\rho^n}{L_\rho^n + \rho^n}\right)(1 - R - \gamma K) - \delta_R R + D_R \frac{\partial^2 R}{\partial x^2} \tag{18a}$$

$$\frac{\partial R_i}{\partial t} = -(I_R + I_K^*)\left(\frac{L_\rho^n}{L_\rho^n + \rho^n}\right)(1 - R - \gamma K) + \delta_R R + D_{R_i} \frac{\partial^2 R_i}{\partial x^2}, \tag{18b}$$

where γ is the ratio of total PAK to total Rac concentrations, K the scaled concentration of active PAK, defined by $\frac{[PAK^*]}{[PAK_{tot}]}$, D_R and D_{R_i} are the diffusion coefficients of R and R_i, respectively, $I_R + I_K^*$ is the sum of the constant basal rate (I_R) and the GIT-PIX-PAK complex-dependent rate (I_K^*) of R activation, δ_R is the inactivation rate of R, L_ρ is the half-maximal inhibition of R by ρ and n is the Hill coefficient. At steady state,

$$\rho = \frac{I_\rho L_R^n}{I_\rho L_R^n + \delta_\rho \left(L_R^n + (R + \gamma K)^n\right)},$$

$$P = \frac{B \frac{K^n}{L_K^n + K^n}}{\alpha_P B \frac{K^n}{L_K^n + K^n} + \delta_P}, \tag{19}$$

$$K = \frac{\alpha_R R}{(1 + k_X[PIX])(1 + \alpha_R R) + \frac{k_G k_X [GIT][PIX]}{1 + k_X[PIX] + \frac{3}{1+R}}}$$

and

$$I_K^* = I_K \times \left(1 - \frac{1}{1.5 + k_X[PIX] + k_G k_X k_C [GIT][PIX][Pax_{tot}]P}\right),$$

where L_K represents the half-maximum phosphorylation of paxillin at steady state, I_K the maximum Rac activation rate, α_P the linearization coefficient between total scaled concentration of paxillin $[Pax_{tot}]$ and scaled concentration of phosphorylated paxillin involved or not in the binding with the GIT-PIX-PAK complex, k_X the association constant for PIX-PAK binding, k_G the association constant for GIT-PIX binding, k_C the association constant for Pax_p-GIT binding, $[GIT]$ the concentration of GIT, $[PIX]$ the concentration of PIX, α_R the affinity constant for PAK-RacGTP binding, δ_ρ the Rho inactivation rate, and δ_P the paxillin dephosphorylation rate [B21, B23]. Technical details of how the three assumptions were implemented to simplify the model can be found in [B39].

This 2D model produces dynamics that are very similar to the original 6D model [B21], including bistability with respect to maximum paxillin phosphorylation rate (B) in the absence of diffusion, as well as the wave-pinning phenomenon, a spatiotemporal pattern with a stable front and back [B26, B27]. In this study, we demonstrated that wave-pinning produces only directed motion that is not consistent with the migration patterns detected

in CHO-K1 cells. To address this issue, we expanded the 2D model into a 4D semi-phenomenological model (Fig. 15a) with three timescales: fast, slow and very slow, to allow for other patterns of activity to arise, including mixed-mode oscillations (MMOs) that combine slow large amplitude with fast small amplitude oscillations within one cycle. The fast variables in this new model are R and R_i, described by Eqs. (18a) and (18b), whereas the slow and the very slow variables are the two parameters - turned into variables - the maximum paxillin phosphorylation rate (B) and the recovery rate of B to its resting state $B_r = 10$ (k_B).

The resulting 4D model is given by

$$\frac{\partial R}{\partial t} = (I_R + I_K^*)\left(\frac{L_\rho^n}{L_\rho^n + \rho^n}\right)(1 - R - \gamma K) - \delta_R R + D_R \frac{\partial^2 R}{\partial x^2} \tag{20a}$$

$$\frac{\partial R_i}{\partial t} = -(I_R + I_K^*)\left(\frac{L_\rho^n}{L_\rho^n + \rho^n}\right)(1 - R - \gamma K) + \delta_R R + D_{R_i} \frac{\partial^2 R_i}{\partial x^2} \tag{20b}$$

$$\frac{\partial B}{dt} = \epsilon\left(1 - \gamma_R R - k_B(B - B_r) + \frac{1}{\eta\,(B + \epsilon_B)}\right) \tag{20c}$$

$$\frac{\partial k_B}{\partial t} = \epsilon_L\,(\gamma_K - R)\,. \tag{20d}$$

The R and R_i equations here are identical to Eqs. (16a) and (16b), respectively, where B was designed to vary slowly compared to R and R_i, so that these fast variables can converge to their steady states before any substantial variation in B can occur. This slow dynamics of B is reflected by the parameter $0 < \epsilon \ll 1$. Mechanistically, R exerts positive (negative) feedback on B on a fast (slow) timescale (Fig. 15a). The new recovery variable k_B, on the other hand, causes the system to exhibit oscillations of varying amplitudes and periods. It possesses the slowest timescale defined by ϵ_L, where $0 < \epsilon_L \ll \epsilon \ll 1$. The combination of these timescales allows R to display unusual dynamic properties at low values of B, manifested as MMOs in the absence of diffusion (Fig. 15b). Descriptions and values of model parameters are given in Table S1. Detailed analysis of MMOs produced by the model are available in [B39].

Here we make four important observations: (i) Although there is a positive feedback from phosphorylated paxillin onto Rac activation, there is no direct feedback from B onto R. (ii) There is no diffusion in the last two equations, implying that they are ordinary differential equations (ODEs). (iii) It is impossible for B to be negative due to the fraction term in Eq. (20c) that acts as a barrier. (iv) The parameter L_K has a direct effect on paxillin phosphorylation (Fig. 15); it can increase or decrease the range of bistability generated by the 4D model of Eqs. (20) in the absence of diffusion when L_K is increased or decreased, respectively.

3.4.4 Numerical simulations of the Cellular Potts Model

The development of the Cellular Potts Model (CPM) for computer-based simulations of migrating cells has provided an excellent tool to analyze cellular motility under varying conditions. This discrete grid-based simulation technique involves the modelling of the extra-cellular matrix (ECM) as a mesh upon which simulated cells are superimposed in the form of compartmentalized discrete objects that can evolve, grow or divide on the surface of this discretized mesh. A Hamiltonian function $H(\mathbf{F};\boldsymbol{\lambda})$ is typically designed to account for forces $\mathbf{F}$, such as pressure caused by actin filaments growth that push the membrane outward, peer contact, or external cues depending on environment-related parameters with different weights defined by $\boldsymbol{\lambda}$. This design is used in Monte Carlo Markov Chain (MCMC)-like simulations to mimic cellular movements, membrane deformation or even cell division, employing classically a stochastic energy minimization principle. In these simulations, the deformable area (or volume, depending on the dimensionality of the simulations) representing the cell has no pre-determined shape and movement, except for physical limitations such as elasticity limit and only responds to energy variation and physical forces.

We used *Morpheus*, a highly flexible CPM simulator software [B50], to simulate a migrating cell. The software allows users to simulate cells under different experimental conditions, parameters values and dynamics, and to account for diffusive molecules in these cells. Our main motivation for choosing this particular CPM was its multi-scale component and its applicability to models expressed as reaction-diffusion equations. The software provides a tool to simulate multi-scale multicellular systems (coupling ODEs, PDEs and CPM in 2D or 3D grid), and to solve the resulting models numerically using the stochastic simulation algorithm. The system described by Eq. (20) requires this multi-scale numerical simulation method Morpheus to elucidate its underlying dynamics.

In our settings, we set the Hamiltonian function to be

$$H = \lambda_P \left(p_{\sigma,t} - P_{target}\right)^2 + \lambda_S \left(s_{\sigma,t} - S_{target}\right)^2 + \lambda_{Act} \left(\Pi_{u \in M(\sigma,t)} Act\left(u\right)\right),$$

where σ denotes the position of the cell at time t, the weights λ_P and λ_S describe the deformation resistance with values tuned to allow the CPM cell to exhibit reasonable membrane elasticity properties [B51, B52], $M(\sigma, t)$ denotes the set of lattices that form the membrane of the cell and the *Act* function measures the amount of actin activity at a specific location. In our general CPM implementation, we substituted actin activity by its equivalent counterpart: the active Rac activity represented by R [B53]. All lattice sites outside the cell in this implementation were assumed to have a nonzero, but very small ($0 < \epsilon_R \ll 1$) level of R; this makes Rac activities in these lattice sites negligible. Based on that, the software updates membrane localization by favouring membrane expansion in the regions where R is high, i.e. Rac activity is the highest, causing membrane

protrusions. The level of R is each lattice site in the newly updated configuration of the cell is then dictated by the software.

3.4.5 Cell tracking

CHO-K1 cells were manually tracked in FIJI/ImageJ (NIH, Bethesda, MD) using the manual tracking plugin by clicking on the centre of the cell frame-by-frame for each motile cell in the image time series. The centre of the CHO-K1 cell nucleus was used as the reference point for each cell. Important to note that no significant difference was detected when tracking a CHO-K1 cell using its centre of nucleus or centre of cytoplasm or centre of mass. User bias was minimized by having several authors track the CHO-K1 cells. Cell tracking data from work that was previously published by the Brown laboratory were also used for these studies. Tracking data for WT-paxillin-EGFP expressing CHO-K1 cells were from [B38] and CHO-K1 cells expressing EGFP paxillin fusions of WT, S273A or S273D paxillin constructs were from [B45]. Simulated CPM cells were automatically tracked by Morpheus. There are slight differences across studies in image acquisition methods (i.e. transmitted light versus fluorescence imaging) and settings and cell tracking protocols. Details in the methods section refer to new experiments conducted for these studies and tracked using the methods described above. The reader is referred to the two aforementioned studies for the details of cell tracking for the appropriate figures. The x and y position data for each CHO-K1 and CPM cell track was then exported to Python. Rose plots were created by superimposing the starting position of each cell track on the origin $(0, 0)$. The speed of each cell was then calculated by taking the mean of the distance travelled between each time point over the imaging interval, generating the metric "instantaneous speed". The data shown represents the mean $\pm$ standard error of the mean (SEM) for all CHO-K1 and CPM cells analyzed.

3.4.6 Comparison framework

In the absence of diffusion, the new simplified model, given by Eqs. 20, exhibits not only bistability (and thus wave-pinning in the presence of diffusion in R and R_i), but also relaxation oscillations (ROs) and mixed-mode oscillations (MMOs) [B39]. Thus one would expect that these diverse temporal profiles will generate different migration patterns in the simulated CPM as long as the dynamics are governed by Eqs. (20). To quantitatively verify if such migration patterns of the CPM are similar to those exhibited by motile CHO-K1 cells, an analysis framework was built to fully characterize and compare motile behaviours between simulated cell tracks and tracks from experimental timelapse movies of cells. The framework compares migration patterns by focusing on speed, persistence, directionality and membrane activity as defined below.

3.4.6.1 Analysis of paths: metrics for quantifying cell movement Motile cells can exhibit random motion in their migratory patterns. However, some cells may also display active migratory patterns that are not due to biological noise. Quantitative approaches can be employed to distinguish between the two. In normal diffusion, the mean-square displacement of a diffusing cell, defined by

$$\text{MSD(t)} = ||\mathbf{x(t)} - \mathbf{x(0)}||^{\mathbf{2}}_{\mathbf{2}},$$

where $\mathbf{x(t)}$ is the position of the cell's centre of mass at time t, is proportional to t; this applies to a cell whose motility is not driven by any concrete force but rather by the noisy fluctuations in the cell's shape. However, diffusion can be hindered or enhanced, making MSD proportional to some power of time t^{α}, given by

$$\text{MSD(t)} = t^{\alpha}, \tag{21}$$

with $\alpha < 1$ (> 1) indicating hindered (enhanced) diffusion.

For directed motion, MSD becomes proportional to t^2 [B54]. For this reason, it is more common to consider the mean-square displacement through time in log-scale and use the slope of the curve (referred to hereafter as "α-value") as a metric to determine the level of directionality [B55, B56]. When α is close to 1, the motion is random, when $\alpha > 1$, the motion is said to be superdiffusive, indicating that there is an active force driving directionality, and when $\alpha < 1$, the motion is said to be subdiffusive or the cell is somehow confined. For an actively migrating cell with a speed v, the trajectory of this cell will simultaneously exhibit both superdiffusive and diffusive (random) motion because of the presence of biological noise. Here, the α-value was used to automatically classify their activity.

As with every metric, MSD has its pitfalls. Specifically, a cell that follows a curved path while maintaining an approximately constant distance from its starting point would have the same MSD as that of an immotile cell. To resolve this issue, another metric called the directionality ratio (DR) that quantifies the straightness of motion [B57, B58] was also used. It is defined to be the ratio between the straight-line length from the starting point to the endpoint of the migration path, d, and the total length of the path along the trajectory, D, i.e., DR= d/D. According to this definition, it follows that a DR is roughly 1 for a straight trajectory and much closer to 0 for an almost stationary trajectory. Directionality ratio has its own limitations because it may attain small values for trajectories that exhibit piece-wise directed motion. In this case MSD of such trajectory should be further assessed.

3.4.6.2 Detection of changes in direction To characterize cell movement, a two-step approach was implemented. In the first step, an approximate value of the prevailing α-value over time was computed by applying log-log regression on the MSD and measuring the slope. This was done on every 20-min-long segment of the recording for CHO-K1 cells (70 segments in total), or 50 time-step-long segments for CPM cells (350 segments in total), and then averaged. A threshold value of $\alpha = 1.4$ was found to be the most suitable in differentiating between active or motile cells (when $\alpha > 1.4$) versus those that are inactive or moving randomly (when $\alpha < 1.4$).

Trajectories of active CHO-K1 cells are typically "piece-wise directional", i.e, they exhibit a sequence of directed motions (referred to hereafter as "periods of directedness") separated by events at which cells abruptly change directionality. To ensure an unbiased and self-consistent detection of all these possible changes in direction or "events", we applied the second step in characterizing cell motion. In this step, a 60-min rolling window for CHO-K1 cells and 50 time-steps for CPM cells was used to compute the DR of a portion of the trajectory; the rolling window was then shifted by 1-min (one time-step) in the former (latter) and the computation was repeated. During periods of directedness, DR values are high (essentially above 0.8). This means that when the rolling window is overlapping with an event and is no longer purely covering one period of directedness, a significant drop in DR occurs. A minimum DR is thus attained when half of the window is in the preceding period of directness, relative to the event, while the other half is in the following period. By computing the DR values and applying non-frequency-based smoothing [B59] of the DR time series, pronounced dips in times series were detected. These dips represent the events of abrupt change in directionality.

Note that tracks of inactive cells also exhibit fluctuations in DR with spikes and dips that are quite frequent. This is because DR does not include any normalization in terms of travelled distance or speed. Indeed, any Wiener process would have a noisy DR time series that sometimes reaches high values. Fortunately, these inactive cells also show very low α-values. Such feature can be further used to distinguish between active and inactive cells, along with the computation of confidence interval for the DR. This was how we overcame the main difficulties in the event detection task.

3.4.6.3 Cell protrusion and shape To investigate cell protrusion and shape in CHO-K1 and CPM cells, "binary masks" of these two cell types were extracted [B60]. These masks indicate where the entire body of the cell lies, allowing for visual identification of protrusions in the membrane and distortion or stretching in the general shape of a CHO-K1 and CPM cell (Fig. 22).

Fiji/ImageJ was used to generate binary masks of CHO-K1 cells by applying a classic image-segmentation framework. The cells appeared as fluorescence intensity on a dark background; pixel background intensity signal was subtracted using the "Subtract Background" plug-in with default values; the brightness and contrast were

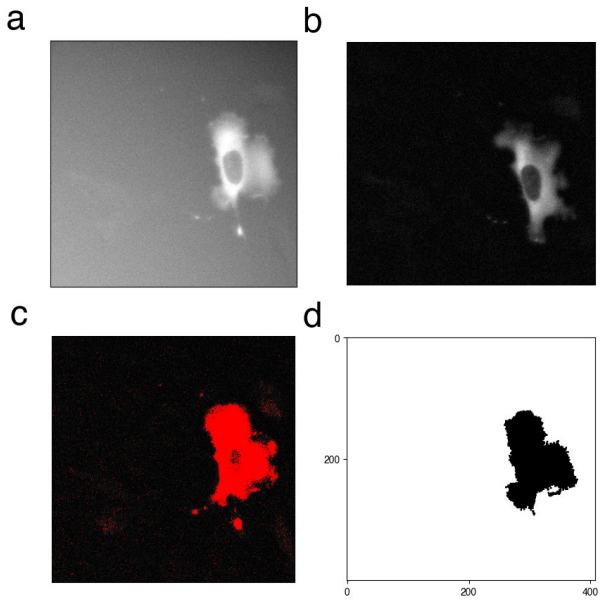

Figure 22: Image processing of motile cells. (a) A widefield fluorescence microscopy image of a CHO-K1 cell expressing WT-paxillin-EGFP. Such images often have a light halo and noisy background, that are (b) filtered to obtain a high signal-to-noise image, and then (c) thresholded to generate a binary image and detect the entire cell body by applying the "find-particle" Fiji/ImageJ plug-in, resulting in (d) a binary mask of the cell. For the CPM cell, the binary masks in step d are generated directly without the need for the first three steps a-c because, by definition, the simulated images have pixels with signal and pixels that have no signal.

adjusted to visualize the cells and images were thresholded to obtain black-and-white binary images using the "Threshold" plug-in, with the default settings except that "dark background" and "Otsu" filter settings were selected. The "Find -particles" algorithm was then used to identify the near-circular objects in the binary images with default settings except that "include holes" and "exclude on edges" were selected. The range of circularity was set to $[0.3 - 1.0]$, minimum size to 1000 (in term of pixel count), allowing for CHO-K1 cell detection. With CPM simulations, the exact lattices (or pixels) occupied by the cell were known, making the exact detection of the cell body and generation of binary masks more straightforward. Binary masks were obtained for different motility patterns detected in CHO-K1 and CPM cells.

From the binary masks of CHO-K1 and CPM cells, changes in cell area due to protrusions and retractions in the membrane were then visually assessed. Here, we subtracted consecutive cell binary masks to count (in pixels) the size of deformations from one image to the next, in order to measure the metric "level of membrane activity". When a CHO-K1 or CPM cell moves forward, it is not sliding on the substrate, but rather dynamically extending its edge by forming a protrusion and retracting its rear. This leads to a displacement, and the mask subtraction is supposed to highlight these two sites of membrane deformation, i.e. the front and the rear. If masks were to be realigned, the level of membrane activity would then be close to zero, especially during periods

of directedness in which CHO-K1 or CPM cells roughly preserve their shapes during migration. That is why masks were not recentred to align the two barycenters of a cell.

3.4.7 Statistical analysis

Statistical analysis was performed using PRISM software (GraphPad). Mann-Whitney tests were performed. Statistical significance was accepted at *P $< 10^{-1}$, **P $< 10^{-2}$, ***P $< 10^{-3}$ and ****P $< 10^{-4}$. Linear regression was performed using the standard method of ordinary least squares, and run on Python with its implementation from the *sklearn* Library.

3.4.8 Machine classifier

We chose to implement our classifier as a neural network, using the simulated wildtype-like, S273A-like and S273D-like CPM cells for training. As demonstrated below, the set of metrics already established in this study was quite effective in capturing the differences between the three conditions of CHO-K1 cells. We therefore chose to restrict ourselves to a very simplified architecture for the neural network; this allowed the algorithm to use the metrics efficiently and adequately with limited processing, as well as facilitated the interpretation of the results produced while reducing the risk of overfitting. The architecture consisted of 4 fully-connected layers, with a rectified linear unit (ReLU) function. The network was given the following four metrics: mean instantaneous speed of the cell, mean alpha-value, directionality ratio and number of events representing change in directionality. It must be pointed out that the units of the speed are different between the CHO-K1 cells and the CPM cells, whereas all other metrics share the same units. For this reason, we normalized the speed across all samples and kept all the other metrics unchanged. Varying the classifier, the training set and the architecture of the network, we always obtained an accuracy above 90 percent. With the adopted architecture of 3 layers, ReLU activation function and a randomized choice of 10 CPM cells per condition (wildtype-like, S273A-like and S273D-like) to form the training set, 95% was the minimum accuracy obtained, and it often reached 100 percent.

3.4.9 Software

The CPM was simulated using Morpheus (an open source software developed at the Technische Universität Dresden [B50], available here). Its graphical user interface supports the entire workflow from model construction and simulation to visualization, archiving and batch processing. Plotting and classification were done using Python 3.8.12. For the machine classifier, we used the implementation of Multi-layer Perceptron classifier from the Python library Scikit learn; it was trained using the default value setting except for the choice of the solver (selected to be 'lbfgs'), and the regularization parameter (set to be $\alpha = 10^{-5}$). The codes used for producing the

simulations can be obtained online [B61].

Data availability statement

The datasets used and/or analysed during the current study are available from the corresponding author on reasonable request.

References

[B1] Friedl, P. & Wolf, K. Plasticity of cell migration: a multiscale tuning model. *Journal of Cell Biology* **188**, 11–19 (2010).

[B2] Swaney, K. F., Huang, C.-H. & Devreotes, P. N. Eukaryotic chemotaxis: a network of signaling pathways controls motility, directional sensing, and polarity. *Annual review of biophysics* **39**, 265 (2010).

[B3] Lauffenburger, D. A. & Horwitz, A. F. Cell migration: a physically integrated molecular process. *cell* **84**, 359–369 (1996).

[B4] Burridge, K. & Wennerberg, K. Rho and rac take center stage. *Cell* **116**, 167–179 (2004).

[B5] Sadok, A. & Marshall, C. J. Rho gtpases: masters of cell migration. *Small GTPases* **5**, e983878 (2014).

[B6] Jaffe, A. B. & Hall, A. Rho gtpases: biochemistry and biology. *Annual review of cell and developmental biology* **21**, 247–269 (2005).

[B7] Scarpa, E. & Mayor, R. Collective cell migration in development. *Journal of Cell Biology* **212**, 143–155 (2016).

[B8] Li, L., He, Y., Zhao, M. & Jiang, J. Collective cell migration: Implications for wound healing and cancer invasion. *Burns & trauma* **1**, 2321–3868 (2013).

[B9] Zipkin, I. D., Kindt, R. M. & Kenyon, C. J. Role of a new rho family member in cell migration and axon guidance in c. elegans. *Cell* **90**, 883–894 (1997).

[B10] Hanahan, D. & Weinberg, R. A. Hallmarks of cancer: the next generation. *cell* **144**, 646–674 (2011).

[B11] Patel, S. *et al.* The cell motility modulator slit2 is a potent inhibitor of platelet function. *Circulation* **126**, 1385–1395 (2012).

[B12] Merino-Casallo, F., Gomez-Benito, M. J., Hervas-Raluy, S. & Garcia-Aznar, J. M. Unravelling cell migration: defining movement from the cell surface. *Cell Adhesion & Migration* **16**, 25–64 (2022).

[B13] Winograd-Katz, S. E., Fässler, R., Geiger, B. & Legate, K. R. The integrin adhesome: from genes and proteins to human disease. *Nature reviews Molecular cell biology* **15**, 273–288 (2014).

[B14] Drubin, D. G. & Nelson, W. J. Origins of cell polarity. *Cell* **84**, 335–344 (1996).

[B15] Nobes, C. D. & Hall, A. Rho, rac, and cdc42 gtpases regulate the assembly of multimolecular focal complexes associated with actin stress fibers, lamellipodia, and filopodia. *Cell* **81**, 53–62 (1995).

[B16] Ridley, A. J., Paterson, H. F., Johnston, C. L., Diekmann, D. & Hall, A. The small gtp-binding protein rac regulates growth factor-induced membrane ruffling. *Cell* **70**, 401–410 (1992).

[B17] Ridley, A. J. Rho gtpases and cell migration. *Journal of cell science* **114**, 2713–2722 (2001).

[B18] Heasman, S. J. & Ridley, A. J. Mammalian rho gtpases: new insights into their functions from in vivo studies. *Nature reviews Molecular cell biology* **9**, 690–701 (2008).

[B19] Jilkine, A., Marée, A. F. & Edelstein-Keshet, L. Mathematical model for spatial segregation of the rho-family gtpases based on inhibitory crosstalk. *Bulletin of mathematical biology* **69**, 1943–1978 (2007).

[B20] Lyda, J. K. *et al.* Rac activation is key to cell motility and directionality: an experimental and modelling investigation. *Computational and structural biotechnology journal* (2019).

[B21] Tang, K., Boudreau, C. G., Brown, C. M. & Khadra, A. Paxillin phosphorylation at serine 273 and its effects on rac, rho and adhesion dynamics. *PLoS computational biology* **14**, e1006303 (2018).

[B22] Nayal, A. *et al.* Paxillin phosphorylation at ser273 localizes a git1–pix–pak complex and regulates adhesion and protrusion dynamics. *The Journal of cell biology* **173**, 587–589 (2006).

[B23] Lyda, J. K. *et al.* Rac activation is key to cell motility and directionality: an experimental and modelling investigation. *Computational and Structural Biotechnology Journal* **17**, 1436–1452 (2019).

[B24] Rajah, A. *et al.* Paxillin s273 phosphorylation regulates adhesion dynamics and cell migration through a common protein complex with pak1 and βpix. *Scientific reports* **9**, 1–20 (2019).

[B25] L, E.-K., WR, H., M, Z. & M., D. From simple to detailed models for cell polarization. *Philosophical transactions of the Royal Society* (2013).

[B26] Mori, Y., Jilkine, A. & Edelstein-Keshet, L. Wave-pinning and cell polarity from a bistable reaction-diffusion system. *Biophysical journal* **94**, 3684–3697 (2008).

[B27] Mori, Y., Jilkine, A. & Edelstein-Keshet, L. Asymptotic and bifurcation analysis of wave-pinning in a reaction-diffusion model for cell polarization. *SIAM Journal on applied mathematics* **71**, 1401–1427 (2011).

[B28] Schreiber, C., Amiri, B., Heyn, J. C., Rädler, J. O. & Falcke, M. On the adhesion–velocity relation and length adaptation of motile cells on stepped fibronectin lanes. *Proceedings of the National Academy of Sciences* **118** (2021).

[B29] Allard, J. & Mogilner, A. Traveling waves in actin dynamics and cell motility. *Current opinion in cell biology* **25**, 107–115 (2013).

[B30] Barnhart, E. L., Allen, G. M., Jülicher, F. & Theriot, J. A. Bipedal locomotion in crawling cells. *Biophysical journal* **98**, 933–942 (2010).

[B31] Ehrengruber, M. U., Deranleau, D. A. & Coates, T. D. Shape oscillations of human neutrophil leukocytes: characterization and relationship to cell motility. *The Journal of experimental biology* **199**, 741–747 (1996).

[B32] Barnhart, E. L., Allard, J., Lou, S. S., Theriot, J. A. & Mogilner, A. Adhesion-dependent wave generation in crawling cells. *Current Biology* **27**, 27–38 (2017).

[B33] MacKay, L., Lehman, E. & Khadra, A. Deciphering the dynamics of lamellipodium in a fish keratocytes model. *Journal of Theoretical Biology* **512**, 110534 (2021).

[B34] Lavi, I., Piel, M., Lennon-Duménil, A.-M., Voituriez, R. & Gov, N. S. Deterministic patterns in cell motility. *Nature Physics* **12**, 1146–1152 (2016).

[B35] Holmes, W. R., Park, J., Levchenko, A. & Edelstein-Keshet, L. A mathematical model coupling polarity signaling to cell adhesion explains diverse cell migration patterns. *PLoS computational biology* **13**, e1005524 (2017).

[B36] Rens, E. G. & Edelstein-Keshet, L. Cellular tango: how extracellular matrix adhesion choreographs rac-rho signaling and cell movement. *Physical biology* **18**, 066005 (2021).

[B37] Marée, A. F., Grieneisen, V. A. & Hogeweg, P. The cellular potts model and biophysical properties of cells, tissues and morphogenesis. In *Single-cell-based models in biology and medicine*, 107–136 (Springer, 2007).

[B38] Kiepas, A., Voorand, E., Mubaid, F., Siegel, P. M. & Brown, C. M. Optimizing live-cell fluorescence imaging conditions to minimize phototoxicity. *Journal of cell science* **133**, jcs242834 (2020).

[B39] Plazen, L. & Khadra, A. Excitable dynamics in a molecularly-explicit model of cell motility: Mixed-mode oscillations and beyond. *bioRxiv* (2022).

[B40] Desroches, M. *et al.* Mixed-mode oscillations with multiple time scales. *Siam Review* **54**, 211–288 (2012).

[B41] Holmes, W. R., Carlsson, A. E. & Edelstein-Keshet, L. Regimes of wave type patterning driven by refractory actin feedback: transition from static polarization to dynamic wave behaviour. *Physical biology* **9**, 046005 (2012).

[B42] Gamper, N., Stockand, J. D. & Shapiro, M. S. The use of chinese hamster ovary (cho) cells in the study of ion channels. *Journal of pharmacological and toxicological methods* **51**, 177–185 (2005).

[B43] Grove, M., Timbrell, L., Jolley, B., Polack, F. & Borg, J. M. The importance of noise colour in simulations of evolutionary systems. *Artificial Life* **27**, 164–182 (2022).

[B44] Spagnolo, B. *et al.* Noise effects in two different biological systems. *The European Physical Journal B* **69**, 133–146 (2009).

[B45] Rajah, A. *The paxillin serine 273 phosphorylation signaling pathway positively regulates cell migration, persistence and protein dynamics.* Master's thesis, McGill University, Department of Physiology (2020).

[B46] Kovacic, H. N., Irani, K. & Goldschmidt-Clermont, P. J. Redox regulation of human rac1 stability by the proteasome in human aortic endothelial cells. *Journal of Biological Chemistry* **276**, 45856–45861 (2001).

[B47] Chen, Y. *et al.* Cullin mediates degradation of rhoa through evolutionarily conserved btb adaptors to control actin cytoskeleton structure and cell movement. *Molecular cell* **35**, 841–855 (2009).

[B48] Chay, K.-O., Park, S. S. & Mushinski, J. F. Linkage of caspase-mediated degradation of paxillin to apoptosis in ba/f3 murine pro-b lymphocytes. *Journal of Biological Chemistry* **277**, 14521–14529 (2002).

[B49] Das, S. *et al.* Single-molecule tracking of small gtpase rac1 uncovers spatial regulation of membrane translocation and mechanism for polarized signaling. *Proceedings of the National Academy of Sciences* **112**, E267–E276 (2015).

[B50] Starruß, J., de Back, W., Brusch, L. & Deutsch, A. Morpheus: a user-friendly modeling environment for multiscale and multicellular systems biology. *Bioinformatics* **30**, 1331–1332 (2014). URL `https://doi.org/10.1093/bioinformatics/btt772`. `http://oup.prod.sis.lan/bioinformatics/article-pdf/30/9/1331/17343853/btt772.pdf`.

[B51] Graner, F. & Glazier, J. A. Simulation of biological cell sorting using a two-dimensional extended potts model. *Physical Review Letters* **69**, 2013 – 2016 (1992).

[B52] Niculescu, I., Textor, J. & de Boer, R. J. Crawling and gliding: A computational model for shape-driven cell migration. *PLOS Computational Biology* **11** (2015).

[B53] Waterman-Storer, C. M. & Salmon, E. Positive feedback interactions between microtubule and actin dynamics during cell motility. *Current opinion in cell biology* **11**, 61–67 (1999).

[B54] Karatzas, I. & Shreve, S. *Brownian motion and stochastic calculus*, vol. 113 (Springer Science & Business Media, 2012).

[B55] Saxton, M. J. A biological interpretation of transient anomalous subdiffusion. i. qualitative model. *Biophysical journal* **92**, 1178–1191 (2007).

[B56] Loosley, A. J., O'Brien, X. M., Reichner, J. S. & Tang, J. X. Describing directional cell migration with a characteristic directionality time. *PloS one* **10**, e0127425 (2015).

[B57] Roman, G. & Alexis, G. Quantitative and unbiased analysis of directional persistence in cell migration. *Nature Protocols* **9**, 1931–1943 (2014).

[B58] Stéphanou, A., Le Floc'h, S. & Chauvière, A. A hybrid model to test the importance of mechanical cues driving cell migration in angiogenesis. *Mathematical Modelling of Natural Phenomena* **10**, 142–166 (2015).

[B59] Savitzky, A. & Golay, M. J. Smoothing and differentiation of data by simplified least squares procedures. *Analytical chemistry* **36**, 1627–1639 (1964).

[B60] Schneider, C. A., Rasband, W. S. & Eliceiri, K. W. Nih image to imagej: 25 years of image analysis. *Nature methods* **9**, 671–675 (2012).

[B61] Plazen, L., Rahbani, J., Brown, C. M. & Khadra, A. Data from: Polarity and mixed-mode oscillations may underlie different patterns of cellular migration profiles (2022). URL `http://www.medicine.mcgill.ca/physio/khadralab/Codes/code_SciRep1.html`.

Author Contributions

L.P.: Formal analysis; Investigation; Methodology; Software; Validation; Writing - original draft.

J.A.R.: Data curation; Writing - review & editing.

C.M.B.: Data curation; Resources; Supervision; Funding acquisition; Writing - review & editing.

A.K.: Conceptualization; Funding acquisition; Methodology; Project administration; Resources; Supervision; Writing - original draft; Writing - review & editing.

Acknowledgments

We thank Alexander Kiepas for providing the CHO-K1 tracking data that were part of a previous manuscript Kiepas A, Voorand E, Mubaid F, Siegel PM, Brown CM. Optimizing live-cell fluorescence imaging conditions to minimize phototoxicity. *J Cell Sci.* (2020) doi: 10.1242/jcs.242834. PMID: 31988150 for further analysis. We thank Abira Rajah for providing the tracking data for cells expressing the wild-type-paxillin-EGFP, paxillin-S273A-EGFP or paxillin-S273D-EGFP that were previously published in her master Thesis *The paxillin serine 273 phosphorylation signaling pathway positively regulates cell migration, persistence and protein dynamics*, 2020, McGill University for further analysis. All microscopy, some image analysis and some cell tracking was performed at the McGill University Advanced BioImaging Facility (ABIF) $RRID : SCR\_017697$.

4 Conclusion and futures directions

4.1 Limitations

4.1.1 Experimental Data

Acquisition and access to data of living CHO-K1 cells was essential for this study. The data enabled us to support our statistical tests and to strengthen our analysis, by going back and forth between predictions of the model and biological observations throughout the whole project. Nevertheless, difficulties to deal with the inherent nature of the CHO-K1 cells must not be underestimated. Cells constantly go through a variety of biological processes not related to motility. For example CHO-K1 cells divide every eighteen hours. Prior to mitosis, the cells grow during this period. This, as a result, may interfere with the experimental observations being measured, such as cell size (assumed to be constant); this is especially relevant when measuring the level of membrane activity. In addition to that, actin cytoskeleton is known to be essential for mitosis [64] and experiences a tightly regulated morphological transformation during cell division. Actin network also plays an important mitotic role in the separation of centrosomes [65]. Indeed, for cytokinesis to occur, actin undergoes a reorganization to become part of the contractile ring (pinching the plasma membrane inward, and forming what is called a cleavage furrow, to separate the cell in half) [66]. In this situation, change in cell shape cannot be attributed only to motile strengths. After mitosis, the two daughter cells experience a short phase of brief repulsion which rely on the actin cytoskeleton of the daughters cells. This increases their speed and restrict the scope of movement. In our situation, where we wanted to identify slow phenomena that take hours to capture, all these limitations may have affect our analysis. To mitigate that, manual selection of cells that were imaged outside the period of mitosis was performed to calculate the level of membrane activity. Doing so reduced the time and number of data that can be used.

4.1.2 Model simplification

Simplification of the six-dimensional initial model tend to fade out the importance and role of the GIT-PIX-PAK complex, as we linearized the relation between total amount of paxillin and the phosphorylated paxillin involved or not in the binding with the GIT-PIX-PAK complex. If the model were to be re used in the context of a study on binding affinity for GIT, PIX or PAK protein, the linearization coefficient α_P should be recomputed or estimated again. The linearization could be replaced by a more precise or exact function. Still, the focus of our work was to showcase the important of paxillin phosphorylation temporal dynamic, which is what motivated this simplification.

4.2 Future directions

4.2.1 Paxillin phosphorylation sites

Phosphorylation of paxillin at serine 273 was studied using both models and data in this thesis. Still, paxillin possesses other phosphorylation cites. Similar to PAK1-mediated paxillin-S273 phosphorylation, FAKSrc-mediated phosphorylation of paxillin at tyrosine 31 (Y31) and 118 (Y118) in the LD2 domain of paxillin is an important regulator of cell migration and adhesion dynamics [44]. Mutations of these two sites can generate other type of paxillin mutants that can be characterized with the metrics developed in this thesis. Following our work, models of cell motility based on paxillin phosphorylation at tyrosine 31 or tyrosine 118 could be developed.

In addition, it is known that tyrosine and serine phosphorylation of paxillin, individually, serve to promote the migratory phenotype. Work done by Zhang *et al* revealed that paxillin Y31 and Y118 phosphorylation precedes and is a requirement for S273 phosphorylation for lung airway smooth muscle contraction [67]. Signalling pathways in cell motility are known to be redundant and complex. Integrating the effects of these three phosphorylation sites on paxillin in a single model could help untangle the interactions between them; it could also help understand the scope and power of redundancy in these pathways and their limitations. The multiplicity of phosphorylation sites that all promote dynamic adhesion and rapid migration is not yet understood. This could also be studied experimentally as our collaborator (Brown Lab, McGill University) has recently succeeded in targeting all three residues (S273, Y31 and Y118) to generate non-phosphorylatable paxillin mutants (also known as CHO-K1 triple-knockout mutant cells).

4.2.2 Partial Differential Equations models

The purpose of this study was to decipher the dynamic of the protein-protein interactions involved in cell motility through mathematical modelling, by providing, among other findings, important results on the dynamical properties of the system. We provided a complete analysis of the ODE system in terms of stability properties; it answers the question of how small perturbations could evolve over time in an ordinary differential equation system.

In the partial differential equations models, the previous results can be generalized to answer the question of how the system would react to small homogeneous perturbations. Still, perturbation can now also occur locally. In such scenarios, diffusion must be taken into account to understand the subsequent effect of a small localized change in one of the concentrations can have. Local Perturbation Analysis (LPA) [68] is a framework that tracks the approximate early evolution of an arbitrarily large perturbation of a homogeneous steady state and can provide an approximation of the spatial stability properties of a PDE system. This general framework is based

on the following three assumptions:

1. There are only two groups of chemical species: slow-diffusing and fast-diffusing.

2. Fast-diffusing species are homogeneously distributed.

3. Slow-diffusing species do not diffuse at all.

Details of the resulting system, bifurcation diagram and numerical resolutions of the model can be found in the Supplementary Material of this thesis. In this analysis, we found that the 2D PDE model is homogeneously stable in the bistable regime when $B \leq 2.7$. The model then shows a transcritical bifurcation at $B = 2.7$ which makes the low global steady state become unstable. For B values above 2.7, perturbation of a very small amplitude, starting from the basin of attraction of the low global steady state, can cause gain in Rac activation to reach the upper stable branch.

Using Local Perturbation Analysis [68], we have thus shown that this simplified model possesses spatial instability regions within which a small perturbation in protein concentration can arise and grow in amplitude, allowing for the generation of, for example, a wave of active Rac protein. In other words, self-polarization of the cell from the low steady state can happened in this regime. This provides an explanation for the ability of cells in nature to develop a polarized profile without any artificially large break in symmetry. The study of the impact that spatial instabilities can have on our slow-fast models could provide new information on cell motility and remains to be done.

4.2.3 Patterns in the four-dimensional reaction-diffusion model

To our knowledge, only the wave-pinning phenomenon has been entirely analytically studied when it comes to reaction-diffusion models in cell motility. Still, it is a very simple spatial pattern, and is apparently the only one which can be observed and which stays stable in a model with two variables. No other pattern more complex in the Rac-Rho subsystem were demonstrated, and different sources agree that any spatial formation would eventually evolve to form the wave, or homogenize across the domain [61]. Nevertheless, our refined model possesses different timescales, and two more variables that are not defusing. Adding this level of complexity could lead to the emergence of complex spatial dynamics.

The PDE model could not be solved analytically here. We observed some spatial patterns through numerical simulations, first on *Matlab* on a simple spatial domain in one dimension, and then on *Morpheus* in the more complex domain which is the cell. The patterns produced matched our expectations but a more thorough analysis could uncover new diffusive phenomena that we would have missed. It cannot be ensured that all of what the

system can produce have been seen. Slow-fast analysis of the PDE model could lead to new discoveries and deserve a thorough study. LPA can provide a way to approach this topic, as was done in the previous subsection.

4.3 Conclusions

The purpose of this study was to decipher the dynamics of the interactions between Rac and paxillin by building simple models which would be tractable and would emphasize the role and importance of different timescales in the time evolution of the activation/phosphorylation of these proteins. By the mean of mathematical modelling and subsequent computer simulations, we have shown that a Cellular Potts Model algorithm based on our 4D PDE model was capable of generating cells that are highly similar to living CH0-K1 cells. We developed metric tools to characterize cell motility that served to support this claim and that could be generalized to other motility studies. The model was shown to capture the effects of paxillin mutations as well, through one parameter related to both adhesion dynamic and paxillin phosphorylation sensitivity to active PAK concentration. The simplicity of the models, viewed in parallel with the complexity of the resulting dynamical time evolution, showed that complex dynamical behaviours can emerge when non-linearity and separation of time scales are included, and that these dynamics can consequently be responsible for rich and diverse motile patterns in migrating cells.

References

[1] Plazen, L. & Khadra, A. Excitable dynamics in a molecularly-explicit model of cell motility: Mixed-mode oscillations and beyond. *bioRxiv* (2022).

[2] Plazen, L., Al Rahbani, J., Brown, C. M. & Khadra, A. Polarity and mixed-mode oscillations may underlie different patterns of cellular migration. *bioRxiv* (2022).

[3] Li, L., He, Y., Zhao, M. & Jiang, J. Collective cell migration: Implications for wound healing and cancer invasion. *Burns & trauma* **1**, 2321–3868 (2013).

[4] Scarpa, E. & Mayor, R. Collective cell migration in development. *Journal of Cell Biology* **212**, 143–155 (2016).

[5] Lamalice, L., Le Boeuf, F. & Huot, J. Endothelial cell migration during angiogenesis. *Circulation research* **100**, 782–794 (2007).

[6] Zipkin, I. D., Kindt, R. M. & Kenyon, C. J. Role of a new rho family member in cell migration and axon guidance in c. elegans. *Cell* **90**, 883–894 (1997).

[7] Hanahan, D. & Weinberg, R. A. Hallmarks of cancer: the next generation. *cell* **144**, 646–674 (2011).

[8] Patel, S. *et al.* The cell motility modulator slit2 is a potent inhibitor of platelet function. *Circulation* **126**, 1385–1395 (2012).

[9] Talkenberger, K., Cavalcanti-Adam, E. A., Voss-Böhme, A. & Deutsch, A. Amoeboid-mesenchymal migration plasticity promotes invasion only in complex heterogeneous microenvironments. *Scientific reports* **7**, 1–12 (2017).

[10] Van Helvert, S., Storm, C. & Friedl, P. Mechanoreciprocity in cell migration. *Nature cell biology* **20**, 8–20 (2018).

[11] Bodor, D. L., Pönisch, W., Endres, R. G. & Paluch, E. K. Of cell shapes and motion: the physical basis of animal cell migration. *Developmental cell* **52**, 550–562 (2020).

[12] Yamazaki, D., Kurisu, S. & Takenawa, T. Regulation of cancer cell motility through actin reorganization. *Cancer science* **96**, 379–386 (2005).

[13] Friedl, P. & Weigelin, B. Interstitial leukocyte migration and immune function. *Nature immunology* **9**, 960–969 (2008).

[14] Trepat, X. *et al.* Physical forces during collective cell migration. *Nature physics* **5**, 426–430 (2009).

[15] Friedl, P. & Gilmour, D. Collective cell migration in morphogenesis, regeneration and cancer. *Nature reviews Molecular cell biology* **10**, 445–457 (2009).

[16] Perez, T. & Nelson, W. Cadherin adhesion: mechanisms and molecular interactions. In *Cell adhesion*, 3–21 (Springer, 2004).

[17] Sadok, A. & Marshall, C. J. Rho gtpases: masters of cell migration. *Small GTPases* **5**, e983878 (2014).

[18] Martin, K. *et al.* Spatio-temporal co-ordination of rhoa, rac1 and cdc42 activation during prototypical edge protrusion and retraction dynamics. *Scientific Reports* **6**, 1–14 (2016).

[19] Drubin, D. G. & Nelson, W. J. Origins of cell polarity. *Cell* **84**, 335–344 (1996).

[20] Burridge, K. & Wennerberg, K. Rho and rac take center stage. *Cell* **116**, 167–179 (2004).

[21] Ridley, A. J., Paterson, H. F., Johnston, C. L., Diekmann, D. & Hall, A. The small gtp-binding protein rac regulates growth factor-induced membrane ruffling. *Cell* **70**, 401–410 (1992).

[22] Ridley, A. J. Rho gtpases and cell migration. *Journal of cell science* **114**, 2713–2722 (2001).

[23] Nobes, C. D. & Hall, A. Rho, rac, and cdc42 gtpases regulate the assembly of multimolecular focal complexes associated with actin stress fibers, lamellipodia, and filopodia. *Cell* **81**, 53–62 (1995).

[24] Heasman, S. J. & Ridley, A. J. Mammalian rho gtpases: new insights into their functions from in vivo studies. *Nature reviews Molecular cell biology* **9**, 690–701 (2008).

[25] Jilkine, A., Marée, A. F. & Edelstein-Keshet, L. Mathematical model for spatial segregation of the rho-family gtpases based on inhibitory crosstalk. *Bulletin of mathematical biology* **69**, 1943–1978 (2007).

[26] Lyda, J. K. *et al.* Rac activation is key to cell motility and directionality: an experimental and modelling investigation. *Computational and structural biotechnology journal* (2019).

[27] Turner, C. E., West, K. A. & Brown, M. C. Paxillin–arf gap signaling and the cytoskeleton. *Current opinion in cell biology* **13**, 593–599 (2001).

[28] Tang, K., Boudreau, C. G., Brown, C. M. & Khadra, A. Paxillin phosphorylation at serine 273 and its effects on rac, rho and adhesion dynamics. *PLoS computational biology* **14**, e1006303 (2018).

[29] Guo, Y. *et al.* R-ketorolac targets cdc42 and rac1 and alters ovarian cancer cell behaviors critical for invasion and metastasisr-ketorolac targets gtpases and ovarian cancer cell invasion. *Molecular cancer therapeutics* **14**, 2215–2227 (2015).

[30] Cotteret, S. & Chernoff, J. The evolutionary history of effectors downstream of cdc42 and rac. *Genome biology* **3**, 1–8 (2002).

[31] Chothia, C. & Jones, E. Y. The molecular structure of cell adhesion molecules. *Annual review of biochemistry* **66**, 823–862 (1997).

[32] Joseph-Silverstein, J. & Silverstein, R. L. Cell adhesion molecules: an overview. *Cancer investigation* **16**, 176–182 (1998).

[33] Kanchanawong, P. *et al.* Nanoscale architecture of integrin-based cell adhesions. *Nature* **468**, 580–584 (2010).

[34] Lawson, C. & Schlaepfer, D. Integrin adhesions: Who's on first? what's on second? *Cell adhesion & migration* **6**, 302–306 (2012).

[35] Changede, R., Xu, X., Margadant, F. & Sheetz, M. P. Nascent integrin adhesions form on all matrix rigidities after integrin activation. *Developmental cell* **35**, 614–621 (2015).

[36] Choi, C. K. *et al.* Actin and α-actinin orchestrate the assembly and maturation of nascent adhesions in a myosin ii motor-independent manner. *Nature cell biology* **10**, 1039–1050 (2008).

[37] Thievessen, I. *et al.* Vinculin–actin interaction couples actin retrograde flow to focal adhesions, but is dispensable for focal adhesion growth. *Journal of Cell Biology* **202**, 163–177 (2013).

[38] Chastney, M. R., Conway, J. R. & Ivaska, J. Integrin adhesion complexes. *Current Biology* **31**, R536–R542 (2021).

[39] Rottner, K., Hall, A. & Small, J. Interplay between rac and rho in the control of substrate contact dynamics. *Current biology* **9**, 640–S1 (1999).

[40] Burridge, K., Molony, L. & Kelly, T. Adhesion plaques: sites of transmembrane interaction between the extracellular matrix and the actin cytoskeleton. *Journal of Cell Science* **1987**, 211–219 (1987).

[41] Nayal, A. *et al.* Paxillin phosphorylation at ser273 localizes a git1–pix–pak complex and regulates adhesion and protrusion dynamics. *The Journal of cell biology* **173**, 587–589 (2006).

[42] Deakin, N. O. & Turner, C. E. Paxillin comes of age. *Journal of cell science* **121**, 2435–2444 (2008).

[43] Burridge, K., Turner, C. E. & Romer, L. H. Tyrosine phosphorylation of paxillin and pp125fak accompanies cell adhesion to extracellular matrix: a role in cytoskeletal assembly. *The Journal of cell biology* **119**, 893–903 (1992).

[44] Rajah, A. *et al.* Paxillin s273 phosphorylation regulates adhesion dynamics and cell migration through a common protein complex with pak1 and βpix. *Scientific reports* **9**, 1–20 (2019).

[45] Ridley, A. J. & Hall, A. The small gtp-binding protein rho regulates the assembly of focal adhesions and actin stress fibers in response to growth factors. *Cell* **70**, 389–399 (1992).

[46] Danuser, G., Allard, J. & Mogilner, A. Mathematical modeling of eukaryotic cell migration: insights beyond experiments. *Annual review of cell and developmental biology* **29**, 501 (2013).

[47] Mogilner, A. & Rubinstein, B. The physics of filopodial protrusion. *Biophysical journal* **89**, 782–795 (2005).

[48] Atilgan, E., Wirtz, D. & Sun, S. X. Mechanics and dynamics of actin-driven thin membrane protrusions. *Biophysical journal* **90**, 65–76 (2006).

[49] Carlsson, A. E. Growth of branched actin networks against obstacles. *Biophysical journal* **81**, 1907–1923 (2001).

[50] DiMilla, P. A., Barbee, K. & Lauffenburger, D. A. Mathematical model for the effects of adhesion and mechanics on cell migration speed. *Biophysical journal* **60**, 15–37 (1991).

[51] Zaman, M. H., Kamm, R. D., Matsudaira, P. & Lauffenburger, D. A. Computational model for cell migration in three-dimensional matrices. *Biophysical journal* **89**, 1389–1397 (2005).

[52] Abercrombie, M. The croonian lecture, 1978-the crawling movement of metazoan cells. *Proceedings of the Royal Society of London. Series B. Biological Sciences* **207**, 129–147 (1980).

[53] Das, S. *et al.* Single-molecule tracking of small gtpase rac1 uncovers spatial regulation of membrane translocation and mechanism for polarized signaling. *Proceedings of the National Academy of Sciences* **112**, E267–E276 (2015).

[54] Digman, M. A., Brown, C. M., Horwitz, A. R., Mantulin, W. W. & Gratton, E. Paxillin dynamics measured during adhesion assembly and disassembly by correlation spectroscopy. *Biophysical journal* **94**, 2819–2831 (2008).

[55] Marée, A. F., Jilkine, A., Dawes, A., Grieneisen, V. A. & Edelstein-Keshet, L. Polarization and movement of keratocytes: a multiscale modelling approach. *Bulletin of mathematical biology* **68**, 1169–1211 (2006).

[56] Holmes, W. R., Park, J., Levchenko, A. & Edelstein-Keshet, L. A mathematical model coupling polarity signaling to cell adhesion explains diverse cell migration patterns. *PLoS computational biology* **13**, e1005524 (2017).

[57] Marée, A. F., Grieneisen, V. A. & Edelstein-Keshet, L. How cells integrate complex stimuli: the effect of feedback from phosphoinositides and cell shape on cell polarization and motility. *PLoS computational biology* **8**, e1002402 (2012).

[58] Rens, E. G. & Edelstein-Keshet, L. Cellular tango: how extracellular matrix adhesion choreographs rac-rho signaling and cell movement. *Physical biology* **18**, 066005 (2021).

[59] Byrne, K. M. *et al.* Bistability in the rac1, pak, and rhoa signaling network drives actin cytoskeleton dynamics and cell motility switches. *Cell systems* **2**, 38–48 (2016).

[60] Nguyen, L. K., Kholodenko, B. N. & Von Kriegsheim, A. Rac1 and rhoa: Networks, loops and bistability. *Small GTPases* **9**, 316–321 (2018).

[61] Mori, Y., Jilkine, A. & Edelstein-Keshet, L. Wave-pinning and cell polarity from a bistable reaction-diffusion system. *Biophysical journal* **94**, 3684–3697 (2008).

[62] Mackay, L. *Modelling the Dynamics of Cellular Motility, from Adhesion Dynamics to Cellular Migration.* Ph.D. thesis, McGill University (2020).

[63] Schreiber, C., Amiri, B., Heyn, J. C., Rädler, J. O. & Falcke, M. On the adhesion–velocity relation and length adaptation of motile cells on stepped fibronectin lanes. *Proceedings of the National Academy of Sciences* **118** (2021).

[64] Heng, Y.-W. & Koh, C.-G. Actin cytoskeleton dynamics and the cell division cycle. *The international journal of biochemistry & cell biology* **42**, 1622–1633 (2010).

[65] Rosenblatt, J., Cramer, L. P., Baum, B. & McGee, K. M. Myosin ii-dependent cortical movement is required for centrosome separation and positioning during mitotic spindle assembly. *Cell* **117**, 361–372 (2004).

[66] Kamijo, K. *et al.* Dissecting the role of rho-mediated signaling in contractile ring formation. *Molecular biology of the cell* **17**, 43–55 (2006).

[67] Zhang, W., Huang, Y. & Gunst, S. J. p21-activated kinase (pak) regulates airway smooth muscle contraction by regulating paxillin complexes that mediate actin polymerization. *The Journal of physiology* **594**, 4879–4900 (2016).

[68] Holmes, W. R., Mata, M. A. & Edelstein-Keshet, L. Local perturbation analysis: a computational tool for biophysical reaction-diffusion models. *Biophysical journal* **108**, 230–236 (2015).

Supplemental

Supplementary material of *Polarity and mixed-mode oscillations may underlie different patterns of cellular migration*

Parameter	Description	Value	Unit	References
I_R	Basal Rac activation Rate	0.0035	s^{-1}	[1]
δ_R	Rac inactivation rate	0.025	s^{-1}	[1]
L_ρ	Rho-dependent half-maximum inhibition of Rac	0.34	unitless	[1]
I_ρ	Basal Rho activation Rate	0.016	s^{-1}	[1]
δ_ρ	Rho inactivation rate	0.016	s^{-1}	[1]
L_R	Rac-dependent half-maximum inhibition of Rho	0.34	unitless	[1]
γ	Ratio of total PAK to total Rac	0.3	unitless	[1]
δ_P	Paxillin dephosphorylation rate	0.00041	s^{-1}	[1]
n	Hill coefficient	4	unitless	[1]
α_P	Linearization coefficient in paxillin activation	2.7	unitless	[1]
L_K	Active PAK-dependent half-maximum activation of paxillin	5.77	unitless	[1]
I_K	Additional Rac activation due to paxillin	0.009	s^{-1}	[1]
k_G	Association constant for GIT-PIX binding	5.71	s^{-1}	[1]
$[GIT]$	Concentration of GIT	0.11	μM	[1]
k_X	Association constant for PIX-PAK binding	41.7	s^{-1}	[1]
$[PIX]$	Concentration of PIX	0.069	μM	[1]
k_C	Association constant for Pax_p-GIT binding	5	s^{-1}	[1]
$[Pax_{tot}]$	Total concentration of paxillin	2.3	μM	[1]
α_R	Affinity constant for PAK-RacGTP binding	15	unitless	[1]
ϵ	Time constant for B	0.01	s^{-1}	Estimated
B_r	Resting state of B	10	unitless	Estimated
k_B	Recovery rate of B back to its resting state	0.04	unitless	Estimated
γ_R	Strength of R feedback onto B	8.6956	s^{-1}	Estimated
η, ϵ_B	Parameters that guarantee the positivity of B	10^4, 10^{-4}	unitless	Estimated
ϵ_L	Time constant of k_B	10^{-5}	s^{-1}	Estimated
γ_K	Source term	0.15	unitless	Estimated

Table S1: Summary of parameter values.

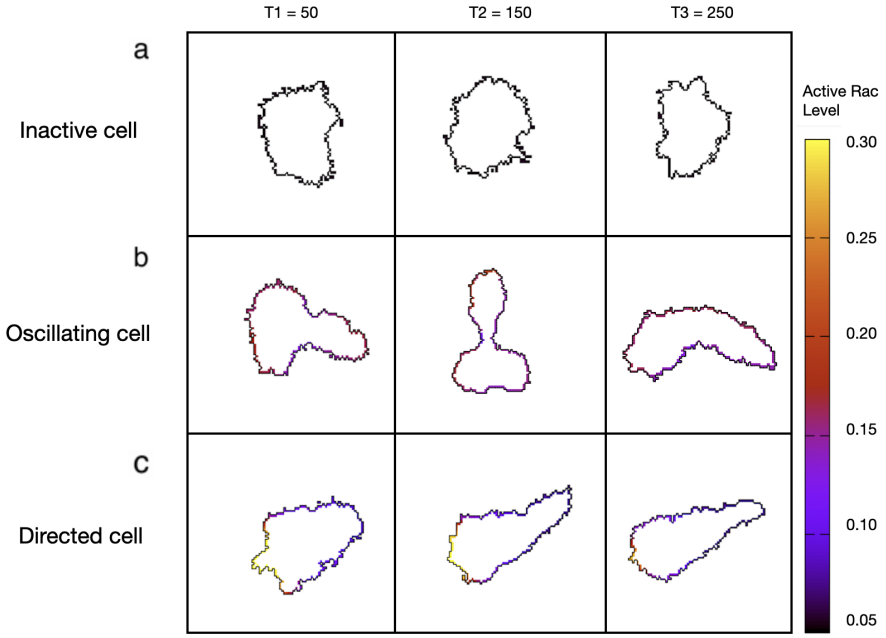

Figure S1: Membrane bound scaled active Rac concentration in simulated CPM cells defines the shapes of (a) inactive, (b) oscillating, and (c) directed cells. Simulations are shown at three different time points: $T_1 = 50$, $T_2 = 150$ and $T_3 = 250$ time-steps. Scaled active Rac concentration is colour-coded according to the colour-bar to the right.

Supplementary material of the thesis

The general framework of Local Perturbation Analysis is based on the following three assumptions

1. There are only two groups of chemical species: slow-diffusing and fast-diffusing.
2. Fast-diffusing species are homogeneously distributed.
3. Slow-diffusing species do not diffuse at all.

Diffusion coefficients are set to zero for all chemical species: to consider only one equation for the fast-diffusing species is equivalent to assume an infinitely-fast diffusion, and two equations for the slow diffusing species is equivalent to assume absence of diffusion. Working under theses hypothesis, one can approximate the system's response to a spatially local perturbation. We present here LPA applied to the 2D PDE system by studying the following system

$$\frac{\partial R^g}{\partial t} = f(R^g, R_i) \tag{S1a}$$

$$\frac{\partial R^l}{\partial t} = f(R^l, R_i) \tag{S1b}$$

$$\frac{\partial R_i}{\partial t} = -f(R^g, R_i) \tag{S1c}$$

where f is the expression derived previously to characterize the variations in Rac activation: $f(u, v) = (I_R + I_K^*)\left(\frac{L_\rho^n}{L_\rho^n + \rho^n}\right) v - \delta_R u$, R^g is active Rac global concentration, R^l is active Rac local concentration and R_i is inactive Rac concentration, which is fast-diffusing and therefore only global in the approximation. The resulting bifurcation diagram is presented in Fig S2.

In the bistable regime (defined by $0.01 \leq B \leq 11.7$), when B < 2.7 all global steady states are stable. The variable R^g undergoes a transcritical bifurcation at approximately $B \approx 2.7$, and become unstable for higher values of B, while the R^l variable becomes stable. This means that a small perturbation won't smooth out

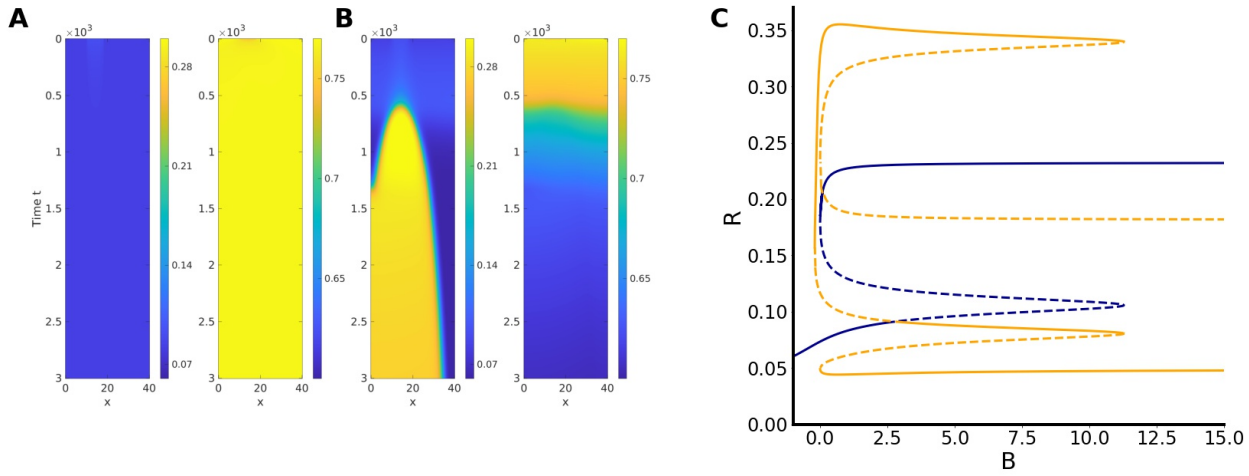

Figure S2: Local Perturbation Analysis of the 2D PDE model. Evolution of a small localized perturbation in active Rac. Global low steady state in active Rac is used as an initial condition and a small perturbation in active Rac is added, staying in the basin of attraction of the low steady state. At B=1 (A), this perturbation smooths out. At B=5 (B), the perturbation is able to gain activation, generating a region where Rac has now reached its elevated steady state. This finally results in the wave-pined profile seen in Figure 11. (C) Bifurcation diagram of the system S1 obtained on XPPAUT. Global Rac branch is in blue, local Rac branches in orange.

at B values above 2.7: the homogeneous low concentration for the global Rac variable is not a stable pattern anymore. A small amplitude perturbation starting from the basin of attraction of the global low steady state can cause gain in Rac activation to reach the upper stable branch. This is a diffusion-specific feature and can be explained by the fact that high amount of inactive Rac (caused by the global active Rac concentration being at low steady state) allows the local active Rac originating from the perturbation to strongly activate. Unstability at homogeneous low concentration was firstly observed by English mathematician Alan Turing over seventy years ago. This provides an explanation for the formation of patterns in nature, such as stripes and spots, originating from a homogeneous uniform state slightly destabilized [2]. For this reason, the region of $B \in [2.7; 11.7]$ is called the Turing instability region.

References

[1] Tang, K., Boudreau, C. G., Brown, C. M. & Khadra, A. Paxillin phosphorylation at serine 273 and its effects on rac, rho and adhesion dynamics. *PLoS computational biology* **14**, e1006303 (2018).

[2] Turing, A. M. The chemical basis of morphogenesis. *Bulletin of mathematical biology* **52**, 153–197 (1990).